DEPARTAMENTO DE ASTROFÍSICA

Universidad de La Laguna

Circumstellar effects and isotopic composition in O-rich AGB stars

Memoria que presenta
D. Víctor Pérez Mesa
para optar al grado de
Doctor por la Universidad de La Laguna.

INSTITUTO Đ ASTROFISICA Đ CANARIAS
Noviembre de 2019

Examination date: xxxx, 2020
Thesis supervisors: Dr. Domingo Aníbal García Hernández and Dr. Olga María Zamora Sánchez

ISBN: xx-xxx-xxxx-x
Depósito legal: TF-xxxx/2019

A mis hermanos,
a mis padres,
a mi abuela

Agradecimientos

Qué fácil es decir la palabra "*gracias*", cuánto bien hace y qué poco la usamos. Son muchos los "*gracias*" que se me han quedado por decir y muchas las personas a las que se los debo, así que no se me ocurre mejor momento que este para ir saldando algunas deudas. Si me olvido de alguien, espero que me perdone. Ya me conocen.

En primer lugar, tengo que darle las gracias al Instituto de Astrofísica de Canarias por darme la oportunidad de hacer esta tesis. No sé si he cambiado mucho o poco desde que entré hasta ahora, pero lo que sí sé es que los grandes responsables de todo lo que he aprendido en estos años han sido mis directores de tesis, Aníbal y Olga. Gracias por hacer que la Astrofísica me guste más hoy que el día que llegué, especialmente a Aníbal, no solo por estar ahí cuando tenía alguna duda o tener siempre comentarios que sumaban, también por ayudarme cuando no tenías que hacerlo, por sacrificar tu tiempo con tu familia trabajando y respondiéndome correos en días y horas en que no tenías que hacerlo, y sobre todo, por las conversaciones sobre la vida en general, entenderme y animarme en todo momento. Estoy orgulloso del director que he tenido. No quiero olvidarme del resto del grupo, Arturo, Thomas y Marco, gracias por el buen ambiente que siempre hemos tenido. Also thanks Maria Lugaro for inviting me to Budapest and let me see how is the research life in other research centres. Thanks Andrés, Benoit, Benjamin, Carolyn, Hannah, Jacqueline, Kundan, Borbála and Blanka for my period in Budapest.

Es imposible que en estos agradecimientos no tenga unas palabras hacia la que ha sido mi familia en el IAC, los pulpos viajeros y demás piratas de temible reputación, Ismael, Parda, Morate, Sergio, Sara, Javi, Dani, Pato, Awe, Ferra, Juanlu, Drogon y por último, Rebe. Espero que estén arrepentidos de las que han liado, porque yo lo estaría, topos. Ahora en serio, mil gracias por todos

los cafés, conversaciones, viajes, salidas, entradas, enfados y risas. He tenido mucha suerte. También me acuerdo de mucha otra gente con la que he compartido muchos momentos y me he reído a más no poder, Jesús, Daniel, Iván, Dani el basura, Jose, Nico, Alexis, Alex Ramos y demás delincuentes y malhechores de La Laguna. Gracias a todos mis compañeros del Yballa La Cuesta por hacer que me olvidara de todo durante unas horas y solo me divirtiera jugando al fútbol. Gracias a toda la gente que he conocido en Tenerife, 11 años dan para mucho.

Siempre digo que la mejor parte de mí son mi familia y mis amigos, y es que tengo los mejores amigos del mundo. Gracias Noelia por tu infinita paciencia conmigo y tirar de esta amistad cuando yo he estado desaparecido. Vales oro y los dos lo sabemos. Niko y Noé, ¿qué le digo a mi Consejo de Sabios? Lo primero que me sale decirles es que los echo mucho de menos, pero también que me alegra que estén haciendo ese viaje y que aunque no esté ahí con ustedes, cada vez que hablamos, me envían fotos y me dicen que se acuerdan de mí, siento que yo también formo parte de esa aventura. Tengan mucho cuidado y nos vemos pronto. Y después está Javi. Es curioso como tu mejor amigo llega de rebote, sin esperarlo, empieza con una conversación normal un día cualquiera y cuando te das cuenta es una de las personas más importantes de tu vida junto con tu familia. Hemos vivido momentos muy malos y muy buenos, y me alegro de que hayan sido a tu lado, porque los malos no han sido tan malos y los buenos han sido mejores. Gracias por todo.

También tengo que darle las gracias a mi familia. Me da pena no exista una palabra con la que de verdad pueda expresar todo lo que quiero decirles porque un simple "*gracias*" se queda corto. Lo que en realidad quiero decirles es que nunca podré devolverles todo el bien que me han hecho. Gracias a mi abuela por todo lo que nos ha dado durante tantos y tantos años. Ahora nos toca a nosotros cuidarte a ti para devolverte una parte y en eso mis padres, que no sé si se están dando cuenta o no (espero que sí), están siendo un ejemplo de amor, cariño y paciencia. Este amor, cariño y paciencia no son nuevos, son los mismos con los que nos han criado a mis hermanos y a mí, que no se los hemos puesto fácil, y con el que siguen manteniendo unida esta familia, aunque a veces nos rebujemos. Por último, a mis hermanos, todo lo que hago es para que algún día puedan sentirse tan orgullosos de mí como yo lo estoy de ustedes. Somos muy diferentes, pero se me cae la baba con todos. Todas las cosas buenas que pueda tener como persona son gracias a ustedes, de lo malo me he encargado yo solo, así que no sufran. Los quiero.

Bueno Víctor, al final lo conseguiste. ¿Quién lo iba a decir? No ha sido fácil, pero también lo has pasado bien. Nadie te ha exigido más de lo que tú te has exigido a ti mismo, así que quédate tranquilo porque lo has hecho lo mejor que has podido, no te has guardado nada. Estoy orgulloso de ti. Esto se termina, pero vendrán cosas nuevas, así que me parece un buen momento para escribir esa frase que tanto te repites, "Sigue, ya descansarás".

Víctor

Resumen

Esta tesis trata varios temas relacionados con el estudio de las estrellas pertenecientes a la rama asintótica de gigantes (AGB, de sus siglas en inglés asymptotic giant branch) más masivas y ricas en oxígeno en nuestra galaxia. En particular, los principales objetivos son la exploración de los efectos circunestelares en la determinación de las abundancias químicas en estrellas AGB masivas a metalicidad solar usando modelos de atmósfera pseudo-dinámicos más realistas y la obtención, por primera vez, de las abundancias elementales e isotópicas de CNO en estrellas AGB galácticas verdaderamente masivas.

En primer lugar, hemos determinado las abundancias de Rb y Zr en una muestra de estrellas AGB galácticas y masivas, previamente estudiadas con modelos hidrostáticos, usando modelos de atmósfera extensos que consideran la presencia de una envoltura circunestelar con un viento radial. Las nuevas abundancias de Rb son mucho más bajas que las obtenidas a partir de modelos hidrostáticos, mientras que las abundancias de Zr son parecidas a las hidrostáticas porque la cabeza de banda 6474 Å ZrO usada para derivar las abundancias de Zr se forma en capas más internas de la atmósfera y está menos afectada por efectos circunestelares que la línea 7800 Å Rb I. Las nuevas abundancias de [Rb/Fe] y cocientes de [Rb/Zr] se comparan mucho mejor con las predicciones teóricas, resolviendo significativamente el problema previo de la discordancia entre las observaciones y los modelos de nucleosíntesis en las estrellas AGB más masivas y confirmando que la reacción ^{22}Ne(α, n)^{25}Mg es la principal fuente de neutrones en estas estrellas.

En segundo lugar, presentamos nuevas abundancias hidrostáticas y pseudo-dinámicas de Li y Ca en una muestra de estrellas AGB masivas y ricas en oxígeno de nuestra galaxia usando los nuevos modelos de atmósfera extensos (pseudo-dinámicos). Las abundancias de Li a partir de modelos de atmósfera extensos son muy similares a las obtenidas con modelos hidrostáticos, confirmando el carácter rico en litio (incluso súper rico en litio en algunas estrellas) de

nuestra muestra de estrellas y la fuerte activación del proceso HBB (de sus siglas en inglés hot bottom burning) en estrellas AGB masivas. Esto está de acuerdo con la mayoría de modelos de nucleosíntesis de estrellas AGB. Las abundancias de Ca, las cuales han sido derivadas aquí por primera vez en estrellas AGB masivas de nuestra galaxia, son consistentes con las predicciones de modelos de nucleosíntesis de procesos 's' para estrellas AGB masivas a metalicidad solar. Una minoría de estrellas muestra una cantidad significativa de Ca depletado y damos posibles explicaciones a esta aparente e inesperada depleción de Ca.

Por último, hemos obtenido, por primera vez mediante síntesis espectral, las abundancias y cocientes isotópicos de CNO en una muestra de estrellas AGB masivas y ricas en oxígeno de nuestra galaxia al principio de la fase de pulsos térmicos (TP, de sus siglas en inglés thermally pulsing). Además, hemos encontrado que la presencia de una envoltura circunestelar y viento radial no afecta a la determinación de las abundancias elementales/isotópicas de CNO en el infrarrojo cercano. Las abundancias elementales/isotópicas de CNO derivadas están generalmente de acuerdo con las predicciones teóricas para estrellas AGB muy masivas ($\sim$7-8 $M_{\odot}$) a metalicidad solar que experimentan HBB en los primeros pulsos térmicos. En particular, las grandes sobre-abundancias de N y los bajos cocientes $^{12}C/^{13}C$ confirman la activación del HBB independientemente de las sobreabundancias de Li. Además, dos estrellas de la muestra parecen ser descendientes de estrellas progenitoras de $\sim$8 $M_{\odot}$ con HBB pero que no han experimentado ningún pulso térmico. Por lo tanto, estas estrellas son muy buenas candidatas a ser verdaderas estrellas súper-AGB. También, hemos comparado nuestros cocientes isotópicos de O con medidas hechas en granos presolares. La composición isotópica de O en dos estrellas refuerza la idea de que las estrellas AGB más masivas podrían ser el lugar de formación de los granos del Grupo II. Sin embargo, las grandes incertidumbres y nuestros límites inferiores conservativos para los cocientes de O en el resto de estrellas de la muestra, no nos permiten obtener una respuesta definitiva acerca del origen de los granos del Grupo II.

Abstract

This thesis addresses several topics in the study of the more massive and O-rich asymptotic giant branch (AGB) stars in our Galaxy. In particular, the main goals are the exploration of the circumstellar effects on the abundance determination in solar metallicity massive AGB stars by using more realistic pseudo-dynamical model atmospheres and the obtention, for the first time, of the CNO elemental abundances and isotopic ratios in truly massive Galactic AGB stars.

First, we have determined the Rb and Zr abundances in a sample of massive Galactic AGB stars, previously studied with hydrostatic models, by using extended model atmospheres that consider the presence of a circumstellar envelope with a radial wind. The new Rb abundances are much lower than those obtained from hydrostatic models, while the Zr abundances are close to the hydrostatic ones because the 6474 Å ZrO bandhead used to derive the Zr abundance is formed deeper in the atmosphere and is less affected, by the circumstellar effects, than the 7800 Å Rb I line. The new [Rb/Fe] abundances and [Rb/Zr] ratios are in much better agreement with the theoretical predictions, significantly resolving the previous mismatch between the observations and the nucleosynthesis models in the more massive AGB stars and confirming that the ^{22}Ne(α, n)^{25}Mg reaction is the main neutron source in these stars.

Second, we have reported new hydrostatic and pseudo-dynamic abundances of Li and Ca in a sample of massive Galactic O-rich AGB stars by using the new extended (pseudo-dynamical) model atmospheres. The Li abundances from extended atmosphere models are very similar to those obtained from hydrostatic models, confirming the Li-rich (and super Li-rich in some stars) character of our sample stars and the strong activation of the hot bottom burning (HBB) process in massive AGB stars. This is in good agreement with most of the AGB nucleosynthesis models. The Ca abundances, which have been derived here for the first time in massive Galactic AGB stars, are consistent with the

predictions from the *s*-process nucleosynthesis models for massive AGB stars at solar metallicity. A minority of stars show a significant Ca depletion and possible explanations are offered to explain their apparent and unexpected Ca depletion.

Finally, we have obtained, for the first time by spectral synthesis, the CNO abundances and isotopic ratios in a small sample of truly massive Galactic O-rich AGB stars at the beginning of the thermally pulsing (TP) phase. Moreover, we have found that the presence of a circumstellar envelope and radial wind is not affecting the determination of the CNO elemental/isotopic abundances in the near-infrared wavelength range. The derived CNO elemental/isotopic abundances are in general good agreement with the theoretical predictions for very massive AGB stars ($\sim$7-8 $M_{\odot}$) at solar metallicity that experience HBB in the early TPs. In particular, the large N enhancements and the low $^{12}C/^{13}C$ ratios confirm the HBB activation independently of the Li overabundances. In addition, two sample stars seem to be descendants of $\sim$8 $M_{\odot}$ HBB progenitors that have not experienced any TP and they thus represent very good candidates for truly super-AGB stars. We have also compared our O isotopic ratios with the measurements made on presolar grains. The O isotopic composition in two sample stars reinforce the idea that the more massive AGB stars could be the formation site of the Group II grains. However, the large uncertainties and our conservative lower limits for the O isotopic ratios in the rest of sample stars do not permit us to reach a definitive answer about the origin of the Group II grains.

Contents

1

Introduction

1.1 Stellar evolution of low- to intermediate-mass stars

Low- to intermediate-mass stars ($0.8 \leq M \leq 8$ $M_{\odot}$) are the great majority of stars in the Universe. These stars evolve from the main sequence (MS) to the asymptotic giant branch (AGB; see Karakas & Lattanzio 2014, for a review) phase after the exhaustion of H and He in their cores. The evolution of the low- to intermediate-mass stars from the MS to the AGB follows well defined evolutionary paths in the Hertzsprung-Russell (HR) diagram. Then, the stars pass through the Planetary Nebulae (PNe) stage before ending their lives as white dwarfs. Figure 1.1 shows the main evolutionary phases in the HR diagram.

During the MS stage, nuclear energy is provided by the different H burning mechanisms in the core of low- and intermediate-mass stars. Low-mass stars ($0.8 \leq M \leq 2.5$ $M_{\odot}$) burn H into He through proton-proton reactions (the pp chain) while in intermediate-mass stars ($2.5 \leq M \leq 8$ $M_{\odot}$) the H burning to He in the core is a combination of the pp chain and the CNO cycle. The mass limit at which the pp chain is the dominant reaction is about 2 $M_{\odot}$, while for stars with masses larger than 2 $M_{\odot}$ the CNO cycle is the preferred H burning mechanism (see Karakas & Lattanzio 2014).

After H exhaustion in the core, the stars leave the MS, but nuclear reactions still occur in external shells. In low-mass stars ($M \leq 2.5$ $M_{\odot}$), the structure consists of a degenerate gas of electrons and He core becoming hotter and denser, surrounded by a H-burning shell and a H-rich envelope. The envelope expands due to the radiation pressure by the nuclear reactions in the H-burning

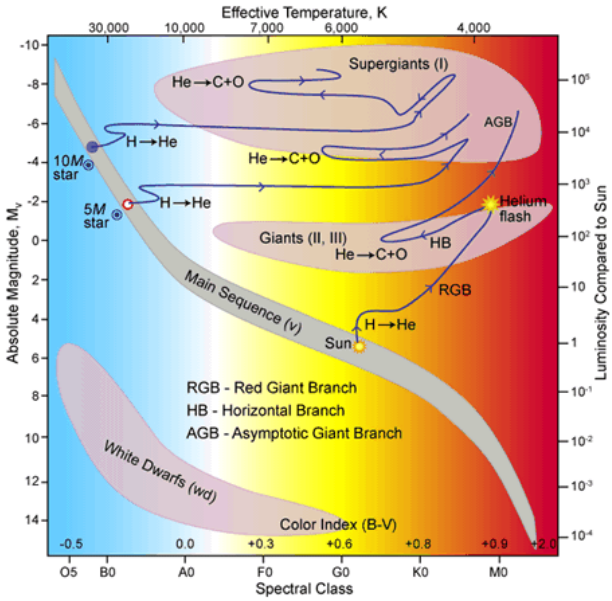

Figure 1.1: HR diagram displaying the main evolutionary phases in the life of low- to intermediate-mass stars. Illustration: Robert Hollow, Commonwealth Science and Industrial Research Organisation (CSIRO), Australia, adapted by Carin Cain.

shell and the stars ascends to the so-called Red Giant Branch (RGB) phase until a maximum luminosity of $\sim$2500 $L_\odot$ is reached, while the core is contracting. During this phase, the 1^{st} dredge-up (FDU) takes place when H and some H-burning products, such as ^{4}He, ^{14}N and ^{13}C, are brought from the top of the H-burning shell to the stellar surface (e.g. Lambert 1981). At this point, the core is hot enough to break the degenerancy of the electron gas and the He-burning is activated with a violent and explosive event, the so-called He-flash. The limit mass for the He-flash activation vary in the theoretical models depending on the implemented physics. In theoretical calculations that consider overshooting into the H-burning core during the MS, the mass limit is around 1.6 $M_\odot$ at Z = 0.02 (Bertelli et al. 1986), while when the overshooting in the core is not taken into account the predicted limit mass is about 2.1 $M_\odot$ at Z = 0.02 (Karakas & Lattanzio 2014). The He-flash marks the beginning of the Horizontal Branch (HB), another evolutionary stage. Following the core He ignition, the structure of the star consists in a central He burning, where He burns in a convective core and H in shell, which provides most of the luminosity. Due to the Coulomb repulsion[1] is larger for He than for H, more energy is needed to active the triple-alpha (3α) process and also the temperature is higher for He burning. The energy produced by the 3α process is about a factor of 10 minor than during H burning, decreasing the luminosity of the star. During the He burning the abundance of ^{12}C increases ($3\ ^4\text{He} \rightarrow\ ^{12}\text{C}$) and also the ^{16}O content from the $^{12}\text{C}(\alpha,\gamma)^{16}\text{O}$ reaction. Then, the star developes a new core composed by C and O (C-O) and an initially not degenerated gas. Finally, the density increases inside the core and the conditions for an electron gas to become degenerated are reached. Then, while the C-O core contracts and increases the luminosity ($\gtrsim 10^4$ $L_\odot$), the star ascends the so-called Asymptotic Giant Branch (AGB).

In the intermediate-mass stars ($2.5 \leq M \leq 8$ $M_\odot$) higher temperatures are reached when the stellar core contracts at the end of the MS. Therefore, the He ignition is more softly in this case because it is produced before the needed physics conditions to the electron gas turns degenerate. In addition, these stars begin the HB without experiencing the He-flash after the H is exhausted in their cores. Then, the intermediate-mass stars ascend to the AGB phase following the same path that the low-mass stars, but the so-called 2^{nd} dredge-up (SDU) takes place during the early AGB (EAGB) phase, in which nuclear reactions occur only in the surrounding He-burning shell, expanding again the stellar envelope. During the SDU, that is experienced by stars with initial masses higher than $\sim$4 $M_\odot$ at solar metallicity (this value depends on the theoretical

[1]The Coulomb repulsion is the repulsive force between two positive, or two negative charges, as described by Coulomb's law.

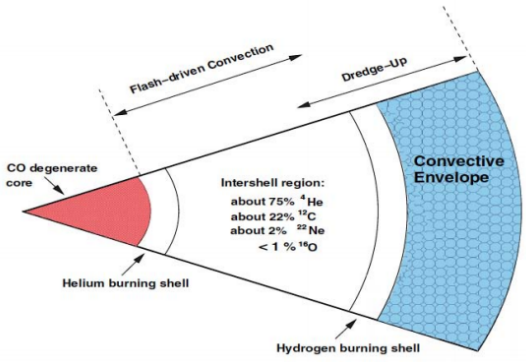

Figure 1.2: Figure taken from Karakas & Lattanzio (2014), showing the stellar structure of an AGB star. The electron-degenerate C-O core is surrounded by a He-burning shell, a intershell region, a H-burning region and the deep convective envelope. Note that the figure is not showed at scale.

model), the H shell is reached by the massive convective envelope, driving large amounts of He and isotopes, such as ^{14}N, to the stellar surface (Becker & Iben 1980). Later, while the energy from the He shell is decreasing, the star begins to contract increasing the temperature and pressure of the plasma at the bottom of the envelope and causing the ignition of the H shell (Becker & Iben 1979). When the H shell losses fuel, the EAGB phase ends and the thermal pulse (TP-AGB) phase starts.

The stellar structure in the AGB phase is shown in Figure 1.2. The star is formed by an inert core of C-O and degenerate gas of electrons surrounded by a He-burning shell and another H-burning shell. The burning shells are separated by a He-rich intershell, and in turn, surrounded by an extended convective envelope of H. Moreover, while the star is ascending the AGB a stellar wind develops in the envelope, which produces strong mass loss that can reach 10^{-4} $M_{\odot}yr^{-1}$. Due to this strong mass loss, in some cases the stars at the end of the AGB phase are highly obscured in the optical by thick dust envelopes, and those stars are only observed in the infrared (IR). The reason is that the optical light is absorved by the circumstellar dust of the envelopes and re-emitted at IR wavelenghts.

At the end of the AGB phase the stars experience also thermal pulses (TPs). The TP-AGB phase is characterised by relatively long periods of quiescent

H-burning shell, known as interpulse phase, occasionally interrupted by He ignition due to instabilities of the He-burning shell (the thermal pulse). The He-burning is ignited at the base of the He-rich intershell region (Schwarzschild & Härm 1965), which is composed of material exposed to previous He-shell flashes and the remains of H-burning shell that have been produced in the previous interpulse phase. The huge amount of energy produced by the He-flash powers a convective region from the He-burning shell to almost all the way to the H-burning shell, homogenising abundances in this region. Once convection in the intershell retreats, the energy from the He-shell flash is converted to mechanical energy and all the outer layers expand and cool down. During the expansion, the H-burning shell moves away from the core, cools down and nuclear reactions cease (decay of the pulse). In between two consecutive TPs, the processed material in the H-burning shell increases the mass of the He-rich intershell until the new He-rich material reaches the pressure and temperature needed to activate the triple-α cycle in the inner He-shell, and a new TP is produced. During the interpulse phase the convective envelope penetrates up to the limit of the H-burning shell without important changes in the luminosity; however, during the TP-phase the star experiences changes in the stellar luminosity and radius after each TP. As a consequence of the energy excess generated by the TP, it is produced convective transport of nuclear processed material from the H-burning shell to the stellar surface while the envelope expands. This process is the so-called 3^{rd} dredge-up (TDU). As a result of this penetration of the convective envelope to zones rich in nuclear processed material, the chemical composition of the stellar surface suffers important changes due to the dregde-up of C, heavy elements and *s*-process elements. Following the TDU, the star contracts, the H-burning shell is again ignited and begins a new interpulse phase. The number of TPs and TDU episodes depend on the initial mass, composition and mass-loss rate of the AGB star (see e.g. Iben & Renzini 1983; Busso et al. 1999; Mowlavi 1999, 2002; Karakas & Lattanzio 2014).

1.2 Nuleosynthesis during the AGB

At the beginning of the life of the stars, they display the original C/O ratio (C/O < 1) composition of the interstellar medium (ISM), but during the TP-AGB phase many TPs and dredge-up episodes mix ^{12}C from the He intershell into the envelope increasing the C/O ratio. For this reason, originally O-rich AGB stars can turn into C-rich AGB stars (C/O > 1) and would explain the observed spectral sequence from M- to C-type stars:

$$M \longrightarrow MS \longrightarrow S \longrightarrow SC \longrightarrow C, \tag{1.1}$$

where M-type stars have C/O $\sim$ 0.5, similar to the Sun, the MS-stars have M-type C/O ratio and small *s*-elements overabundances ([s/Fe] $\sim$ 0.3) in the stellar surface, S-stars display C/O $\sim$ 1 and strong overabundances of *s*-elements ([s/Fe] $\sim$ 0.5), the SC-stars are C-rich stars, but their C/O ratio is still $\sim$ 1, with strong overabundances of *s*-elements ([s/Fe] $\sim$ 0.5), and finally, the C-type stars have C/O $>$ 1 by definition (Wallerstein & Knapp 1998; Mowlavi 1999).

In addition, the AGB stars display slow-neutron elements (*s*-elements) in their surface from the intershell region, which is composed of the material processed in the H-burning shell ($\approx$98% ^{4}He and 2% ^{14}N Karakas & Lattanzio 2014). These neutron-rich species (e.g. Zr, Y, Sr, Ba, Tc), heavier than Fe, are formed by slow-neutron captures (compared with the β-decay) in the interpulse phase. During the TPs, some ^{4}He in the shell is converted into ^{12}C throught the triple-α process: 3^{4}He $\longrightarrow$ ^{12}C, which is the main source of energy during TPs, while the ^{12}C(α, γ)^{16}O reaction needs a reservoir of ^{12}C for efficient activation and is not important during the TPs. This process changes the chemical composition of the intershell region, resulting in ^{4}He- and ^{12}C-rich, and a few percent of ^{16}O (Karakas & Lattanzio 2014). Then, the inclusion of overshooting into the C-O core enriches the ^{12}C and ^{16}O abundances in the intershell (Herwig 2000), and the ^{12}C can react with H to form ^{13}C in the interpulse phase. The ^{13}C(α,n)^{16}O reaction is an important neutron source, and those neutrons can be captured by Fe nuclei and other heavy elements to form *s*-elements that later are dregde-up to the stellar surface in the next TP (Lambert et al. 1995; Abia et al. 2001; Busso et al. 2001; Karakas & Lattanzio 2014). Another neutron source is the ^{22}Ne, which can be formed from ^{14}N throught the CNO cycle in the H-burning shell. The ^{22}Ne(α, n)^{25}Mg reaction requires higher temperatures and produces higher neutron densities than the ^{13}C(α,n)^{16}O reaction, forming also very different isotopes (van Raai et al. 2012; Fishlock et al. 2014).

1.2.1 Nucleosynthesis from hot bottom burning

The low-mass AGB stars in the range 1.5 $\lesssim$ M $\lesssim$ 4 M$_{\odot}$ are C-rich stars[2] (C/O $>$ 1) because ^{12}C is produced during the TP-AGB phase and carried to the stellar surface via the TDU, turning O-rich stars into C-rich ones (Herwig 2005; Karakas & Lattanzio 2007; Lugaro & Chieffi 2011). On the other hand, the more massive AGB stars (M $\gtrsim$ 4-5 M$_{\odot}$) are O-rich (C/O $<$ 1) due to the activation of the so-called hot bottom burning (HBB) process (e.g. Sackmann & Boothroyd 1992; Mazzitelli et al. 1999). The mass limit to activate the HBB is

[2] In stars with M $\lesssim$ 1.5 M$_{\odot}$ the TDU is not activated and the stars remain O-rich. Note that the range of masses is strongly dependent on the metallicity and theoretical model.

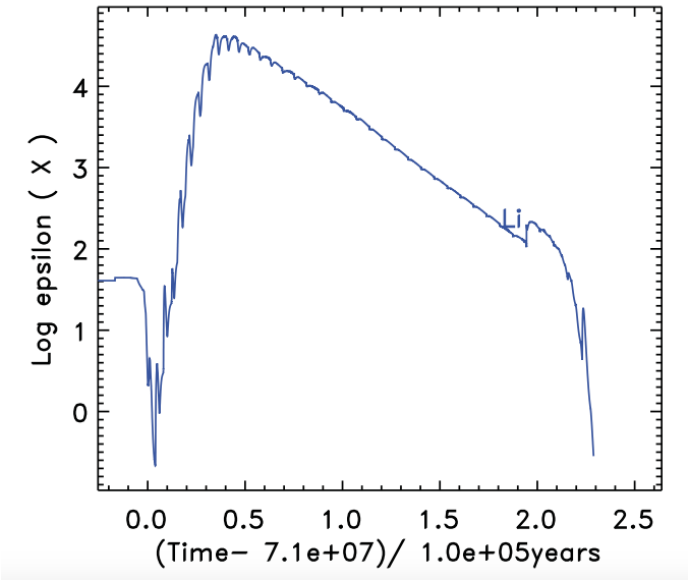

Figure 1.3: Figure taken from Karakas & Lattanzio (2014), showing the ^{7}Li surface enhancement during the TP-AGB phase for a M = 6 $M_{\odot}$ at Z = 0.02 Monash model.

strongly model dependent. In the ATON models (Di Criscienzo et al. 2016) the stellar mass needed to the HBB activation is M > 3-4 $M_{\odot}$ at Z = 0.014, while the Monash models (Karakas & Lugaro 2016), which use the mixing lenght theory of convection (MLT; Böhm-Vitense 1958), predict a limit mass of M > 4-5 $M_{\odot}$ at Z = 0.014. On the other hand, the FRUITY[3] models (Cristallo et al. 2015), that also use the MLT of convection but under the formulae from Straniero et al. (2006), do not obtain the HBB activation at solar metallicity.

The characteristic temperature to activate the HBB at the base of the convective envelope is extremely high, reaching values of the order or even higher than 100 MK in massive AGB stars at subsolar metallicity (Karakas

[3]FUll-Network Repository of Updated Isotopic Tables and Yields: http://fruity.oa-abruzzo.inaf.it/.

& Lattanzio 2014). Once the temperature is high enough, the CN cycle is activated and ^{12}C is converted into ^{13}C and ^{14}N via proton captures at the base of the convective envelope, preventing the formation of a C-rich star (Sackmann & Boothroyd 1992; Mazzitelli et al. 1999). First, ^{12}C and ^{15}N are destroyed by the CN cycle, and later, the isotopes ^{16}O and ^{18}O are also destroyed to form ^{14}N (Karakas & Lattanzio 2014). The HBB models also predict the production of ^{7}Li via the ^{7}Be transport mechanism (Cameron & Fowler 1971). One of the chains in the Cameron-Fowler ^{7}Be transport mechanism, ^{3}He(α,γ)^{7}Be(e^{-},v)^{7}Li, predicts that Li should be detectable at the stellar surface regions, at least for a short period of time, together with *s*-elements (e.g. Rb, Zr, Ba, Tc, Nd, etc.) produced during the TP phase. Once the ^{3}He is depleted in the envelope, the ^{7}Li production stops. In Figure 1.3 the ^{7}Li evolution at the stellar surface for a M = 6 M$_{\odot}$ Monash model at Z = 0.02 during the TP-AGB phase is shown. The effect of the HBB activation is that C/O < 1 during the TP-AGB phase and only increases when the HBB is shutting down during the last TPs. The evolution of the ^{12}C/^{13}C ratio and N abundance are clear signatures of the HBB. While the ^{12}C/^{13}C ratio decreases at the beginning of the TP-AGB phase and shows low values (^{12}C/^{13}C $\approx$ 3 for the M = 6 M$_{\odot}$ Monash model, at Z = 0.02) for most of the TPs, the N enhancement strongly increases because primary ^{12}C is mixed from the intershell by the TDU into the envelope, producing N. The ^{14}N/^{15}N ratio during the evolution reaches high values (^{14}N/^{15}N $>$ 10,000), near to the CN cycle equilibrium value. Finally, the ^{16}O/^{17}O ratio increases during the TP-phase, and also the ^{16}O/^{18}O, due to the fact that almost all ^{18}O is destroyed. However, the total O elemental abundance does not experience a strong decay (Karakas & Lattanzio 2014).

The activation of the HBB is supported by spectroscopic observations of massive O-rich AGB stars. First, the high Li enhancements observed in massive AGB stars at different metallicities demonstate the HBB activation in the Galaxy (Fe/H = 0.0; e.g. García-Hernández et al. 2007a, 2013; Pérez-Mesa et al. 2019), the Magellanic Clouds (Fe/H = -0.7--0.3; e.g. Plez et al. 1993; Smith et al. 1995; García-Hernández et al. 2009a) and the dwarf galaxy IC 1613 (Fe/H = -1.6; e.g. Menzies et al. 2015). Secondly, the high N abundances and low ^{12}C/^{13}C ratios in massive Li-rich AGB stars in the Magellanic Clouds are clear signatures of the HBB (e.g. Plez et al. 1993; McSaveney et al. 2007). In addition, observations of type-I planetary nebulae, at different metallicities in different galaxies, which are expected to be the descendants of the HBB massive AGB stars based on their strong N and He overabundances, support the HBB activation in massive AGB stars (see e.g. Leisy & Dennefeld 1996; Stanghellini et al. 2006; Karakas et al. 2009; García-Rojas et al. 2016).

1.3 The slow neutron-capture process

Most of the heavy nuclei with atomic masses larger than A > 56 in the universe are formed by neutron capture onto abundant Fe-peak elements. There are two main neutron capture processes: the slow neutron capture process (s-process) and the rapid neutron capture process (r-process). The r-process occurs under conditions of very high neutron densities ($N_n \gtrsim 10^{20}$ n cm^{-3}); so the timescales for neutron captures are much faster than the β-decay rate of unstable isotopes (Karakas & Lattanzio 2014). The extreme conditions for r-process can only occur during supernovae explosions (e.g. Winteler et al. 2012), colliding neutron stars (e.g. Korobkin et al. 2012) and black hole/neutron star mergers (Surman et al. 2008). In contrast, the s-procees, which is responsable of the formation of about half of elements heavier than Fe, occurs under relatively low neutron densities ($N_n \lesssim 10^{18}$ n cm^{-3}) and the timescale for neutron captures is generally slower than the β-decay rates (Karakas & Lattanzio 2014). The AGB stars are one of the sites of the s-process, so the rest of this section will be focused in the s-process.

There are two neutron sources during the TP-AGB phase that produce the free neutrons to form the s-elements:

$$^{14}\mathrm{N}(\alpha,\gamma)^{18}\mathrm{F}(\beta^{+}v)^{18}\mathrm{O}(\alpha,\gamma)^{22}\mathrm{Ne}(\alpha,n)^{25}\mathrm{Mg} \tag{1.2}$$

$$^{12}\mathrm{C}(p,\gamma)^{13}\mathrm{N}(\beta^{+}v)^{13}\mathrm{C}(\alpha,n)^{16}\mathrm{O} \tag{1.3}$$

Historically, the ^{22}Ne(α,n)^{25}Mg reaction was identified as a source of neutrons for AGB stars by Cameron (1960). From the CNO cycling, the intershell region is rich in ^{14}N, which can experience α captures and forms ^{22}Ne during a TP. Then, if the temperature reachs 3×10^{8} K, the ^{22}Ne suffers α captures to produce ^{25}Mg and ^{26}Mg. During a convective TP, the ^{22}Ne(α,n)^{25}Mg reaction releases free neutrons. This reaction operates more efficiently in massive (M $\gtrsim$ 4 M$_{\odot}$) AGB stars.

However, all the observations were historically compatible with low-mass (M $\lesssim$ 4 M$_{\odot}$) AGB stars, where the ^{13}C(α,n)^{16}O reaction should be the dominant neutron source. For the efficient activation of the ^{13}C(α,n)^{16}O reaction, some ^{13}C is needed in the intershell. Although some ^{13}C is provided by the CNO cycling during the previous interpulse phase, the amount of ^{13}C is small to account for the s-process enhancements observed in AGB stars (Gallino et al. 1998; Karakas et al. 2007). The extra ^{13}C comes from the so-called ^{13}C pocket (Iben & Renzini 1982a), which is a thin layer rich in ^{13}C and ^{14}N. In order

to reach the necessary amount of ^{13}C to explain the *s*-element AGB abundances, proton and α capture reactions are required in the He intershell, which is blank of protons, so some protons are mixed from the convective envelope into the top layers of the He intershell. Then, these protons react with ^{12}C that is abundant in the He intershell, to form ^{13}C via the CN cycle reactions: $^{12}C(p,\gamma)^{13}N(\beta^{+}v)^{13}C$ (Iben & Renzini 1982b). Finally, the $^{13}C(\alpha,n)^{16}O$ reaction is produced in radiative conditions before the beginning of the next TP (Straniero et al. 1995). Therefore, the *s*-process ocurrs in the same layer than the ^{13}C pocket during the interpulse phase, turning this layer into *s*-element rich and in the next convective TP the material will be mixed in the intershell.

In short, the $^{22}Ne(\alpha,n)^{25}Mg$ reaction is the dominant neutron source in massive AGB stars and operates during the convective TPs, while in the low-mass AGB stars the temperature is not high enough to active the $^{22}Ne(\alpha,n)^{25}Mg$ reaction and, as a consequence, the $^{13}C(\alpha,n)^{16}O$ reaction is the main source of free neutrons in those stars, operating during the interpulse phase. The mass limit for which the neutron source swicthes is ~ 4 M$_{\odot}$ at Z = 0.02 (Goriely & Siess 2004).

A different *s*-element pattern is expected depending on the dominant neutron source. The ^{13}C source, which operates on long timescales ($\approx 10^3$ years) and lower neutron densities ($\lesssim 10^7$ n/cm^3), is responsible of the *s*-process reaching isotopes (like Ba and Pb) beyond the first *s*-peak at Sr-Y-Zr. In contrast, the ^{22}Ne reaction, which operates on short timescales ($\approx$10 years) and higher neutron densities (up to 10^{13} n/cm^3), does not produce isotopes beyond the first *s*-process peak (Gallino et al. 1998). In addition, the ^{22}Ne neutron source activates some key branching points that are not efficiently activated during the operation of the ^{13}C source. In particular, the produced Rb depends on the probability of ^{85}Kr and ^{86}Rb capturing a neutron before decaying and acting as branching points (see van Raai et al. 2012, for more details). The probability of this to happen depends on the local neutron density (Beer & Macklin 1989). Once the ^{85}Kr and ^{86}Rb branching points are open, the isotope ^{87}Rb is strongly produced and the ^{87}Rb/^{85}Rb ratio is a direct indicator of the neutron density at the production site. However, it is not possible to distinguish individual ^{87}Rb and ^{85}Rb atomic lines from stellar spectra (García-Hernández et al. 2006). In contrast, the relative abundance of Rb to other nearby *s*-element, such as Zr (or Sr or Y) is very sensitive to the neutron density, and so a good discriminant of the stellar mass and the neutron source at the *s*-process site in AGB stars (Lambert et al. 1995; Abia et al. 2001; García-Hernández et al. 2006; van Raai et al. 2012). For example, in low-mass AGB stars, where the $^{13}C(\alpha,n)^{16}O$ reaction is the dominant neutron source, [Rb/Zr] < 1 (Plez et al. 1993; Lambert et al. 1995; Abia et al. 2001), while in more massive AGB

stars, where the ^{22}Ne(α,n)^{25}Mg reaction releases the free neutrons, [Rb/Zr] > 1 (García-Hernández et al. 2006, 2007a, 2009a).

Moreover, the free neutrons from the ^{22}Ne reaction can also drive neutron captures on the light elements, including the Ca isotopes. The total abundance of Ca is predicted not to vary so much in AGB stars, roughly 10% (e.g. Karakas & Lugaro 2016), but the isotopic composition of Ca can be affected, mostly resulting in an overproduction of ^{46}Ca relatively to the other Ca isotopes (see also Wasserburg et al. 2015). In addition, the radionuclide ^{41}Ca (half-life of 0.1 Myr) can be produced and also carried up to the stellar surface from the intershell region via the TDU, with maximum ^{41}Ca/^{40}Ca ratios at the stellar surface of the order of 10^{-4} (see e.g. Trigo-Rodríguez et al. 2009; Lugaro et al. 2012, 2014). The ^{41}Ca isotope is destroyed by neutron captures via ^{41}Ca(n,α)^{38}Ar and ^{41}Ca(n,p)^{41}K, but all of these interaction channels are uncertain (see Lugaro et al. 2018, for a discussion), so the production of ^{41}Ca could in principle lead to a decrease in the total Ca abundance. In any case, the cross section of the main production channel of ^{41}Ca, the ^{40}Ca(n,γ)^{41}Ca reaction is well determined (Dillmann et al. 2009), so we do not expect major changes in the predictions from the models if any of the input physics related to ^{41}Ca is modified.

1.4 The Rb problem in massive AGB stars

As we mentioned above, the ^{22}Ne(α,n)^{25}Mg reaction favors the production of ^{87}Rb because of the operation of branching points at ^{85}Kr and ^{86}Rb. At high neutron density, other radioisotopes such as ^{60}Fe and ^{41}Ca are also efficiently overproduced as well as other isotopes like ^{96}Zr. The [Rb/Zr] ratio is a powerful indicator of the neutron density and, as such, is a good indicator of the stellar mass in AGB stars. Observationally, [Rb/Zr] < 0 is found in low-mass AGB stars (Plez et al. 1993; Lambert et al. 1995; Abia et al. 2001), while more massive AGB stars display [Rb/Zr] > 0 (García-Hernández et al. 2006, 2007a, 2009a).

García-Hernández et al. (2006) studied for the first time a sample of the more massive and O-rich AGB stars of our Galaxy. These stars displayed strong Rb overabundances and confirmed the activation of the ^{22}Ne neutron source in massive AGB stars. The AGB nucleosynthesis models (e.g. van Raai et al. 2012) can reproduce the observed correlation between the Rb abundances and the stellar mass showed in García-Hernández et al. (2006) but they cannot explain the extremely high Rb abundances seen in the more extreme stars. In addition, Rb-rich AGB stars were also found in other Galaxies such as the MCs and those stars displayed extremely high Rb abundances and low Zr abundances, so

extraordinary high [Rb/Zr] > 3-4 dex ratios were derived (García-Hernández et al. 2009a). Thus, the Rb problem had two parts: the extremely high Rb overabundances and the large [Rb/Zr] ratios. The standard theoretical models qualitatively described the observations of Rb-rich AGB stars in both the MCs and our Galaxy, in the sense that increasing Rb abundances with increasing stellar mass and decreasing metallicity were theoretically predicted (van Raai et al. 2012). However, the standard theoretical models were far from matching the observational results and, in the framework of the *s*-process, it was not possible to overproduce Rb without co-producing Zr at similar levels. A way to produce more Rb was the delay of the superwind phase in the more massive AGB stars (Karakas et al. 2012). Indeed, massive AGB stars with delayed superwinds can produce more Rb than the standard models; however, the delayed superwinds co-produced more Zr. There were two possible explanations for the Rb problem: (i) the high Rb and [Rb/Zr] ratios are real, then an unknown nucleosynthesis process is at work in the more luminous and extreme AGB stars; (ii) the extremely high Rb enhancements and [Rb/Zr] ratios are artifacts of the abundance analysis; i.e. the adopted model atmospheres (with hydrostatic equilibrium and LTE) likely fail to represent the real stars. More realistic model atmospheres (e.g. models including a circumstellar envelope) are needed to address the discrepancy observed.

1.4.1 New pseudo-dynamic models

Zamora et al. (2014) developed more realistic model atmospheres for extreme AGB stars. For this, Zamora et al. (2014) considered the presence of a gaseous circumstellar envelope with a radial wind. A modified version of the spectral synthesis code Turbospectrum (Alvarez & Plez 1998; Plez 2012) was used to deal with extended atmosphere models and velocity fields. In these models, scattering is only included for the continuum, an approximation that is consistent with complementary Monte Carlo simulations. In addition, the new pseudo-dynamic models are constructed from the original MARCS hydrostatic model, expanding the atmospheric radius by the inclusion of a wind out to about 5 stellar radii, with a radial velocity field in spherical symmetry. Moreover, the stellar wind is computed under the assumptions of mass conservation (Eq. 1.4) and radiative thermal equilibrium (Eq. 1.5), following a classical β-velocity law (Eq. 1.6),

$$\rho(r) = \frac{\dot{M}}{4\pi r^2 v(r)}, \tag{1.4}$$

$$rT^2 = constant = r_{out}T_{out}^2, \tag{1.5}$$

$$v(r) = v_0 + (v_\infty - v_0)\left(1 - \frac{R_*}{r}\right)^\beta \tag{1.6}$$

where R_* is the radius corresponding to $r(\tau_{Ross} = 1)$, r is the distance from the centre of the star and τ_{Ross} is the Rosseland optical depth[4]. In Eq. 1.4, $\rho(r)$ is the density at the envelope radius r, $\dot{M}$ is the mass-loss rate and $v(r)$ is the velocity of the envelope, which is calculated by means of Eq. 1.6. In Eq. 1.6, v_0 is a reference velocity for the beginning of the wind and β is an arbitrary free parameter. Zamora et al. (2014) takes $v_0 = v(R_*)$ for the onset of the wind and the extension of the envelope begins from the outer radius of the hydrostatic model. Using Eq. 1.5 the envelope is extended, layer by layer, out to the distance r_{max}, which corresponds to the maximum radius in our calculations, with $T_{min} = 1000$ K. Turbospectrum cannot compute lower temperatures due to numerical reasons (see Zamora et al. 2014, for more details).

By using the new extended atmosphere models, Zamora et al. (2014) preliminarly determined the Rb and Zr abundances in five representative O-rich AGB stars with different expansion velocities and metallicities. The new pseudo-dynamical models reproduced the profiles (photospheric and circumstellar components) of the observed resonant 7800 Å Rb I line much better than the classical hydrostatic models. In addition, the main result of that work is that the effect of the circumstellar envelope is dramatic and the derived Rb abundances are much lower (by 1-2 dex) in those O-rich AGB stars showing the higher circumstellar expansion velocities. However, the Zr abundances remain close to the hydrostatic values because the 6474 Å ZrO bandhead is formed deeper in the atmosphere and is less affected than the Rb I line. In summary, the preliminary Rb abundances and [Rb/Zr] ratios derived in Zamora et al. (2014) are in good agreement with the massive AGB nucleosynthesis models and would resolve the problem of the mismatch between the observations of massive Rb-rich AGB stars and the theoretical predictions (see Zamora et al. 2014, for more details). One of the goals of this thesis is to study the effect of the circumstellar envelope on the Rb and Zr abundances in a larger sample of massive Galactic AGB stars, to explore possible circumstellar effects in the abundance determination of other elements (e.g. Li and Ca) and also the extension to molecular and atomic lines (CN, CO, OH) on the near-IR.

[4]The particularity of this optical depth is that uses a temperature derivatives of the Plack distribution as the weighting function.

1.5 CNO isotopic ratios and presolar grains

The CNO isotopic ratios, which are indicators of the nucleosynthesis processes experienced by the stars during their evolution, are a complementary way to prove the HBB effects in massive AGB stars. Moreover, the advantage of the isotopic ratios over the elemental abundances is that they are less dependent on variations of the stellar parameters and their determination is more robust. In addition, the AGB stellar wind of low- and intermediate-mass stars, together with the supernovae explosions of massive stars, are the main sources of enrichment of the ISM and also the origin of the vast majority of meteoritic stardust grains (Hoppe & Ott 1997; Nittler et al. 1997; Lugaro et al. 2017). The composition of the material ejected by the AGB star depends on the initial stellar composition, nuclear processing and mixing of the stellar material over the lifetime of the star (Hinkle et al. 2016). The abundances produced in the AGB phase are very important in the condensation of circumstellar dust around these stars, and that dust is the origin of the majority of interstellar grain nuclei (Gehrz 1998). The interstellar grains from the AGB stellar wind have been conserved in meteorites, which can be analyzed at the laboratory in order to measure the isotopic ratios of C and O in the presolar grains. This allows a direct comparison between the isotopic ratios from the interstellar dust and AGB stars.

The isotopic ratios measured in the atmospheres of AGB stars are modified by the CNO cycle, He-burning and mixing processes that occur in the stellar interior over the lifetime of the star (e.g. Dearborn 1992). The material produced by the nucleosynthesis processes can be dredged-up at the surface due to deep mixing, resulting in important modifications of the surface isotopic abundances of C and O. For example, in the FDU (when the stars leave the MS and approches the RGB) and SDU (during the early-AGB phase for M > 4 $M_{\odot}$) the material previously exposed to the CNO cycle is mixed and brought to the stellar surface (Hinkle et al. 2016). Moreover, the TPs during the TP-AGB phase and the TDU during the late AGB phase bring fresh material to the surface. In addition, in the more massive AGB stars (M > 4-5 $M_{\odot}$) the HBB process is activated when the temperature at the base of the convective envelope is high enough to activate the CNO cycle and the combination of this nuclear burning and convective mixing cause important changes in the isotopic ratios at the stellar surface.

Presolar grains show clear signatures of the nucleosynthesis and mixing process ocurred in the parent stars (Zinner 1998). Figure 1.4 shows the O isotopic ratios for presolar oxide and silicate grains, separated into Groups following the Nittler et al. (1997) definitions. Among them, the majority show

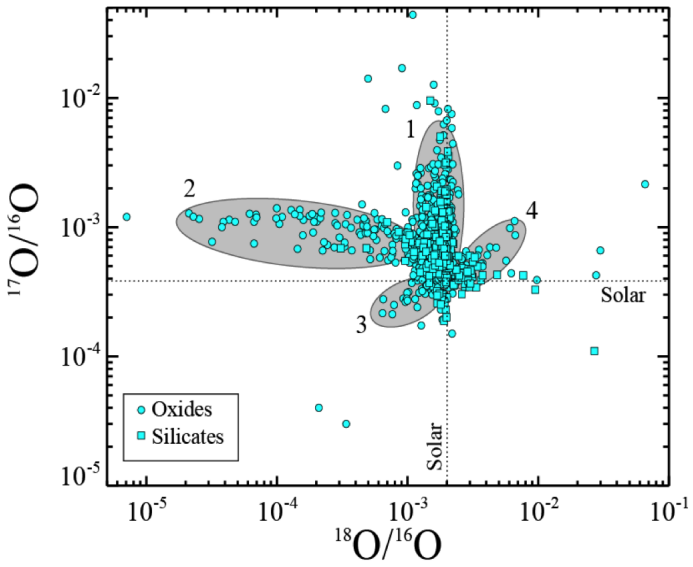

Figure 1.4: O isotopic ratios in presolar oxide (circles) and silicate (squares) grains (see Nittler et al. 2008, for data source). The dashed lines show the solar values for the $^{17}O/^{16}O$ and $^{18}O/^{16}O$ isotopic ratios and the ellipses indicate the different grain Groups defined by Nittler et al. (1997).

^{17}O excesses and slight to strong ^{18}O depletions, characteristic of H-burning by the CNO cycles, and are believed to originate in the wind of AGB stars (Nittler 2009). The ^{17}O excesses in Group I population is characteristic of the FDU in red giant stars of M $\sim$ 1-3 M$_{\odot}$ and their origin is attributed to the O-rich phases of the AGB (Lugaro et al. 2017). The relatively small ^{17}O excesses displayed by Group III grains can also be explained by AGB stars of low mass (M $<$ 1.2 M$_{\odot}$) and metallicity, because lower-metallicity stars are expected to have formed with lower abundances of the ^{17}O and ^{18}O isotopes and the FDU only has a minor impact on the surface O isotopic composition in such low-mass stars (Nittler et al. 1997; Nittler & Cowsik 1997). The difference between the O isotopic distribution of the Groups I and III is easily explained by a combination of Galactic chemical evolution (GCE) and dredge-up models (see Nittler 2009, for more details). In contrast, the ^{18}O enrichment displayed by Group IV grains is strongly supportive of a supernova origin for the majority of these grains, which is also the most likely origin for the grains of the Group III with strong ^{17}O depletion (see e.g. Messenger et al. 2005; Nittler et al. 2008; Vollmer et al. 2008).

The Group II grains, like the Group I ones, display excesses in ^{17}O but also a high depletion of ^{18}O, resulting in ^{18}O/^{16}O ratios that are up to two orders of magnitude lower than the solar value (Lugaro et al. 2017). The ^{17}O/^{16}O ratios are mainly set by the FDU and depend strongly on the stellar mass with only a mild dependence on the initial composition. However, the ^{18}O/^{16}O ratios are only affected about $\sim$ 20% by the FDU, so that the larger variations found in the ^{18}O/^{16}O ratios must reflect variations in the initial composition and/or additional processing through cool bottom processing (CBP; Nollett et al. 2003; Palmerini et al. 2011). The CBP is a process in which extra mixing is experienced below the bottom of the convective envelope in low-mass AGB stars. In this scenario, material from the bottom of the convective envelope penetrates into the thin radiative region between the base of the convective envelope and the top of the H-burning shell, where the temperature and density increase steeply with mass depth and proton captures can ocurrs (Lugaro et al. 2017). The main differences between the HBB and the CBP are: (i) the HBB takes place in massive AGB stars and the CBP in low-mass AGB stars; (ii) the material is processed at higher temperatures in the HBB (60-80 MK) than in the CBP (40-55 MK); (iii) mixing occurs via convection in the case of HBB, while non-convective extra mixing is needed in the CBP case (Lugaro et al. 2017).

While the origin of the Group I grains is well understood and attributed to low-mass AGB stars, the hypothesis on the site of formation for Group II grains are still tentative. One possible candidate could be the massive AGB

stars, which generate large amounts of dust and are expected to have contributed around half of the O-rich dust of AGB origin in the Solar System as based on current models of Galactic dust evolution (Gail et al. 2009; Zhukovska et al. 2015). However, although the Group II grains show the highly depleted $^{18}O/^{16}O$ ratios, qualitatively expected from HBB, no stardust grains have been found to show the $^{17}O/^{16}O$ ratios predicted by the HBB using the available reaction rates (Iliadis et al. 2010). Thus, it is suggested that the origin of Group II grains are AGB stars of low mass ($M < 1.5\ M_{\odot}$), which did not dredge-up enough amounts of C to become C-rich but the star experienced CBP. However, at the temperatures typical of CBP (40-55 MK), only the higher $^{17}O/^{16}O$ ratios observed in Group II grains are usually reproduced (Lugaro et al. 2017).

Recently, Lugaro et al. (2017) showed that the increased proton-capture rate of ^{17}O (as reported by the Laboratory for Underground Nuclear Astrophysics, LUNA), at typical temperatures of CBP (40-55 MK), the new rate only reproduces the lowest $^{17}O/^{16}O$ ratios observed in Group II grains, but at the higher typical temperatures of HBB (60-80 MK), the new rate can reproduce most of the observed range of $^{17}O/^{16}O$ ratios, in well agreement with the expected signature of HBB in stardust grains. The Lugaro et al. (2017) result is robust because any AGB model experiencing HBB, and with temperatures in the range 60-80 MK, produces $^{17}O/^{16}O$ ratios in good agreement with the values observed in most Group II grains. However, these theoretical results have not been confronted with observations of truly massive AGB stars in our Galaxy because the few previous works about the CNO isotopic ratios in evolved massive AGB stars had problems modelling the spectra of such extreme and dusty stars or the studied giant stars did not show evidences for HBB. This is thus other of the ain objectives of this thesis: to derive for the first time, by spectral synthesis, the CNO isotopic ratios in truly massive AGB stars at the beginning of the TP phase and compare those CNO abundances with theoretical models and the presolar grains database. This is because such stars may display simpler spectra (less affected by circumstellar dust and should be more easy to model) and already show the strong effects of the HBB (García-Hernández et al. 2013).

1.6 Outline of this thesis

This thesis is mainly based on three articles, two of them already published and the third one will be submitted soon for publication. The manuscript is organized as follows:

- In Chapter 2, we report new Rb and Zr abundances in a sample (21) of

massive Galactic AGB stars, previously studied with hydrostatic models, by using more realistic extended model atmospheres in order to confirm the ^{22}Ne neutron source and try to resolve the Rb problem in massive AGB stars.

- In Chapter 3, we extend the study of the circumstellar effects to the Li and Ca abundances in a larger sample (30) of massive Galactic O-rich AGB stars. The Li abundances had previously been determined with hydrostatic models, while the Ca abundances are obtained here for the first time. The objective is to confirm/discard if the Li-rich (and super Li-rich, in some cases) character of the sample stars supports the activation of the HBB process in massive Galactic AGB stars.

- In chapter 4, we obtain for the first time, by spectral synthesis, the CNO elemental and isotopic ratios (e.g. ^{12}C/^{13}C, ^{14}N/^{15}N, ^{16}O/^{17}O and ^{16}O/^{18}O) in a small sample (5) of truly massive Galactic AGB stars at the beginning of the TP phase. In addition, we study in the near-IR how the CNO elemental/isotopic abundances are affected by the presence of a circumstellar envelope with a radial wind. Moreover, we compare the derived CNO elemental abundances and isotopic ratios with AGB nucleosynthesis predictions and presolar grains data in order to try to find the site of the origin of the Group II grains.

- Finally, we give a summary of the conclusions reached in this thesis in Chapter 5 and list directions for future work in Chapter 6.

2

Rb and Zr circumstellar abundances in massive Galactic AGB stars

Based on
V. Pérez-Mesa et al. 2017, A&A, 606, A20

ABSTRACT - Luminous Galactic OH/IR stars have been identified as massive (M > 4-5 $M_{\odot}$) AGB stars experiencing hot bottom burning (HBB) and Li production. Their Rb abundances and [Rb/Zr] ratios, as derived from classical hydrostatic model atmospheres, are significantly higher than predictions from AGB nucleosynthesis models, posing a problem for our understanding of AGB evolution and nucleosynthesis. We report new Rb and Zr abundances in a sample of massive Galactic AGB stars, previously studied with hydrostatic models, by using more realistic extended model atmospheres. We confirm that the use of extended atmosphere models can solve the discrepancy between the AGB nucleosynthesis theoretical models and the observations of Galactic massive AGB stars.

2.1 Introduction

The more massive AGB stars(Herwig 2005; Karakas & Lattanzio 2014) are intermediate-mass ($4 \leq M \leq 8$ $M_{\odot}$) stars, and are O-rich (C/O < 1) because the HBB process is activated. Through the CN cycle via proton captures at the base of the convective envelope, HBB converts ^{12}C into ^{13}C and ^{14}N,

preventing the formation of a C-rich star (C/O > 1) (Sackmann & Boothroyd 1992; Mazzitelli et al. 1999).

The *s*-process allows the production of neutron-rich elements heavier than iron (*s*-elements such as Sr, Y, Zr, Ba, La, Nd, Tc, etc.) by the *s*-process. In the low-mass AGB stars (M < 4 $M_{\odot}$), the $^{13}C(\alpha, n)^{16}O$ reaction is the dominant neutron source (e.g. Abia et al. 2001). In the more massive AGB stars, instead, neutrons are mainly released by the $^{22}Ne(\alpha, n)^{25}Mg$ reaction, resulting in a higher neutron density (up to 10^{13} n/cm^3) and temperature environment than in lower-mass AGB stars (García-Hernández et al. 2006). The Rb produced depends on the probability of the ^{85}Kr and ^{86}Rb capturing a neutron before decaying and acting as branching points (see van Raai et al. 2012, for more details). The probability of this happening depends on the local neutron density (Beer & Macklin 1989). The $^{87}Rb/^{85}Rb$ isotopic ratio is a direct indicator of the neutron density at the production site but it is not possible to distinguish individual ^{87}Rb and ^{85}Rb from stellar spectra (García-Hernández et al. 2006). However, the relative abundance of Rb to other nearby *s*-process elements such as Zr is very sensitive to the neutron density, and so a good discriminant of the stellar mass and the neutron source at the *s*-process site (Lambert et al. 1995; Abia et al. 2001; García-Hernández et al. 2006; van Raai et al. 2012). In other words, [Rb/Zr]<0 is observed in low-mass AGB stars where the main neutron source is the $^{13}C(\alpha, n)^{16}O$ reaction (Plez et al. 1993; Lambert et al. 1995; Abia et al. 2001), while [Rb/Zr]>0 is observed in more massive AGB stars, where the neutrons are mainly released through the $^{22}Ne(\alpha, n)^{25}Mg$ reaction (García-Hernández et al. 2006, 2007a, 2009a).

Chemical abundance analyses using classical MARCS hydrostatic atmospheres (Gustafsson et al. 2008) revealed strong Rb overabundances ($\sim 10^3$-10^5 times solar) and high [Rb/Zr] ratios ($\geqslant$ 3-4 dex) in massive AGB stars (generally very luminous OH/IR stars) of our own Galaxy and the Magellanic Clouds (MC; García-Hernández et al. 2006, 2007a, 2009a). This observationally confirmed for the first time that the ^{22}Ne neutron source dominates the production of *s*-process elements in these stars. However, the extremely high Rb abundances and [Rb/Zr] ratios observed in most the massive stars (and especially in the lower-metallicity MC AGB stars) have posed a Rb problem; such extreme [Rb/Fe] and [Rb/Zr] values are not predicted by the *s*-process AGB models, (van Raai et al. 2012; Karakas et al. 2012), suggesting fundamental problems in our present understanding of AGB nucleosynthesis and/or of the complex extended dynamical atmospheres of these stars (García-Hernández et al. 2009a).

Zamora et al. (2014) constructed new pseudo-dynamical MARCS model atmospheres by considering the presence of a gaseous circumstellar envelope with

a radial wind and applied them to a scriptsize sample of five O-rich AGB stars with different expansion velocities and metallicities. The Rb abundances and [Rb/Zr] ratios obtained were much lower than those obtained with classical hydrostatic models; in better agreement with the AGB nucleosynthesis theoretical predictions. In this chapter, we use the Zamora et al. (2014) pseudo-dynamical model atmospheres to obtain the abundances of Rb and Zr in the sample of massive Galactic AGB stars previously analysed with hydrostatic models (García-Hernández et al. 2006, 2007a). These Rb and Zr abundances are then compared with the more recent AGB nucleosynthesis theoretical predictions available in the literature.

2.2 Sample and observational data

Our sample is composed of 21 massive Galactic AGB stars (most of them very luminous OH/IR stars) previously analysed by García-Hernández et al. (2006, 2007a); we use their high-resolution (R ∼40,000−50,000) optical echelle spectra (we refer to García-Hernández et al. 2006, 2007a, for further observational details)[1]. The signal-to-noise (S/N) ratios achieved in the reduced spectra vary greatly from the blue to the red (typically ∼ 10-20 at 6000 Å and >100 at 8000 Å. The Rb and Zr abundances were determined from the resonant 7800 Å Rb I line and the 6474 Å ZrO bandhead, respectively, by using classical MARCS hydrostatic model atmospheres (García-Hernández et al. 2006, 2007a). The Rb abundances and [Rb/Zr] ratios obtained from this chemical analysis are mostly in the range [Rb/Fe]∼0.6−2.6 dex and [Rb/Zr]∼0.1−2.1 dex. The atmospheric parameters and Rb abundances derived with the hydrostatic models as well as other useful observational information like the OH expansion velocity, variability period, and the presence of Li are listed in Table 2.1.

2.3 Chemical abundance analysis using pseudo-dynamical models

2.3.1 Modified version of the Turbospectrum spectral synthesis code

We used the v12.2 modified version of the spectral synthesis code *Turbospectrum* (Alvarez & Plez 1998; Plez 2012), which considers the presence of a circumstellar gas envelope and a radial wind, as modified by Zamora et al. (2014).

[1]The high-resolution spectra were obtained using the Utrecht Echelle Spectrograph (UES) at the 4.2 m William Herschel Telescope (La Palma, Spain) and the CAsegrain Echelle SPECtrograph (CASPEC) of the ESO 3.6 m telescope (La Silla, Chile) during several observing periods in 1996-97 (see García-Hernández et al. 2007a).

Table 2.1: Atmosphere parameters and Rb abundances (as derived using hydrostatic models) and other selected observational information.

IRAS name	T_{eff} (K)	log g	v_{exp}(OH) (km s^{-1})	Period (days)	Lithium	[Rb/Fe]$_{static}$	S/N at 7800 Å
01085+3022	3000*	−0.5	13	560	yes	2.0	49
04404−7427	3000	−0.5	8	534	...	1.3	68
05027−2158	2800	−0.5	8	368	yes	0.4	418
05098−6422	3000	−0.5	6	394	no	0.1	309
05151+6312	3000	−0.5	15	...	no	2.1	161
06300+6058	3000	−0.5	12	440	yes	1.6	127
07222−2005	3000	−0.5	8	1200	...	0.6	30
09194−4518	3000	−0.5	11	...	...	1.1	25
10261−5055	3000	−0.5	4	317	no	< -1.0	595
14266−4211	2900	−0.5	9	389	no	0.9	106
15193+3132	2800	−0.5	3	360	no	−0.3	266
15576−1212	3000	−0.5	10	415	yes	1.5	91
16030−5156	3000	−0.5	7-14	579	yes	1.3	86
16037+4218	2900	−0.5	4	360	no	0.6	115
17034−1024	3300	−0.5	3-9	346	no	0.2	189
18429−1721	3000	−0.5	7	481	yes	1.2	98
19059−2219	3000	−0.5	13	510	...	2.3	32
19426+4342	3000	−0.5	9	...	...	1.0	19
20052+0554	3000*	−0.5	16	450	yes	1.5	47
20077−0625	3000	−0.5	12	680	...	1.3	19
20343−3020	3000	−0.5	8	349	no	0.9	76

Notes. The stellar parameters, Rb abundances, OH expansion velocities, variability periods and presence of Li are collected from García-Hernández et al. (2006, 2007a) (and references therein). The asterisks indicate that the best fitting T_{eff} in the ZrO 6474 Å spectral region is warmer (3300 K) than that around the Rb I 7800 Å line (García-Hernández et al. 2006, 2007a). Two stars (IRAS 16030−5156 and IRAS 17034−1024) only display the blue-shifted 1612 MHz OH maser peak and we list the range of OH expansion velocities shown by other stars with similar variability periods (García-Hernández et al. 2007a).

The main modifications are the following: (i) The Doppler effect due to the extended atmosphere and velocity field is introduced in the routines that compute the line intensities at the stellar surface; (ii) the source function of the radiative transfer is assumed to be the same as computed in the static case (Gustafsson et al. 2008). The validity of this approximation was tested by comparing with Monte Carlo simulations (see Zamora et al. 2014); (iii) The scattering term of the source function ($\propto \sigma_\lambda J_\lambda$) is not shifted to save computing time and is only incorporated for the continuum. This scattering term is computed as in the static case using the Feautrier method (Nordlund 1984; Gustafsson et al. 2008); and (iv) the velocity field is taken into account through a shift of the absorption coefficient κ_λ; the source function is built using the static $\sigma_\lambda J_\lambda$ and the shifted $\kappa_\lambda B_\lambda$. The emerging intensity is then computed in the observer frame by a direct quadrature of the source function.

2.3.2 Extended atmosphere models

For the analysis of each star in our sample, we adopted the atmosphere parameters from García-Hernández et al. (2006, 2007a), the solar reference abundances by Grevesse et al. (2007) and the pseudo-dyncamic models constructed by Zamora et al. (2014) and described in Chapter 1. The input parameters needed to generate the synthetic spectra are: the effective temperature T_{eff}, surface gravity $logg$, stellar mass M, metallicity z, microturbulent velocity ξ, and C/O ratio, while the output parameters are the chemical abundances of the elements of our interest. In addition, the synthetic spectra are convolved with a gaussian profile which accounts for the instrumental profile and the large-scale motions expected in the stellar atmosphere (macroturbulence, rotation, etc.). The best set of input parameters are selected by comparing the synthetic spectra with the observations at different wavelenghts regions, until a good set of stellar parameters describes the atmosphere of the star García-Hernández et al. (2006, 2007a).

2.3.3 Resulting grids of synthetic spectra

The synthetic spectra are generated with the modified version of *Turbospectrum* by using the extended pseudo-dynamical model atmospheres as input. We constructed a mini-grid of synthetic spectra for each sample star by adopting the atmospheric parameters (e.g. effective temperature, macroturbulence[2])

[2]The synthetic spectra are convolved with a Gaussian profile (with a certain FWHM typically between 250 and 400 mÅ) to account for macroturbulence as well as instrumental profile effects.

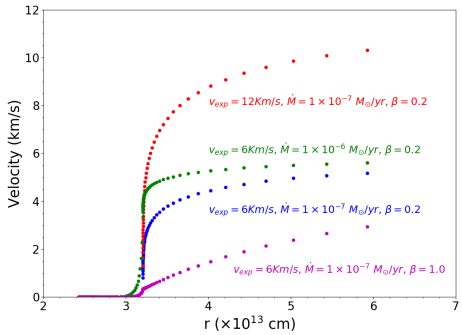

Figure 2.1: Velocity vs. distance from the star in four of our AGB wind models. These velocity laws present different expansion velocities v_{exp}(OH), mass-loss rates $\dot{M}$, and β exponents. The effective temperature T_{eff} = 3000 K, gravity log g = −0.5 and the solar chemical composition are the same in all models.

from García-Hernández et al. (2006, 2007a). Basically, the stellar mass, gravity log g, microturbulent velocity ξ, metallicity [Fe/H], and C/O ratio are fixed to 2 $M_{\odot}$, −0.5 dex, 3 kms^{-1}, 0.0, and 0.5 dex, respectively (we refer to García-Hernández et al. 2007a, for more details). On the other hand, for the mass-loss rate $\dot{M}$ and the exponent β, we use values in the range $\dot{M} \sim 10^{-9}$−$10^{-6} M_{\odot} yr^{-1}$ in steps of 0.5×10^{-1} $M_{\odot} yr^{-1}$ and the range $\beta \sim 0.2 - 1.6$ in steps of 0.2. We have not considered the case where β = 0.0 because the expansion velocity would be constant at any r. We assume the OH expansion velocity (v_{exp}(OH); see Table 2.1) as the terminal velocity because the OH maser emission is found at very large distances from the central star (e.g. Decin et al. 2010). Figure 2.1 shows examples of the β-velocity laws used in our pseudo-dynamical models based on the MARCS hydrostatic models. Finally, for the Rb and Zr abundances, we used [Rb/Fe]$\sim$ −2.6 to +3.0 dex, and [Zr/Fe]$\sim$ −1.0 to +1.0 in steps of 0.1 and 0.25 dex, respectively.

The resulting mini-grid ($\sim$4400 models) is compared to the observed spectrum in order to find the synthetic spectrum that best fits the 7800 Å Rb I line and the 6474 Å ZrO bandhead profiles and their adjacent pseudocontinua. In order to obtain the best fits, we made use of a procedure based on the comparison between synthetic and observed spectra, while in Zamora et al. (2014) the observed spectra were fitted by eye. The method is a modified version of

the standard χ^2 test,

$$\chi^{2*} = \chi^2 \times w = \left(\sum_{i=1}^{N} \frac{[Yobs_i - Ysynth_i(x_1...x_M)]^2}{Yobs_i} \right) \times w, \qquad (2.1)$$

where $Yobs_i$ and $Ysynth_i$ are the observed and synthetic data points, respectively, with N the number of data points, and M the number of free parameters. On the other hand, w is a vector that gives a stronger weight to the detailed spectral profiles of the Rb I line and the ZrO bandhead. This way, the lowest value of χ^{2*} gives us the best fitting synthetic spectrum from the mini-grid for each sample star.

The use of the χ^{2*} test to find the best fits to the observed spectra reveals the presence of important degeneracies in the resulting grids of pseudo-dynamical synthetic spectra; that is, very similar synthetic spectra are obtained from different sets of wind parameters (more details below). Moreover, in some cases (IRAS 04404−7427, IRAS 05027−2158, IRAS 05098−6422, IRAS 06300+6058, IRAS 10261−5055, IRAS 18429−1721, IRAS 19059−2219 and IRAS 20343−3020) the use of the χ^{2*} test is not enough for obtaining the synthetic spectrum that best reproduces the observed one and the best fits have to be found by eye. Unfortunately, the wind model parameters $\dot{M}$ and β are generally not known for stars in our sample (see below), complicating the abundance analysis. Thus, here we study the sensitivity of the synthetic spectra and the abundance results to variations of the stellar and wind parameters.

2.3.4 Sensitivity of the synthetic spectra to variations of the model parameters

Here, we analyse how the variations in stellar (T_{eff}) and wind ($\dot{M}$, β and v_{exp}(OH)) parameters influence the output synthetic spectra. Figures 2.2 and 2.3 show examples of synthetic spectra for different stellar and wind parameters in the spectral regions around the 7800 Å Rb I line and 6474 Å ZrO bandhead, respectively. We note that the fraction of the absorption at 7800 Å due to other species (e.g. TiO) is typically around 20%. We indicate, however, that this has a minor effect in the Rb abundances derived as compared with the sensitivity of the Rb abundances to variations of the stellar and wind parameters. Also, the TiO molecule (the main contributor) is one of the best known molecules to date (McKemmish et al. 2019), as it can be see from our excellent fits to the numerous TiO lines present in our optical spectra.

The Rb I line profile is very sensitive to the wind mass-loss rate $\dot{M}$ (especially for $\dot{M} \geq 10^{-8}$ $M_{\odot} yr^{-1}$); the Rb I line is significantly deeper and blue-

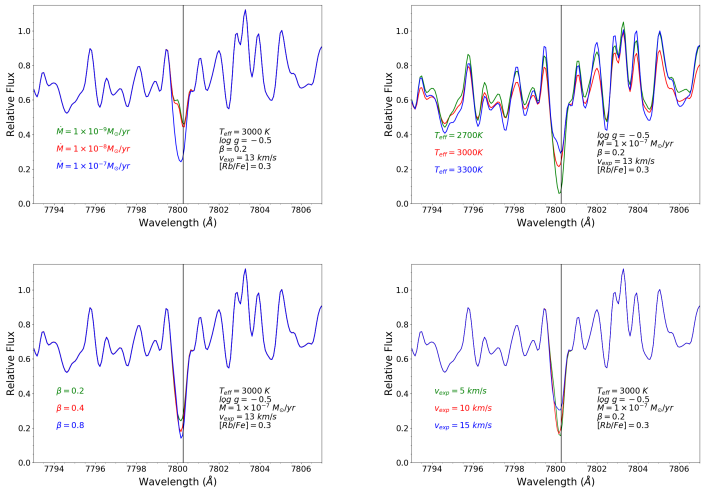

Figure 2.2: Illustrative examples of synthetic spectra for different stellar (T_{eff}) and wind ($\dot{M}$, β, and v_{exp}(OH)) parameters in the spectral region around the 7800 Å Rb I line. The black vertical line indicates the position of the 7800 Å Rb I line.

shifted with increasing $\dot{M}$ (Figure 2.2, top-left panel). However, the Rb I line profile is much less sensitive to changes of the wind velocity-law (β parameter); being only slightly deeper with increasing β (Figure 2.2, bottom-left panel). In addition, for β values higher than ∼1.2 (shallower velocity profiles), the Rb I line profile is not sensitive to variations of the expansion velocity v_{exp}(OH) because the velocity profiles are very similar in our extended model atmosphere (up to $\sim 10^{14}$ cm; see Figure 2.1). Variations in the expansion velocity v_{exp}(OH) mainly affect the blue-shift of the Rb I line and, in addition, for large v_{exp}(OH) values the core of the Rb I line is less deep (Figure 2.2, bottom-right panel). Finally, the Rb I absorption line is stronger with decreasing effective temperature T_{eff} (as expected; Figure 2.2, top-right panel) but this time the wealth of TiO molecular lines and the pseudo-continua are also affected. We note that all these effects (variations in the Rb I profile in terms of depth and blue-shift) are more evident for extreme mass-loss rates ($\dot{M} \geq 10^{-7}$ $M_\odot yr^{-1}$) and higher

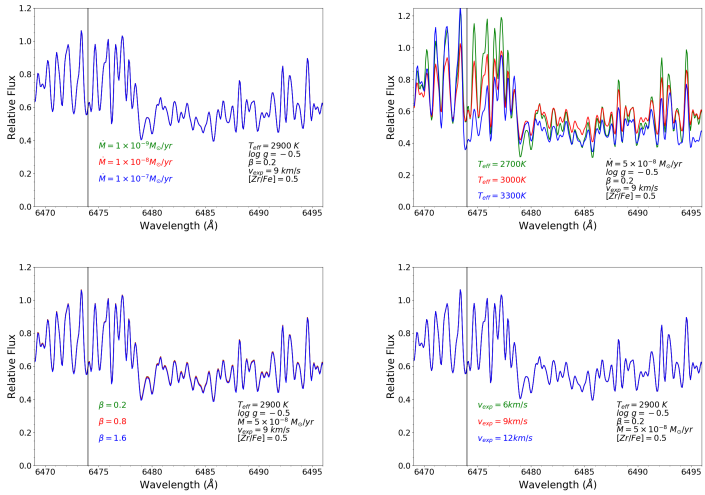

Figure 2.3: Illustrative examples of synthetic spectra for different stellar (T_{eff}) and wind ($\dot{M}$, β, and v_{exp}(OH)) parameters in the spectral region around the 6474 Å ZrO bandhead. The black vertical line indicates the position of the 6474 Å ZrO bandhead.

Rb abundances ([Rb/Fe] $\geq$ 0.4 dex).

On the other hand, the ZrO bandhead profile is not sensitive to the wind parameters $\dot{M}$, β, and v_{exp}(OH) (see Figure 2.3; top-left, bottom-left, and bottom-right panels, respectively). The ZrO bandhead profile (as well as the adjacent TiO lines and pseudo-continuum) are, again as expected, stronger with decreasing T_{eff} (Figure 2.3, top-right panel). This is because ZrO is formed deeper than Rb I in the atmosphere, being much less affected by the circumstellar envelope and radial wind.

2.4 Abundance results

As we have mentioned above, there are important degeneracies in the resulting mini-grids of synthetic spectra for each star. Two synthetic spectra with the same T_{eff}, $logg$ and v_{exp}(OH), but different β, $\dot{M}$, and [Rb/Fe] abundances

could be practically identical in spite of the different wind parameters. This complicates the abundance analysis because the wind model parameters $\dot{M}$ and β are generally not known for stars in our sample. In any case, we can use some observational constraints and previous results on a few similar OH/IR stars to limit the possible variation range of these wind parameters (in particular for the mass-loss rates $\dot{M}$, see below).

Just for a few stars in our sample there are available values of mass-loss rates, $\dot{M}$, from infrared spectra (see Table 2.2). However, these mass-loss rates $\dot{M}$ from 60 μm flux measurements are sistematically larger than those obtained from our fits, except for IRAS 05027−2158, where the order of magnitude of the mass-loss rates $\dot{M}$ is the same. In addition, by using multiple rotationally excited lines of both ^{12}CO and ^{13}CO, De Beck et al. (2010) provide accurate mass-loss rates $\dot{M}$ for a large sample of Galactic AGB stars. Unfortunately, only one star (IRAS 20077−0625) from our present sample of Rb-rich OH/IR massive AGB stars is included in their work and we cannot fit this star with our pseudo-dynamical models (see below). There are seven massive AGB stars of OH/IR type (WX Psc, V669 Cas, NV Aur, OH 26.5+0.6, OH 44.8−2.3, IRC −10529 and OH 104.9+2.4) previously studied in the optical by García-Hernández et al. (2007a). Their variability periods and mass-loss rates range from 552 to 1620 days[3] and from 1.8×10^{-5} $M_{\odot}yr^{-1}$ to 9.7×10^{-6} $M_{\odot}yr^{-1}$, respectively. Interestingly, all these stars are extremely obscured in the optical, being too red or without optical counterpart[4]; they likely already have entered the superwind phase. Thus, the $\dot{M}$ values in optically obscured OH/IR AGB stars can be taken as upper limits (i.e. $<10^{-6}$ $M_{\odot}yr^{-1}$) for our sample of OH/IR massive AGB stars with optical counterparts; that is, with useful spectra around the 7800 Å Rb I line. Indeed, we generally find that lower mass-loss rates ($\sim10^{-7}$−10^{-8} $M_{\odot}yr^{-1}$) give superior fits to the observed Rb I line profiles. Mass-loss rates of $\sim10^{-6}$ $M_{\odot}yr^{-1}$ (or higher) give strong Rb I absorption lines for solar Rb abundances (see also Zamora et al. 2014) with the consequence that all stars in our sample of OH/IR massive AGB stars would be Rb-poor. By combining the variability periods from Table 2.1 and the mass-loss rates estimated from the Rb I line profiles (mainly in the range $\sim10^{-7}$−10^{-8} $M_{\odot}yr^{-1}$; Table 2.3) into the AGB mass-loss formula by Vassiliadis & Wood (1993) (their Eq. (5)), we obtain reasonable current stellar masses in the range

[3]The variability periods of our sample stars are also lower, from ∼320 to 580 days (only two stars display periods in excess of 580 days; Table 2.1).

[4]The only exception is WX Psc as already noted by Zamora et al. (2014). This star (with a mass-loss rate of $\sim1.8\times10^{-5}$ $M_{\odot}yr^{-1}$, De Beck et al. 2010; Justtanont et al. 2013) has an extremely faint optical counterpart. The S/N around 7800 Å is too low for an abundance analysis but a strong Rb I absorption line is clearly detected in its optical spectrum.

Table 2.2: Mass-loss rates from 60 μm flux measurements for various sample stars.

IRAS name	$\dot{M}$ ($M_{\odot}yr^{-1}$)	Ref.
01085+3022	3.3×10^{-6}	1
04404−7427	2.9×10^{-6}	1
05027−2158	1.5×10^{-7}	1
05098−6422	5.0×10^{-7}	1
06300+6058	5.3×10^{-6}	2
15193+3132	1.1×10^{-7}	3
19059−2219	1.0×10^{-5}	2
20077−0625	1.5×10^{-5}	2
20343−3020	8.7×10^{-7}	1

References: (1) Whitelock et al. (1994); (2) Jura & Kleinmann (1989); (3) Jura & Kleinmann (1992).

$\sim$2.5−6 $M_{\odot}$. In Table 2.3 we show the mass-loss rates obtained from the best spectral fits ($\dot{M}_{fit}$) and the current stellar masses by using the mass-loss expression from Vassiliadis & Wood (1993). In addition, we have explored the mass loss relation for winds of pulsating O-rich AGB stars adopted by Miller Bertolami (2016) in the range of masses 0.8 < M < 4 $M_{\odot}$. However, we consider that our sample of O-rich AGB stars are more massive (M > 4-5 $M_{\odot}$) than the range of masses used by Miller Bertolami (2016), so we have decided not to apply those relation.

The β parameter in our models (only up to $\sim10^{14}$ cm from the photosphere; Figure 2.1) cannot be directly compared with other estimations of this parameter in the literature (e.g. Decin et al. 2010; Danilovich et al. 2015), which map many outer regions in the circumstellar envelope and that usually obtain relatively high and uncertain values ($0 \leq \beta \leq 5.0$). However, the effect of the β parameter on our synthetic spectra is minor compared to the mass-loss rate $\dot{M}$ and we keep it as a free parameter in our abundance analysis. We note also that the velocity profiles are very similar in our extended model atmosphere for $\beta \geq 1.2$; that is, the Rb I line profile is not more sensitive to variations of the expansion velocity and the abundance results are very similar for $\beta \geq 1.2$. We generally find better fits with low β values (or steeper velocity profiles; see Table 2.4).

Table 2.3: Mass-loss rates estimated from the best spectral fits and current stellar masses obtained by using the Vassiliadis & Wood (1993) mass-loss formula (their Eq. (5)).

IRAS name	Period (days)	$\dot{M}$ ($M_{\odot}yr^{-1}$)	$M_{current}$ ($M_{\odot}$)
01085+3022	560	1.0×10^{-7}	4.6
04404−7427	534	1.0×10^{-7}	4.3
05027−2158	368	1.0×10^{-7}	2.7
05098−6422	394	5.0×10^{-7}	2.4
05151+6312	...	1.0×10^{-8}	...
06300+6058	440	1.0×10^{-7}	3.4
07222−2005	1200	...	...
09194−4518	...	...	...
10261−5055	317	1.0×10^{-9}	3.8
14266−4211	389	5.0×10^{-8}	3.1
15193+3132	360	1.0×10^{-9}	4.2
15576−1212	415	1.0×10^{-8}	3.9
16030−5156	579	1.0×10^{-8}	5.6
16037−1024	360	1.0×10^{-7}	2.6
17034−1024	346	1.0×10^{-8}	3.2
18429−1721	481	1.0×10^{-8}	4.6
19059−2219	510	5.0×10^{-8}	4.3
19426+4342	...	...	...
20052+0554	450	5.0×10^{-7}	2.9
20077−0625	680	...	...
20343−3020	349	1.0×10^{-9}	4.1

As mentioned above, the parameters of the hydrostatic models providing the best fit to the observations and the Rb abundances derived are shown in Table 2.1. The static models use the solar abundances from Grevesse & Sauval (1998) for computing the Rb abundances (García-Hernández et al. 2006, 2007a), while our pseudo-dynamical models use the more recent solar abundances from Grevesse et al. (2007). In Zamora et al. (2014) the Rb abundances from static models using Grevesse & Sauval (1998) and Grevesse et al. (2007) were compared, and the Rb abundances obtained agree within ∼0.2 dex in most cases.

Figure 2.4 shows that our pseudo-dynamical atmosphere models reproduce the observed 7800 Å Rb I line profile much better than the classical hydrostatic models in four sample stars (we refer to Appendix A for the remainder of the sample stars). On the other hand, the Zr abundances derived from the extended models are similar to those obtained with the hydrostatic models because the 6474 Å ZrO bandhead is formed deeper in the atmosphere and is less affected by the radial velocity field (Zamora et al. 2014). We could obtain the Rb and Zr abundances (or upper limits) for 17 sample stars. The remainder of our sample stars (IRAS 07222−2005, IRAS 09194−4518, IRAS 19426+4342 and IRAS 20077−0625) seem to display different Rb I line profiles (e.g. with more than one circumstellar contribution or anomalously broad profiles with red-extended wings; e.g. Figure 2.5) that cannot be completely reproduced by our present version of the spectral synthesis code. In the two stars (IRAS 07222−2005 and IRAS 09194−4518) shown in Figure 2.5 we cannot fit the two Rb I components (circumstellar and photospheric) at the same time; for example, we could only partially fit the blue-shifted circumstellar component using larger mass-loss rates ($>10^{-6}\ M_{\odot} yr^{-1}$). Curiously, these two stars present the largest periods (see Table 2.1) and they may be the most extreme and evolved stars in our sample, where our extended models do not work so well (e.g. due to even more extended atmospheres). It is not completely clear, however, if the observed profiles are real because these four sample stars have the lowest-quality spectra ($S/N < 30$ at 7800 Å; Table 2.1).

For the two sample stars with unknown OH expansion velocity, IRAS 16030−5156 and IRAS 17034−1024, we explore the velocity range displayed by other stars with similar variability periods (see Table 2.1). Similar fits can be obtained for v_{exp}(OH) ∼ 7−12 and 7−9 kms^{-1} (in combination with sligthly different wind parameters) for IRAS 16030−5156 and IRAS 17034−1024, respectively, and we thus adopt average velocities of 10 and 8 kms^{-1}, respectively, in the abundance analysis (Table 2.4).

Table 2.4 shows the atmospheric and wind parameters as well as the Rb and Zr abundances (or upper limits) from the best fits to the observed spectra when the wind parameters $\dot{M}$ and β are not fixed. In most cases, the best

fit is obtained for both low β ($\sim$0.2) and $\dot{M}$ ($\sim 10^{-9}$-10^{-7} $M_{\odot}$ yr^{-1}) values. The new Rb abundances obtained from extended models are lower than those obtained using the hydrostatic models, and the difference is larger for stars with higher hydrostatic Rb abundances. In addition, this difference is smaller for lower v_{exp}(OH) and increases with increasing v_{exp}(OH), as expected. On the other hand, in the case of Zr we obtain upper limits mostly between 0.0 and +0.25 dex, as derived from the hydrostatic models. Figure 2.6 displays the hydrostatic and pseudo-dynamical Rb abundances versus the OH expansion velocity for the wind parameters that provide the best fits (Table 2.4). We plot the Rb abundances versus the expansion velocity because the v_{exp}(OH) can be used as a mass indicator independent of the distance in OH/IR stars (García-Hernández et al. 2007a). In addition, in Figure 2.6 we have marked the Li-rich stars (García-Hernández et al. 2007a) by squares. About half of the stars with v_{exp}(OH) $>$ 6 km/s are Li-rich and most of these stars are also the more Rb-rich ones. We get pseudo-dynamical abundances lower than the hydrostatic ones and a worse correlation between[5] the Rb abundances and v_{exp}(OH); the Rb-v_{exp}(OH) relationship is flatter (with a higher degeneration) for the pseudo-dynamical case (see also Sect. 2.5).

[5]The correlation coefficients are $r = 0.84$ and 0.54 for the hydrostatic and pseudo-dynamic cases, respectively.

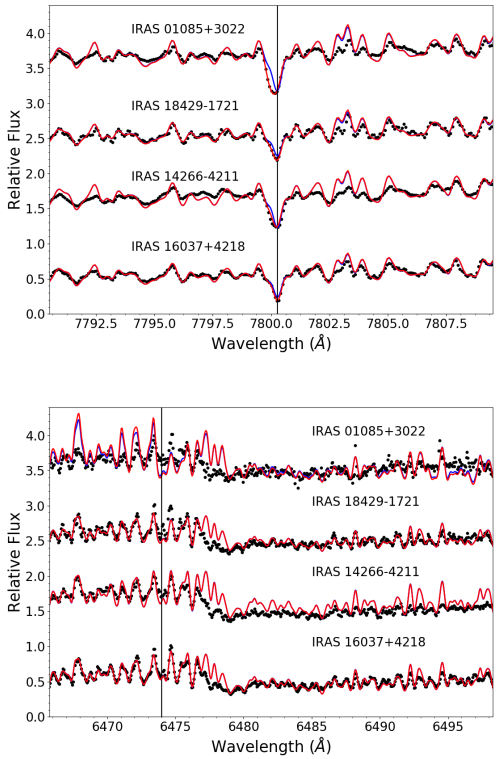

Figure 2.4: The Rb I 7800 Å (*top panel*) and ZrO 6474 Å (*bottom panel*) spectral regions in massive Galactic AGB stars. The pseudo-dynamical models (red lines) that best fit the observations (black dots) are shown in four sample stars. For comparison, the hydrostatic models are also displayed (blue lines). The location of the Rb I line and the ZrO bandhead are indicated by black vertical lines.

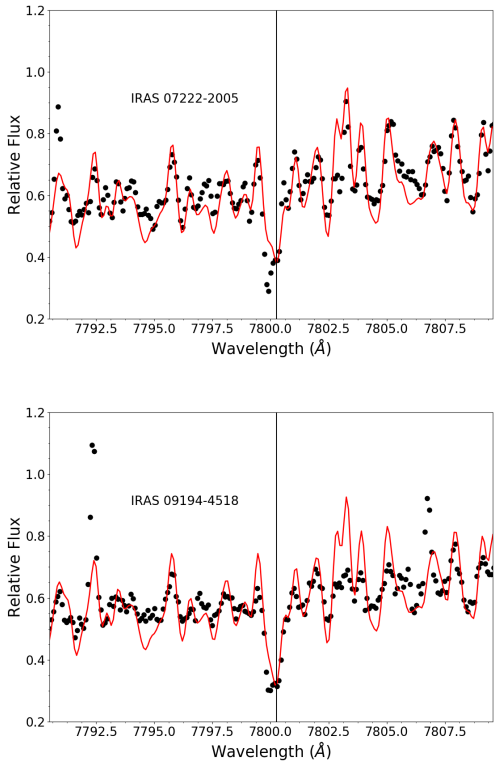

Figure 2.5: IRAS 07222−2005 (*top panel*) and IRAS 09194−4518 (*bottom panel*) display two components (circumstellar and photospheric) in the 7800 Å Rb I line (black line) and cannot be reproduced by our present version of the spectral synthesis code. The red line shows the pseudo-dynamical synthetic spectrum that gives a good fit to the photospheric component only.

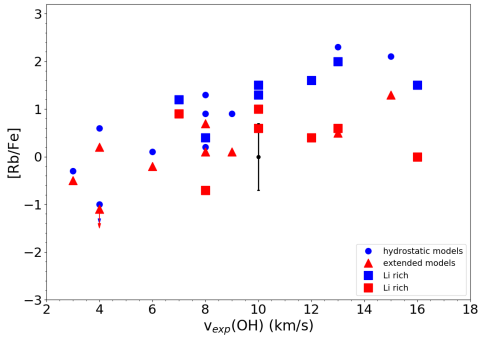

Figure 2.6: Rb abundances derived both with hydrostatic (blue dots) and pseudo-dynamical model atmospheres (red triangles) with best-fit parameters plotted against the OH expansion velocity. The Li-rich stars are indicated by squares. A typical error bar of ±0.7 dex is also displayed.

Table 2.4: Atmosphere parameters and best-fit Rb pseudo-dynamical abundances for the listed wind parameters $\dot{M}$ and β. The asterisks indicate that the best fitting T_{eff} in the ZrO 6474 Å spectral region is warmer (3300 K) than the one around the Rb I 7800 Å line (García-Hernández et al. 2006, 2007a).

IRAS name	T_{eff} (K)	log g	β	$\dot{M}$ ($M_\odot$ yr^{-1})	v_{exp}(OH) (km s^{-1})	[Rb/Fe]$_{static}$	[Rb/Fe]$_{dyn}$	[Zr/Fe]$_{dyn}$
01085+3022	3000*	−0.5	0.2	1.0×10^{-7}	13	2.0	0.6	≤ 0.0
04404−7427	3000	−0.5	0.2	1.0×10^{-7}	8	1.3	0.1	≤ 0.0
05027−2158	2800	−0.5	0.4	1.0×10^{-7}	8	0.4	−0.7	≤ +0.5
05098−6422	3000	−0.5	1.4	1.0×10^{-8}	6	0.1	−0.2	≤ +0.25
05151+6312	3000	−0.5	1.0	1.0×10^{-8}	15	2.1	1.3	≤ +0.25
06300+6058	3000	−0.5	0.2	1.0×10^{-7}	12	1.6	0.4	≤ 0.0
07222−2005	3000	−0.5	...	...	8	0.6	...	...
09194−4518	3000	−0.5	...	...	11	1.1	...	...
10261−5055	3000	−0.5	0.2	1.0×10^{-9}	4	< −1.0	< −1.1	≤ +0.25
14266−4211	2900	−0.5	0.2	5.0×10^{-8}	9	0.9	0.1	≤ 0.0
15193+3132	2800	−0.5	1.6	1.0×10^{-9}	3	−0.3	−0.5	≤ 0.0
15576−1212	3000	−0.5	0.2	1.0×10^{-8}	10	1.5	1.0	≤ 0.0
16030−5156	3000	−0.5	0.2	1.0×10^{-8}	10	1.3	0.6	≤ +0.25
16037+4218	2900	−0.5	1.2	1.0×10^{-8}	4	0.6	0.2	≤ +0.25
17034−1024	3300	−0.5	0.8	1.0×10^{-8}	8	0.2	−0.7	≤ 0.0
18429−1721	3000	−0.5	0.2	1.0×10^{-8}	7	1.2	0.9	≤ +0.25
19059−2219	3000	−0.5	0.2	1.0×10^{-7}	13	2.3	0.5	≤ +0.25
19426+4342	3000	−0.5	...	...	9	1.0	...	...
20052+0554	3000*	−0.5	0.2	5.0×10^{-7}	16	1.5	0.0	≤ 0.0
20077−0625	3000	−0.5	...	...	12	1.3	...	...
20343−3020	3000	−0.5	1.2	1.0×10^{-9}	8	0.9	0.7	≤ 0.0

Notes. The asterisks indicate that the best fitting T_{eff} in the ZrO 6474 Å spectral region is warmer (3300 K) than the one around the Rb I 7800 Å line (García-Hernández et al. 2006, 2007a). We have checked the sensitivity of the derived abundances to small changes in the model atmosphere parameters ($\Delta T_{eff} = \pm100$ K, $\Delta\beta = 0.2$, $\Delta log(\dot{M}/M_\odot \mathrm{yr}^{-1}) = 0.5$, $\Delta v_{exp}(\mathrm{OH}) = 5$ km s^{-1}). The dominant sources of uncertainties are $\dot{M}$ and T_{eff} for dominant sources of uncertainties are $\dot{M}$ and T_{eff} for Rb and Zr, respectively, which result in error bars of ±0.7 and ±0.3 dex, respectively. In the hydrostatic case, the formal Rb uncertainties (quoted by García-Hernández et al. (2006)) due to changes of all the atmosphere parameters are ±0.8 dex.

Table 2.5: Atmosphere parameters and Rb pseudo-dynamical abundances with $\beta = 0.2$ and $\beta = 1.2$, respectively. The asterisks indicate that the best fitting T_{eff} in the ZrO 6474 Å spectral region is warmer (3300 K) than the one around the Rb I 7800 Å line (García-Hernández et al. 2006, 2007a).

IRAS name	T_{eff} (K)	log g	β	$\dot{M}$ ($M_\odot$ yr^{-1})	v_{exp}(OH) (km s^{-1})	[Rb/Fe]$_{static}$	[Rb/Fe]$_{dyn}$	[Zr/Fe]$_{dyn}$
01085+3022	3000*	−0.5	0.2	1.0×10^{-7}	13	2.0	0.6	≤ 0.0
			1.2	1.0×10^{-7}			0.3	
04404−7427	3000	−0.5	0.2	1.0×10^{-7}	8	1.3	0.1	≤ 0.0
			1.2	1.0×10^{-7}			0.1	
05027−2158	2800	−0.5	0.2	1.0×10^{-7}	8	0.4	−0.6	≤ +0.5
			1.2	1.0×10^{-7}			−1.1	
05098−6422	3000	−0.5	0.2	1.0×10^{-8}	6	0.1	−0.2	≤ +0.25
			1.2	5.0×10^{-7}			−2.1	
05151+6312	3000	−0.5	0.2	5.0×10^{-7}	15	2.1	0.0	≤ +0.25
			1.2	5.0×10^{-7}			−0.5	
06300+6058	3000	−0.5	0.2	1.0×10^{-7}	12	1.6	0.4	≤ 0.0
			1.2	1.0×10^{-7}			0.3	
07222−2005	3000	−0.5	...	...	8	0.6	...	...
09194−4518	3000	−0.5	...	...	11	1.1	...	...
10261−5055	3000	−0.5	0.2	1.0×10^{-9}	4	< −1.0	< −1.1	≤ +0.25
			1.2	1.0×10^{-9}			< −1.1	
14266−4211	2900	−0.5	0.2	5.0×10^{-8}	9	0.9	0.1	≤ 0.0
			1.2	1.0×10^{-7}			−0.4	≤ −0.25
15193+3132	2800	−0.5	0.2	1.0×10^{-9}	3	−0.3	−0.4	≤ 0.0
			1.2	1.0×10^{-9}			−0.4	
15576−1212	3000	−0.5	0.2	1.0×10^{-8}	10	1.5	1.0	≤ 0.0
			1.2	1.0×10^{-8}			0.9	
16030−5156	3000	−0.5	0.2	1.0×10^{-8}	10	1.3	0.6	≤ +0.25
			1.2	1.0×10^{-7}			−0.4	
16037+4218	2900	−0.5	0.2	1.0×10^{-8}	4	0.6	0.5	≤ +0.25
			1.2	1.0×10^{-8}			0.2	
17034−1024	3300	−0.5	0.2	1.0×10^{-8}	8	0.2	−0.7	≤ 0.0
			1.2	1.0×10^{-8}			−0.8	
18429−1721	3000	−0.5	0.2	1.0×10^{-8}	7	1.2	0.9	≤ +0.25
			1.2	5.0×10^{-7}			−1.0	≤ 0.0
19059−2219	3000	−0.5	0.2	1.0×10^{-7}	13	2.3	0.5	≤ +0.25
			1.2	5.0×10^{-8}			0.5	
19426+4342	3000	−0.5	...	...	9	1.0	...	...
20052+0554	3000*	−0.5	0.2	5.0×10^{-7}	16	1.5	0.0	≤ 0.0
			1.2	5.0×10^{-7}			−0.7	
20077−0625	3000	−0.5	...	...	12	1.3	...	...
20343−3020	3000	−0.5	0.2	1.0×10^{-9}	8	0.9	0.7	≤ 0.0
			1.2	1.0×10^{-9}			0.7	

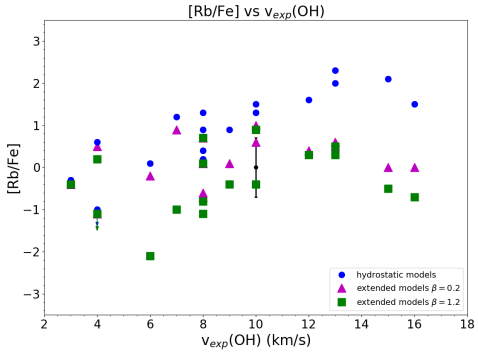

Figure 2.7: Rb abundances derived both with hydrostatic (blue dots) and extended model atmospheres with $\beta = 0.2$ (magenta triangles) and $\beta = 1.2$ (green squares) plotted against the OH expansion velocity.

Also, we carried out several tests with different β and $\dot{M}$ values in order to check the sensitivity of the derived abundances to variations of the wind parameters. In Table 2.5 we present the wind parameters and Rb abundances obtained when fixing β to 0.2 and 1.2. Basically, the Rb abundances are lower in the $\beta = 1.2$ case because a higher β deepens the Rb I 7800 Å line for the same Rb abundance (see Figure 2.2); in a few cases, however, the $\dot{M}$ of the best fit also changes, further affecting the determination of the Rb abundance. The Zr abundances (or upper limits) are similar in most cases; the upper limits only change when the $\dot{M}$ is not the same for the $\beta = 0.2$ and 1.2 cases. Figure 2.7 represents the Rb abundances obtained versus v_{exp}(OH) for $\beta = 0.2$ and β = 1.2. By comparing the Rb abundances from Figure 2.6 and Figure 2.7, it is clear that the Rb abundances are slightly lower in the $\beta = 1.2$ case. Moreover, the correlation between the pseudo-dynamical Rb abundances and v_{exp}(OH) for different β values is worse (e.g. flatter) than the hydrostatic case. In addition, the dispersion seems to be larger for the $\beta = 1.2$ case.

On the other hand, Figure 2.8 displays the Rb results when $\dot{M}$ is fixed to 10^{-8}, 10^{-7} and 10^{-6} $M_{\odot}$ yr^{-1}. This could be equivalent to considering that our AGB sample stars are at a similar evolutionary stage in terms of mass loss; of course we have a strong degeneracy between the progenitor masses and mass loss/evolutionary stage. In the particular case of the Li-rich AGB stars,

statistical arguments suggest that these stars should have a narrow initial mass range (Di Criscienzo et al. 2016); 4-5 or 5-6 $M_{\odot}$ according to the most recent ATON (Di Criscienzo et al. 2016) or Monash (Karakas & Lugaro 2016) AGB nucleosynthesis models, respectively. The current stellar masses from Table 2.3 show, however, that there is a complicated interplay (degeneracy) between Li enhancement, progenitor mass, and mass-loss rate and that the progenitor mass range of these stars may actually be broader; for example, their current stellar mass and Li abundance ranges are ∼2.7-5.6 $M_{\odot}$ and ∼logε(Li)∼0.7-2.6 dex. Figure 2.8 shows that the Rb abundances decrease with increasing $\dot{M}$ and the dispersion of the Rb abundances is much lower when fixing $\dot{M}$. The slopes (and correlation coefficients) of the Rb-v_{exp}(OH) correlations are more similar to the ones obtained with hydrostatic models. The Rb abundances from extended models approach the hydrostatic ones with decreasing $\dot{M}$ (both sets of Rb abundances are identical for $\dot{M} \leq 10^{-9}$ $M_{\odot}$ yr^{-1}) because the atmosphere is less extended with decreasing $\dot{M}$, as expected.

Finally, we fixed $\dot{M}$ and β, which could be equivalent to considering that our AGB sample stars have the same mass-loss stage and velocity profile. Figure 2.9 displays the pseudo-dynamical Rb abundances versus v_{exp}(OH) for $\beta = 0.2$ and $\dot{M}$ values of 10^{-8}, 10^{-7} and 10^{-6} $M_{\odot}$ yr^{-1}. The Rb results, when fixing both $\dot{M}$ and β, are very similar (with a slightly tighter correlation with v_{exp}(OH)) to those obtained when only fixing $\dot{M}$ (see Figure 2.8) because $\beta = 0.2$ is the most common value obtained from the best spectral fits (all wind parameters free); an exception is the AGB star IRAS 15193+3132 (with the lowest v_{exp}(OH) and high β) for which only an upper limit to the Rb abundance ([Rb/Fe]≤0.7) could be obtained because the pseudo-dynamical model does not converge for such an unusual combination of wind parameters ($\dot{M}$=10^{-6} $M_{\odot}$ yr^{-1}; β=0.2; v_{exp}(OH)=3 km s^{-1}) coupled with [Rb/Fe]<0.7 dex (see Figure 2.9).

Figure 2.10 displays the [Rb/Fe] abundances from the best spectral fits versus the variability periods P. As mentioned above, our sample is composed of AGB stars of different progenitor masses and evolutionary stages. Most stars with $P > 400$ days are Li-rich and present some Rb enhancement[6], which suggests that, on average, these stars are more massive stars experiencing HBB and/or more evolved stars (because of the longer periods) than the group of non Li-rich (and generally Rb-poor) stars with $P < 400$ days. The stars IRAS 05027−2158 (P=368 days) and IRAS 20343−3020 (P=349 days) are exceptions in the latter group. IRAS 05027−2158 is slightly Li-rich and Rb-poor,

[6]The only exceptions are IRAS 04404−7427 and IRAS 19059−2219, whose optical counterparts are too red to estimate their Li abundances (i.e. the S/N at 6708 Å is too low; see García-Hernández et al. 2007a)

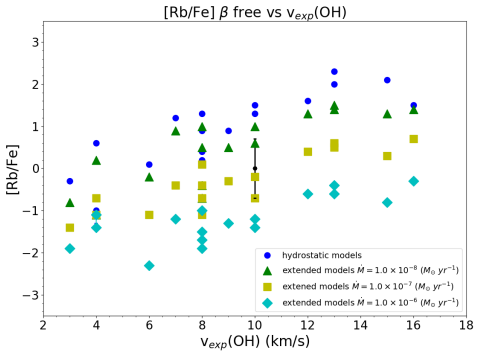

Figure 2.8: Rb abundances vs. the expansion velocity (v_{exp}(OH)) for extended model atmospheres with $\dot{M} = 10^{-8}$, 10^{-7} and 10^{-6} $M_{\odot}$ yr^{-1} (green triangles, yellow squares and cyan diamonds, respectively) in comparison with those obtained from hydrostatic models (blue dots).

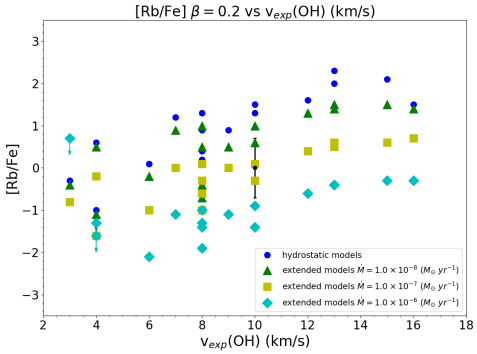

Figure 2.9: Rb abundances vs. the expansion velocity (v_{exp}(OH)) for extended model atmospheres with $\beta = 0.2$ and $\dot{M} = 10^{-8}$, 10^{-7} and 10^{-6} $M_{\odot}$ yr^{-1} (green triangles, yellow squares and cyan diamonds, respectively) in comparison with those obtained from hydrostatic models (blue dots).

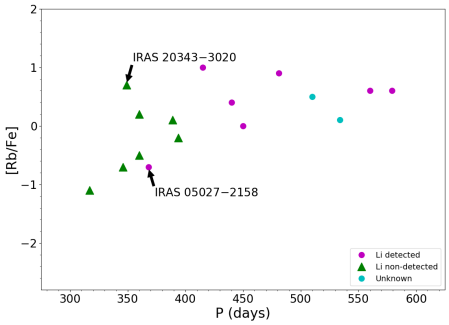

Figure 2.10: [Rb/Fe] pseudo-dynamical abundances versus variability period (P). The Li-rich and Li-poor stars are marked with magenta dots and green triangles, respectively. The two stars where Li could not be estimated are marked with cyan dots (see text).

suggesting that it is a relatively massive AGB star (say ∼3.5−4.5 $M_{\odot}$[7]) at the beginning of the TP phase (e.g. in an inter-pulse period immediately before or after the super Li-rich phase) but is not evolved enough for efficient Rb production (García-Hernández et al. 2013). On the other hand, IRAS 20343−3020 is slightly Rb-rich and Li-poor, which suggests a more advanced evolutionary stage and a slightly higher initial mass (say ∼4.0−5 $M_{\odot}$) than IRAS 05027−2158 (we refer to Fig. 1 in García-Hernández et al. 2013).

2.5 Comparison with AGB nucleosynthesis models

In Figure 2.11 we compare our new [Rb/Fe] abundances and [Rb/Zr] ratios with solar metallicity massive (3−9 $M_{\odot}$) AGB predictions from several nucleosynthesis models: van Raai et al. (2012), Karakas et al. (2012), Karakas & Lugaro (2016) (Monash), Pignatari et al. (2016) (NuGrid/MESA) and Cristallo et al. (2015) (FRUITY[8]). The predicted [Rb/Fe] abundances and [Rb/Zr] ratio

[7]The initial mass for HBB activation is model dependent; i.e. at solar metallicity HBB is activated at ∼3.5 and 4.5 $M_{\odot}$ depending on the mass-loss and convection prescriptions used in the models (see e.g. García-Hernández et al. 2013, for more details).

[8]FUll-Network Repository of Updated Isotopic Tables and Yields: http:// fruity.oateramo.inaf.it/.

ranges are 0.00−1.35 and −0.45−0.52 dex, respectively.

The Monash models (van Raai et al. 2012; Karakas et al. 2012; Karakas & Lugaro 2016) use the stellar evolutionary sequences calculated with the Monash version of the Mount Stromlo Stellar Structure Program (Frost & Lattanzio 1996), which uses the Vassiliadis & Wood (1993) mass-loss prescription on the AGB. A post-processing code is used to obtain in detail the nucleosynthesis of a large number of species, including the *s*-process abundances. Due to convergence difficulties, the stellar evolution models used in the calculations are not always evolved until the end of the superwind phase and synthetic models have been used to estimate the effect of remaining TPs and to completely remove the envelope. We refer the reader to van Raai et al. (2012), Karakas et al. (2012) and Karakas & Lugaro (2016) for more details about the theoretical models. Here, we only report on the main differences between these models: i) The use of different nuclear networks; that is, the total number of nuclear species considered and the values of some reaction rates and neutron-capture cross-sections (see below); and ii) the use by Karakas et al. (2012) of a modified Vassiliadis & Wood (1993) mass-loss prescription, which delays the beginning of the superwind phase until the pulsation period reaches values of 700-800 days (instead of the value of 500 days used in the other models), resulting in a higher Rb production.

The NuGrid/MESA and FRUITY models assume AGB mass-loss prescriptions, nuclear physics inputs and treatments of convection different from the Monash models. In particular, the Bloecker (1995) and Straniero et al. (2006) mass-loss formulae for the AGB phase are assumed by the NuGrid/MESA and FRUITY models, respectively. Furthermore, these models produce self-consistently the ^{13}C neutron source as a result of the different convective boundary mixing scheme and treatments of the convective borders, while in the Monash models the mixing required to produce the ^{13}C neutron source is included in a parametrised way during the post processing and is typically not included in massive AGB stars, following theoretical (Goriely & Siess 2004) and observational indications (García-Hernández et al. 2013) (we refer also to Pignatari et al. 2016; Cristallo et al. 2015; Karakas & Lugaro 2016, for more details). In relation to the main results, i) the NuGrid/MESA solar metallicity massive AGB models are qualitatively similar to the Monash models in that HBB and light *s*-process element production (of the elements from Rb to Zr) are seen at the stellar surface, the latter due to the activation of the ^{22}Ne neutron source and the subsequent operation of the TDU; and ii) the FRUITY solar metallicity massive AGB models are different to the Monash and NuGrid/MESA models because these models experience very inefficient TDU, hence the signature of the nucleosynthesis due to the ^{22}Ne neutron source is

not visible at the stellar surface.

Figure 2.11 shows that the FRUITY massive AGB model predicts final [Rb/Fe] < 0.15, which does not explain the observed range of Rb abundances and [Rb/Zr] ratios; specifically the [Rb/Zr] ratios remain negative for all masses. Another difference between the FRUITY models and the Monash and NuGrid models is that the FRUITY models do not predict HBB to occur in AGB stars unless the metallicity is very low; at least ten times lower than solar. However, spectroscopic observations of massive AGB stars demonstrate that they experience HBB; as evidenced by i) strong Li overabundances observed in massive AGB stars in the Galaxy (Fe/H=0.0; e.g. García-Hernández et al. 2007a, 2013), the Magellanic Clouds (Fe/H=−0.7-−0.3; e.g. Plez et al. 1993; Smith et al. 1995; García-Hernández et al. 2009a) and the dwarf galaxy IC 1613 (Fe/H=−1.6; e.g. Menzies et al. 2015); and ii) N enhancements and low $^{12}C/^{13}C$ ratios in Magellanic Cloud Li-rich massive AGBs (e.g. Plez et al. 1993; McSaveney et al. 2007). The lack of HBB in the FRUITY predictions is also at odds with the observations of the so-called type-I planetary nebulae in very different metallicity environments and galaxies; which are expected to be the descendants of HBB massive AGB stars based on their strong N and He overabundances (see e.g. Stanghellini et al. 2006; Karakas et al. 2009; Leisy & Dennefeld 1996; García-Rojas et al. 2016, and references therein).

It is to be noted here that the several Monash AGB models (van Raai et al. 2012; Karakas et al. 2012; Karakas & Lugaro 2016) mentioned above notably use different rates for the $^{22}Ne(\alpha, n)^{25}Mg$ reaction, which drives the production of *s*-process elements in massive AGB stars. In particular, Karakas & Lugaro (2016) use the $^{22}Ne(\alpha, n)^{25}Mg$ reaction from Iliadis et al. (2010), neutron-capture cross-section of the Zr isotopes (Lugaro et al. 2014), and a more extended nuclear network of 328 species (from H to S, and then from Fe to Bi). The van Raai et al. (2012) models, instead, use a nuclear network of 166 species (up to Nb) and the $^{22}Ne(\alpha, n)^{25}Mg$ reaction rate from Karakas et al. (2006), while Karakas et al. (2012) explored different networks (166, 172 and 320 species) and $^{22}Ne(\alpha, n)^{25}Mg$ reaction rates; from Karakas et al. (2006), Iliadis et al. (2010) and Angulo et al. (1999), NACRE.

The van Raai et al. (2012) models (from 4 to 6.5 $M_\odot$ at $Z = 0.02$; Fig. 2.11) show that both the [Rb/Fe] abundances and [Rb/Zr] ratios increase with the initial mass of the AGB star, as the star becomes hotter and the $^{22}Ne(\alpha, n)^{25}Mg$ reaction is more efficiently activated. However, the [Rb/Fe] abundances from the last computed TP are too low (ranging from 0.0 to 0.26 dex). The corresponding Rb abundances ([Rb/Fe]∼0.0−1.0 dex) from the synthetic evolution calculations cover most of the Rb abundances observed; although they cannot explain the star IRAS 05151+6312 with [Rb/Fe]=1.3 dex. Such high Rb abun-

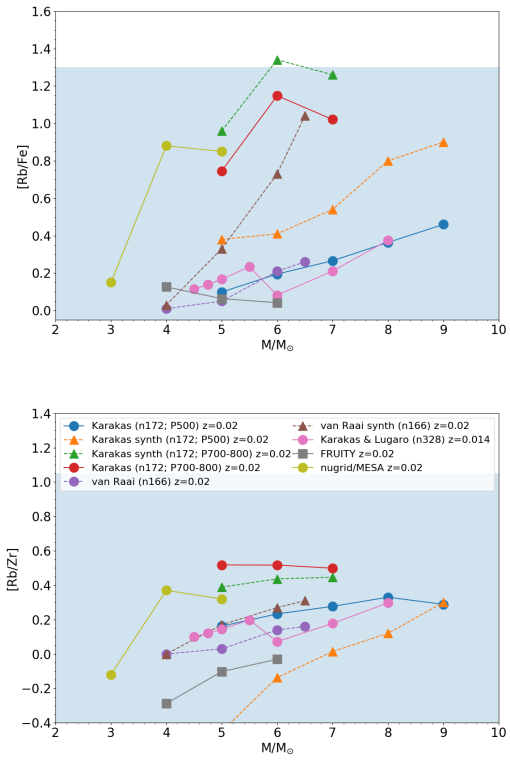

Figure 2.11: Model predictions from van Raai et al. (2012), Karakas et al. (2012), Karakas & Lugaro (2016), FRUITY database and Pignatari et al. (2016): Stellar mass vs. [Rb/Fe] (*top panel*) and [Rb/Zr] (*bottom panel*). The abundances from the last computed thermal pulse and from the synthetic evolution calculations are shown with dots and triangles, respectively. P represents the period for the beginning of the superwind phase and n is the number of species in the nucleosynthesis network. The shaded regions mark the range of the new Rb abundances and [Rb/Zr] ratios obtained in our sample with extended models.

dances can be reached by the synthetic calculations of the solar metallicity 6 and 7 $M_\odot$ AGB models with delayed superwinds of Karakas et al. (2012) when using the faster NACRE rate for the $^{22}Ne(\alpha, n)^{25}Mg$ reaction. Finally, the Karakas & Lugaro (2016) models (from 4.5 to 8 $M_\odot$ at $Z = 0.014$[9]; Fig. 2.11) predict lower Rb abundances than the Karakas et al. (2012) models of the same mass and similar metallicity, mostly due to the implementation of the delayed superwind and the use of the NACRE rate in Karakas et al. (2012).

The NuGrid/MESA models (from 3 to 5 $M_\odot$ at $Z = 0.02$; Fig. 2.11) reproduce the observed [Rb/Fe] and [Rb/Zr] ranges, up to 0.9 and 0.4 dex, respectively. However, we note that only in the 5 $M_\odot$ case do the NuGrid/MESA models see signature of HBB and predict O-rich stars. The 3 and 4 $M_\odot$ cases become C-rich stars and do not experience HBB, which is at odds with our sample of O-rich stars (García-Hernández et al. 2006).

Regarding the [Rb/Zr] ratios, obviously also in this case the higher [Rb/Zr] ratios are obtained from the models with delayed superwind (P = 700-800), however, these [Rb/Zr] ratios are still lower than our observed values. The maximum value from the AGB models is [Rb/Zr] = 0.52 for M = 5 $M_\odot$, and the maximum value from our observations is [Rb/Zr] = 1.05. A possible explanation is that Zr could be depleted into dust (e.g. van Raai et al. 2012; Zamora et al. 2014), producing the differences between the theoretical and observational [Rb/Zr] ratios. Observations of other *s*-process elements belonging to the same first peak as Rb and Zr, and with condensation temperature lower than the Zr one, Zr will help to clarify this mismatch.

[9] According to the more recent solar abundances from Asplund et al. 2009.

3

Circumstellar effects on the Li and Ca abundances in massive Galactic AGB stars

Based on
V. Pérez-Mesa et al. 2019, A&A, 623, A151

ABSTRACT - Here we are interested in clarifying the role of the extended atmosphere in the case of Li and Ca. Li is an important indicator of HBB while the total Ca abundances in these stars could be affected by neutron captures. We report new Li and Ca abundances in a larger sample of massive Galactic O-rich AGB stars by using more-realistic extended atmospheres that consider the presence of a gaseous circumstellar envelope and radial wind. Li abundances had been previously studied with hydrostatic models, while the Ca abundances have been determined here for the first time. The Li abundances derived with the pseudo-dynamical models are very similar to those obtained from hydrostatic models, with no difference for Ca. The new Li abundances confirm the Li-rich nature of the sample stars, supporting the activation of the HBB in massive Galactic AGB stars. Most sample stars display Ca abundances consistent with nucleosynthesis models for solar metallicity massive AGB stars. A minority of the sample stars seem to show a significant Ca depletion and possible explanations are offered to explain their apparent and unexpected Ca depletion.

3.1 Introduction

As already mentioned in Chapter 1, the more massive AGB stars (M > 4-5 $M_{\odot}$) are O-rich (C/O < 1) due to the activation of the so-called HBB process. HBB converts ^{12}C into ^{13}C and ^{14}N through the CN cycle via proton captures at the base of the convective envelope, preventing the formation of a carbon star (e.g. Sackmann & Boothroyd 1992; Mazzitelli et al. 1999). The HBB models (e.g. Sackmann & Boothroyd 1992; Mazzitelli et al. 1999) also predict the production of ^{7}Li via the ^{7}Be transport mechanism (Cameron & Fowler 1971), where Li should be detectable at the stellar surface regions (at least for a short time; see below).

Regarding the *s*-process, the ^{13}C(α,n)^{16}O reaction is the preferred neutron source in low-mass AGB stars (e.g. Lambert et al. 1995; Abia et al. 2001). The ^{22}Ne(α,n)^{25}Mg dominates the production of *s*-process elements in the more massive (M > 4-5 $M_{\odot}$) AGB stars (e.g. García-Hernández et al. 2006, 2009a, 2013). A different *s*-elements pattern is expected depending on the dominant neutron source. The free neutrons can drive neutron captures also on the light elements including the Ca isotopes. While the total abundance of Ca is predicted not to vary in AGB stars by more than roughly 10% (e.g. Karakas & Lugaro 2016), the isotopic composition of Ca can be affected, mostly resulting in an overproduction of ^{46}Ca relatively to the other Ca isotopes (see also Wasserburg et al. 2015). Furthermore, the models predict the production of the radionuclide ^{41}Ca (half life $\sim$ 0.1 Myr), which can also be carried up to the stellar surface from the inter-shell region via the TDU, with maximum ^{41}Ca/^{40}Ca ratios at the stellar surface of the order of 10^{-4} (see e.g. Trigo-Rodríguez et al. 2009; Lugaro et al. 2012, 2014). This isotope decays via electron captures and is also destroyed by neutron captures via ^{41}Ca(n,α)^{38}Ar and ^{41}Ca(n,p)^{41}K. All of these interaction channels are uncertain (see Lugaro et al. 2018, for a discussion), so the production of ^{41}Ca could in principle lead to a decrease in the total Ca abundance. However, the cross section of the production channel of ^{41}Ca, the ^{40}Ca(n,γ)^{41}Ca reaction is well determined (Dillmann et al. 2009) and we do not expect major changes in the model predictions if any of the input physics related to ^{41}Ca will be modified.

High-resolution optical spectroscopic surveys of very luminous Galactic OH/IR stars show that most of the stars with long periods and high OH expansion velocities are Li-rich, which confirm them as truly massive HBB-AGB stars. The strong Rb over-abundances coupled with mild Zr enhancements (García-Hernández et al. 2006, 2007a) confirm the activation of the ^{22}Ne neutron source in the more massive O-rich AGB stars. More recently, observations of a few massive Galactic AGB stars at the beginning of the TP phase have

confirmed that HBB is strongly activated at the early AGB stages and that the *s*-process is dominated by the ^{22}Ne neutron source (García-Hernández et al. 2013). The latter stars are super Li-rich (logε(Li) up to ∼4 dex) together with the lack of *s*-process elements (Rb, Zr and Tc), as predicted by the theoretical models (e.g. van Raai et al. 2012; Karakas et al. 2012). On the other hand, the Ca abundances have never been previously measured in massive Galactic AGB stars; we report here, for the first time, the Ca abundances in a sample of such stars.

Previously, we studied in Chapter 2 the circumstellar effects on Rb and Zr abundances by applying the Zamora et al. (2014) pseudo-dynamical model atmospheres in a sample of massive Galactic O-rich AGB stars. In this chapter, we explore the circumstellar effects on the Li and Ca abundances to the sample of massive Galactic AGB stars of García-Hernández et al. (2007a) and the super Li-rich AGBs of García-Hernández et al. (2013). These new Li and Ca abundances are then compared with several AGB nucleosynthesis theoretical predictions: ATON (Ventura & D'Antona 2009), Monash (Karakas & Lugaro 2016), NuGrid/MESA (Ritter et al. 2018) and FRUITY (Cristallo et al. 2015) models.

3.2 Observational data

We have used the high S/N (at least ∼30−50 around Li I 6708 Å and Ca I 6463 Å; see below) and high-resolution (R∼50,000) optical (∼4000−9000 Å) echelle spectra of the García-Hernández et al. (2006) sample (15 stars) of massive Galactic AGB stars, for which Rb and Zr abundances could be derived by us (see Chapter 2) as well as for the García-Hernández et al. (2007a) sub-sample (12 stars) of Li-detected stars not analysed in the study of the Rb and Zr abundances (see Chapter 2). In addition, we have analysed the high-quality optical echelle spectra of the three (RU Cyg, SV Cas and R Cen) massive Galactic AGB stars, two of them (SV Cas and R Cen) super Li-rich, reported by García-Hernández et al. (2013). The high-resolution spectra were obtained using the Utrecht Echelle Spectrograph (UES) at the 4.2 m William Herschel Telescope, the CAsegrain Echelle SPECtrograph (CASPEC) at the ESO 3.6 m telescope, the Tull spectrograph at the 2.7 m Harlan J. Smith (HJS) Telescope and the UVES spectrograph at the ESO-VLT (Table 3.1; see García-Hernández et al. 2007a, 2013, for more observational details). Our final sample is thus composed of 30 stars; for all of which there exist previous hydrostatic Li abundance determinations. It is to be noted here that our sub-sample of stars with previous Rb abundance determinations slightly differs from the sample

Table 3.1: Log of the spectroscopic observations.

IRAS name	Spectral Range (Å)	Telescope	Instrumentation	Resolution	Ref.
01085+3022	4700-10300	4.2m WHT	UES	50,000	1
02095−2355	5300-9400	4.2m WHT	UES	50,000	1
05027−2158	6000-8200	3.6m ESO	CASPEC	40,000	1
05098−6422	6000-8200	3.6m ESO	CASPEC	40,000	1
05151+6312	5300-9400	4.2m WHT	UES	50,000	1
05559+3825	4700-10300	4.2m WHT	UES	50,000	1
06300+6058	4700-10300	4.2m WHT	UES	50,000	1
07304−2032	6000-8200	3.6m ESO	CASPEC	40,000	1
09429−2148	6000-8200	3.6m ESO	CASPEC	40,000	1
10261−5055	6000-8200	3.6m ESO	CASPEC	40,000	1
11081−4203	6000-8200	3.6m ESO	CASPEC	40,000	1
14266−4211	6000-8200	3.6m ESO	CASPEC	40,000	1
14337−6215	6000-8200	3.6m ESO	CASPEC	40,000	1
15193+3132	5300-9400	4.2m WHT	UES	50,000	1
15211−4254	6000-8200	3.6m ESO	CASPEC	40,000	1
15255+1944	5300-9400	4.2m WHT	UES	50,000	1
15576−1212	6000-8200	3.6m ESO	CASPEC	40,000	1
16030−5156	6000-8200	3.6m ESO	CASPEC	40,000	1
16037+4218	5300-9400	4.2m WHT	UES	50,000	1
16260+3454	5300-9400	4.2m WHT	UES	50,000	1
17034−1024	4700-10300	4.2m WHT	UES	50,000	1
18413+1354	4700-10300	4.2m WHT	UES	50,000	1
18429−1721	5300-9400	4.2m WHT	UES	50,000	1
19129+2803	4700-10300	4.2m WHT	UES	50,000	1
19361−1658	4700-10300	4.2m WHT	UES	50,000	1
20052+0554	4700-10300	4.2m WHT	UES	50,000	1
20343−3020	4700-10300	4.2m WHT	UES	50,000	1
RU Cyg	3650-9500	2.7m HJS	Tull spectragh	60,000	
SV Cas	3650-9500	2.7m HJS	Tull spectragh	60,000	2
R Cen	3770-10500	VLT ESO	UVES	50,000	2

References: (1) (García-Hernández et al. 2007a); (2) (García-Hernández et al. 2013).

analyzed in Chapter 2 because the observed spectra are extremely red and the S/N ratios achieved for a given star can strongly vary from the blue to the red spectral regions (e.g. 10−20 at Ca I 6463 Å while >50−100 at Rb I 7800 Å; see also below); that is, six stars analyzed in the previous chapter display a too low S/N at Li I 6708 Å to estimate their Li abundances and were removed from the present sample.

We first carried out an exhaustive study of the Li and Ca absorption spectral lines that can be useful for the extraction of the Li and Ca abundances in these stars. As previously found by García-Hernández et al. (2007a), we find the Li I 6708 Å line to be the best one for the abundance analysis; for example, we discarded the subordinate and weaker Li I 8126 Å line because the synthetic spectra do not properly reproduce the observed stellar pseudo-continuum in this spectral region due to strong contamination by telluric lines and still unknown opacity contributors (García-Hernández et al. 2007a). Regarding the Ca absorption lines, we checked the strongest Ca I lines like those at 6122, 6162, 6439, 6463 and 6573 Å as well as the Ca II triplet (∼ 8500 Å) at longer wavelengths (see Figure 3.1). The Ca I 6463 Å line turned out to be the best Ca abundance indicator. This is because the synthetic fits around the Ca I 6463 Å line (i.e. the stellar pseudo-continuum) are much better than for the rest of Ca I lines; the stronger Ca I 6573 Å line also displays saturation effects. As we have mentioned in the Section 3.1, the isotopic Ca composition is theoretically expected to be affected by neutron captures. The Ca isotope ratios cannot be measured from the atomic Ca absorption lines (the atomic lines are intrinsically too broad; even at very high resolutions). To facilitate our Ca measurement from atomic lines, we explored in addition the possibility of detecting the most intense CaH (Shayesteh et al. 2013; Alavi & Shayesteh 2018) and CaO (Yurchenko et al. 2016) bandheads (around ∼6850-6950 and 8650-8850 Å, respectively) in the optical spectra of our sample stars. Unfortunately, spectral syntheses show that no CaH and CaO molecular lines are detectable in these spectral regions, which are completely dominated by TiO bands.

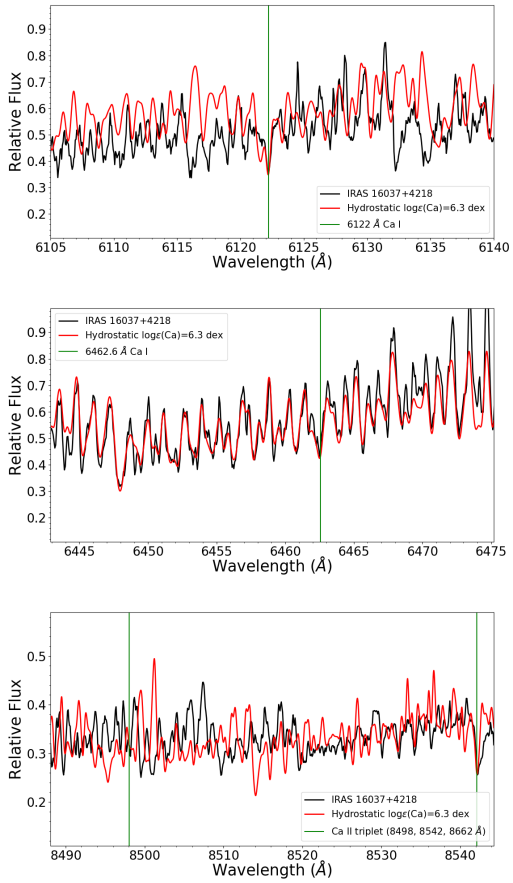

Figure 3.1: Observed spectrum of IRAS 16037+4218 (black lines) and the best hydrostatic fits (red lines) around the 6122 (*top panel*), 6463 (*middle panel*) and 8520 (bottom panel) Å spectral regions. The green vertical lines indicate the position of the Ca I 6122.217 Å (*top panel*), Ca I 6462.567 Å (*middle panel* and two lines of the Ca II triplet 8498.023-8542.091-8662.141 Å (*bottom panel*).

Table 3.2: Atmosphere parameters and Li abundances (derived using hydrostatic models) and other selected observational information.

IRAS name	T_{eff} (K)	log g	v_{exp}(OH) (km s^{-1})	Ref.	Period (days)	Ref.	log $\varepsilon(Li)_{static}$
01085+3022	3300	−0.5	13	1	560	1	2.4
02095−2355	3300	−0.5	12†	...	659	2	1.6
05027−2158	2800	−0.5	8	2	368	1	1.1
05098−6422	3000	−0.5	6	3	394	3	≤ -1.0
05151+6312	3000	−0.5	15	3	628	4	< 0.0
05559+3825	2900	−0.5	12†	6	590	5	0.6
06300+6058	3000	−0.5	12	3	440	6	0.7
07304−2032	2700	−0.5	7	4	509	1	0.9
09429−2148	3300	−0.5	12	3	650	1	2.2
10261−5055	3000	−0.5	4	2	317	1	≤ -1.0
11081−4203	3000	−0.5	8†	2	332	8	1.3
14266−4211	2900	−0.5	9	2	389	8	≤ 0.0
14337−6215	3300	−0.5	20	5	...	...	2.4[1]
15193+3132	2800	−0.5	3	3	360	1	≤ 0.0
15211−4254	3300	−0.5	11	2	...	...	2.3
15255+1944	2900	−0.5	7	3	425	1	1.0
15576−1212	3000	−0.5	10	3	415	1	1.1
16030−5156	3000	−0.5	10†	2	579	9	1.5
16037+4218	2900	−0.5	4	2	360	10	≤ -1.0
16260+3454	3300	−0.5	12	3	475	1	2.7
17034−1024	3300	−0.5	8†	2	346	1	≤ 0.0
18413+1354	3300	−0.5	15	6	590	5	1.8
18429−1721	3000	−0.5	7	2	481	8	1.2
19129+2803	3300	−0.5	11†	2	420	10	3.1[1]
19361−1658	3000	−0.5	8	2	...	...	1.9
20052+0554	3300	−0.5	16	7	450	5	2.6
20343−3020	3000	−0.5	8	2	349	1	≤ -1.0
RU Cyg	3000	−0.5	12†	...	442	11	2.0
SV Cas	3000	−0.5	12†	...	456	11	3.5
R Cen	3000	−0.5	5†	...	251	11	4.3

† These stars only display a single peak in the 1612 MHz OH maser. Thus, in the abundance analysis, we adopted the average OH expansion velocities from the velocity values displayed by the other sample stars with similar variability periods. [1]The line is resolved in two components (circumstellar and photospheric) and the abundance obtained corresponds to the photospheric one.

References for the OH expansion velocities: (1) Chengalur et al. (1993); (2) te Lintel Hekkert et al. (1991); (3) te Lintel Hekkert et al. (1989); (4) Sivagnanam et al. (1989); (5) Sevenster et al. (1997); (6) Slootmaker et al. (1985); (7) Lewis (1994). References for the periods: (1) Combined General Catalogue of Variable Stars (GCVS), Kholopov et al. (1998); (2) Richards et al. (2012); (3) Whitelock et al. (1994); (4) Woźniak et al. (2004); (5) Jones et al. (1990); (6) Lockwood (1985); (7) Groenewegen & de Jong (1998); (8) AAVSO International Variable Star Index, Watson et al. (2006); (9) General Catalogue of Variable Stars (GCVS), Samus' et al. (2017); (10) Jiménez-Esteban et al. (2006), (11) García-Hernández et al. (2013).

Thus, the Li and Ca abundances were determined from the Li I 6708 Å and Ca I 6463 Å lines, respectively, by using extended model atmospheres developed by group (see Chapter 2 and Zamora et al. 2014, for further information). The atmospheric parameters (T_{eff} and log$g$), additional observational information (variability period and OH expansion velocity) and the Li abundance derived from hydrostatic models are listed in Table 3.2 for our sample stars (see García-Hernández et al. 2007a, 2013, for more details).

3.3 Pseuso-dynamical models

In the chemical abundance analysis, we have followed the same methodology described in Chapter 2. In short, we have used the v12.2 modified version of the spectral synthesis code *Turbospectrum* (Alvarez & Plez 1998; Plez 2012), in which the presence of a circumstellar gas envelope and a radial wind are considered. In the analysis of the stars in our sample, we have assumed the atmosphere parameters (e.g. T_{eff}, log$g$, C/O, [Fe/H], macroturbulence) from García-Hernández et al. (2007a, 2013) and the solar abundances from Grevesse et al. (2007). Hydrodynamical wind models for AGB stars have been developed through the years (see the review by Höfner & Olofsson 2018, and references therein). Recent pulsation-enhanced dust-driven outflow type models include time-dependent gas dynamics and dust formation, with polychromatic radiative transfer (e.g. Eriksson et al. 2014; Höfner et al. 2016). Their predictive power for a particular star is, however, limited by the use of free parameters, for example, the piston velocity and amplitude driving the pulsations. We therefore chose to use generic empirical models, based on observational determinations of the velocity-law and simple physical hypotheses. The pseudo-dynamical models were constructed from the original MARCS hydrostatic model structure and the atmosphere radius was extended by a wind out to approximately five stellar radii and a radial velocity field. We compute the stellar wind following mass conservation, radiative thermal equilibrium, and a classical β-velocity law (see Chapter 2 and references therein for more details).

We adopted the atmospheric parameters from García-Hernández et al. (2006, 2007a, 2013), to generate a mini-grid of synthetic spectra for each sample star. Some parameters are fixed: stellar mass M = 2 $M_{\odot}$[1], gravity log $g = -0.5$, microturbulent velocity $\xi = 3$ km/s, metallicity [Fe/H] = 0.0 and C/O = 0.5 dex (see García-Hernández et al. 2007a, for more details). However, for the mass-

[1]The stellar mass was, in all cases, selected to be 2 $M_{\odot}$ because the temperature and pressure structure of the model atmosphere is pratically identical for a 1 $M_{\odot}$ and 10 $M_{\odot}$ model atmosphere and the output synthetic spectra are not sensitive to the mass of the star (see Fig. 1 in Plez 1990).

loss rate $\dot{M}$ and β parameters, we use values between $\dot{M} \sim 10^{-9} - 10^{-6} M_{\odot} yr^{-1}$ [2] in steps of 0.5×10^{-1} $M_{\odot} yr^{-1}$ and $\beta \sim 0.2 - 1.6$ in steps of 0.2, respectively. Finally, for the Li and Ca abundances we used values between log $\varepsilon(Li) \sim$ 0.0 to +2.8 dex and log $\varepsilon(Ca) \sim$ +5.0 to +7.0 dex, in steps of 0.1 dex. The parameters of the synthetic spectra that best fit the 6708 Å Li I and the 6463 Å Ca I profiles and their adjacent pseudocontinua are listed in Table 3.3.

For the sub-sample of stars (15 stars) analyzed in Chapter 2 we have used the stellar and wind parameters obtained from the Rb I 7800 Å spectral region fits for consistency and because the synthetic spectra are much less sensitive to variations of the model parameters in the Li I 6708 Å and Ca I 6463 Å spectral regions (see Subsection 3.3.1 below).

3.3.1 Sensitivity of the synthetic spectra to variations of the model parameters

We have analysed the influence of variations in the stellar (T_{eff}) and wind ($\dot{M}$, β and v_{exp}(OH)) parameters in the output synthetic spectra. Figures 3.2 and 3.3 show, respectively, synthetic spectra in the spectral regions around the 6708 Å Li I and 6463 Å Ca I lines for different stellar and wind parameters.

The Li I profile is not very sensitive to the wind parameters ($\dot{M}$, β and v_{exp}(OH)). The Li I line is only slightly stronger, with increasing $\dot{M}$ (Figure 3.2; top-left panel) and β (Figure 3.2; bottom-left panel), while it is slightly weaker with increasing v_{exp}(OH) (Figure 3.2; bottom-right panel). In addition, the Li I absorption line is stronger with decreasing T_{eff} (Figure 3.2; top-right panel), with the pseudo-continuum (e.g. the TiO molecular bands) also being affected, as expected (see e.g. García-Hernández et al. 2007a). In the Ca case, the sensitivity of the synthetic spectra to variations in $\dot{M}$, β, and v_{exp}(OH) (Figure 3.3; top-left, bottom-left and bottom-right panel, respectively) is even smaller than the Li case. The Ca I 6463 Å spectral region displays TiO molecular bands weaker than the Li I 6708 Å spectral region and, consequently, the Ca I line and the pseudo-continuum are less affected by T_{eff} variations (Figure 3.3; top-right panel) than in the Li I region.

3.4 Abundance results

The parameters of the best fits of García-Hernández et al. (2006, 2007a, 2013) to the observations and the hydrostatic Li abundances are listed in Table 3.2.

[2] Massive AGB stars with mass-loss rates higher than 10^{-6} $M_{\odot} yr^{-1}$ are completely obscured in the optical, while our sample stars, still visible in the optical, should have lower mass-loss rates (see Chapter 2 and references therein for more details).

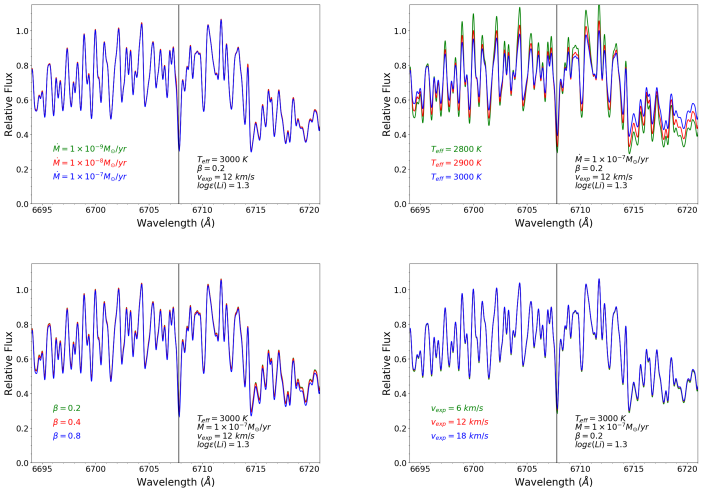

Figure 3.2: Illustrative examples of synthetic spectra for different stellar (T_{eff}) and wind ($\dot{M}$, β, and v_{exp}(OH)) parameters in the spectral region around the 6708 Å Li I line. The gravity log $g = -0.5$ is the same in all the spectra. The black vertical line indicates the position of the 6708 Å Li I line.

In these fits, the static models have used the solar abundances from Grevesse & Sauval (1998) for computing the Li abundances, while the new pseudo-dynamical models and the hydrostatic values shown in Table 3.3 use the more recent solar abundances from Grevesse et al. (2007). The Li hydrostatic abundances obtained by using Grevesse & Sauval (1998) and Grevesse et al. (2007) are practically the same.

In Figure 3.4 we display the hydrostatic and pseudo-dynamical fits in the 6708 Å Li I and 6463 Å Ca I regions in four sample stars. The pseudo-dynamical models are similar to the hydrostatic ones, and properly reproduce the Li and Ca regions. The Li and Ca line profiles are not strongly affected by the presence of a circumstellar envelope and a radial wind. The rest of spectral fits are shown in Appendix B. In addition, Figure 3.5 displays in more detail the Li and Ca regions for some sample stars, showing that the Ca I line is less sensitive (but still useful) to abundance variations than the Li one. In seven stars (IRAS

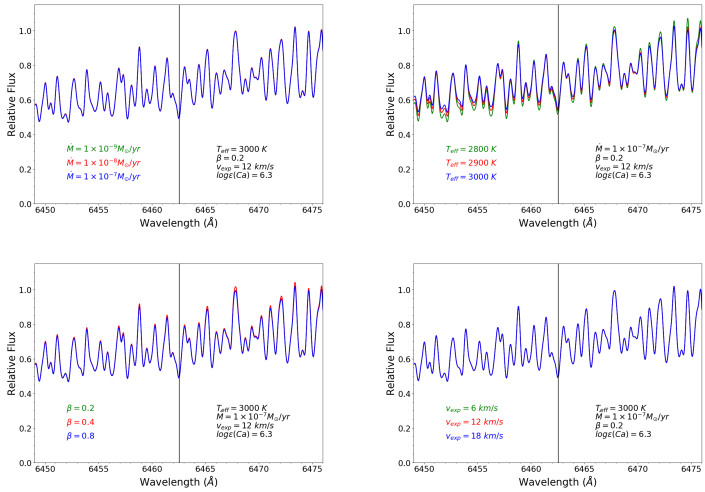

Figure 3.3: Illustrative examples of synthetic spectra for different stellar (T_{eff}) and wind ($\dot{M}$, β, and v_{exp}(OH)) parameters in the spectral region around the 6462.6 Å Ca I line. The gravity log $g = -0.5$ is the same in all the spectra. The black vertical line indicates the position of the 6462.6 Å Li I line.

02095−2355, IRAS 09429−2148, IRAS 15211−4254, IRAS 16260+3454, IRAS 17034−1024, IRAS 18413+1354 and IRAS 19129+2803) the best spectral fit is different in the Li and Ca regions. In all cases, around the 6708 Å Li I line the best spectral fits give $T_{eff} = 3300$ K, while around the 6463 Å Ca I line the best spectral fits provide cooler T_{eff} of 3000 K. A similar finding, this time when comparing the Li I 6708 Å and Rb I 7800 Å regions was previously found by García-Hernández et al. (2006, 2007a).

In addition, for some sample stars in which the OH expansion velocity is unknown (IRAS 02095−2355, IRAS 05559+3825, IRAS 11081−4203, IRAS 16030−5156, IRAS 17034−1024, IRAS 19129+2803, RU Cyg, SV Cas and R Cen), we explored the OH expansion velocity range displayed by other sample stars with similar variability periods. Due to the similar spectral fits that are obtained for slightly different OH expansion velocities, for these stars we thus adopted the average OH expansion velocities from the values displayed by the

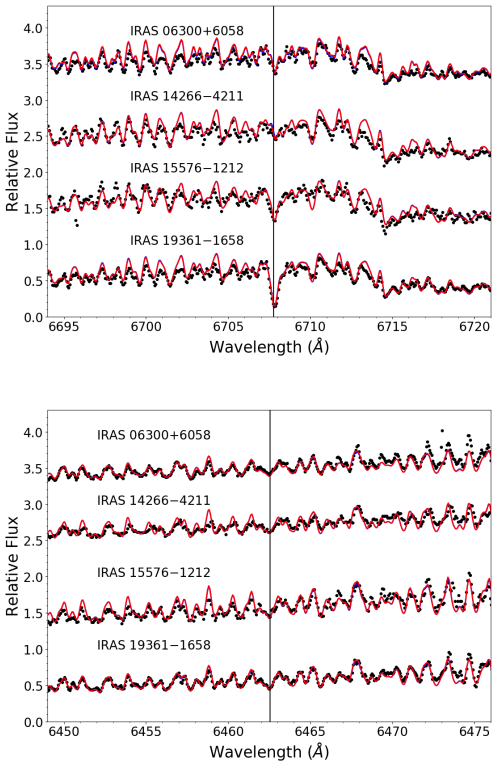

Figure 3.4: Li I 6708 Å (*top panel*) and Ca I 6463 Å (*bottom panel*) spectral regions in four massive Galactic AGB stars. The hydrostatic models (blue lines) and the pseudo-dynamical models (red lines) that best fit the observations (black dots) are shown. The location of the Li I and the Ca I lines are indicated by black vertical lines.

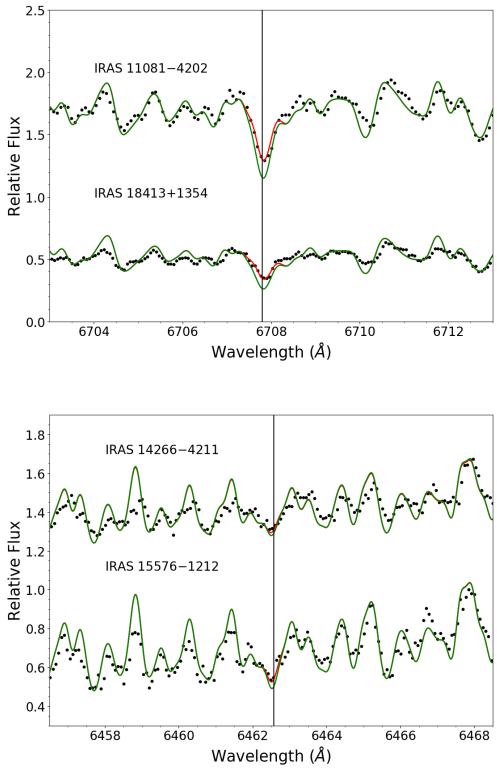

Figure 3.5: A magnification of the Li I 6708 Å (*top panel*) and Ca I 6463 Å (*bottom panel*) spectral regions. The pseudo-dynamic models (red lines) that best fits the observations (black dots) are shown together with the corresponding synthetic spectra for Li and Ca abundances 0.5 dex higher (green lines).

sample stars with similar periods (see Table 3.2).

The atmospheric and wind parameters as well as the Li and Ca abundances (or upper limits) from the best fits to the observed spectra are shown in Table 3.3. The new Li abundances determined from the extended models are very similar to those obtained with the hydrostatic models (see Table 3.3). A maximum difference, between the hydrostatic and dynamical abundances ($\Delta(\log\varepsilon(\mathrm{Li}))_{static-dynamic}$), of +0.3 dex is found for IRAS 20052+0554 and R Cen, while an average difference of +0.18 dex is found in our entire AGB sample. This indicates that the Li content in these stars is not strongly affected by the presence of a circumstellar envelope. We note here that the latter number does not take into account the four stars (IRAS 05098−6422, IRAS 10261−5055, IRAS 16037+4218, and IRAS 20343−3020) for which we get more conservative pseudo-dynamic Li upper limits ($\leq$0.0 dex) than from the hydrostatic models ($\leq$-1.0 dex). In addition, the Ca abundances from the hydrostatic and pseudo-dynamical models are practically identical and the presence of a circumstellar envelope does not at all affect the derived Ca abundances.

We have estimated the uncertainties in the derived Li and Ca abundances for the sample stars. For this, we have made small changes in the atmosphere parameters ΔT_{eff} = ±100 K, $\Delta\log\, g$ = ±0.5, ΔZ = ±0.2, Δt = ±0.5 km s^{-1} and $\Delta FWHM$ = ±50 mÅ for the hydrostatic models, and also in the wind parameters $\Delta\beta$ = ±0.2, $\Delta log(\dot{M}/M_{\odot}\mathrm{yr}^{-1})$ = ±0.5 and Δv_{exp}(OH) = ±5 km s^{-1} for the pseudo-dynamic models. These small changes result in Li formal errors of ±0.3 and ±0.2 dex for the hydrostatic and pseudo-dynamic abundances, respectively, while the estimated Ca formal uncertainties are ±0.5 dex for both the hydrostatic and pseudo-dynamic abundances.

3.5 Non-LTE effects on the Li I and Ca I lines

Due to the fact that the classical hydrostatic and our pseudo-dynamical synthetic spectra are constructed by considering a local thermodynamic equilibrium (LTE) treatment in the (extended) stellar atmosphere, we have explored the possible non-LTE (NLTE) effects on the 6708 Å Li I and 6463 Å Ca I lines in order to clarify the sign and magnitude of the corrections to be applied to the hydrostatic and pseudo-dynamic Li and Ca abundances.

Table 3.3: Atmosphere parameters and best-fit Li and Ca pseudo-dynamical abundances for the sample of massive AGB stars.

IRAS name	T_{eff} (K)	log g	β	$\dot{M}$ ($M_\odot$ yr^{-1})	v_{exp}(OH) (km s^{-1})	log $\varepsilon(Li)_{static}$	log $\varepsilon(Li)_{dyn}$	log $\varepsilon(Ca)_{static}$	log $\varepsilon(Ca)_{dyn}$
01085+3022*	3300	−0.5	0.2	1.0×10^{-7}	13	2.4	2.2	...	...
02095−2355	3300**	−0.5	0.8	1.0×10^{-9}	12†	1.6	1.6	6.3	6.3
05027−2158	2800	−0.5	0.4	1.0×10^{-7}	8	1.1	1.1	5.8	5.8
05098−6422	3000	−0.5	1.4	1.0×10^{-8}	6	≤ -1.0	≤ 0.0	6.1	6.1
05151+6312	3000	−0.5	1.0	1.0×10^{-8}	15	≤ 0.0	≤ 0.2	6.0	6.0
05559+3825	2900	−0.5	1.6	1.0×10^{-7}	12†	0.6	0.5	5.8	5.8
06300+6058	3000	−0.5	0.2	1.0×10^{-7}	12	0.7	0.8	≤ 5.8	≤ 5.8
07304−2032	2700	−0.5	0.4	1.0×10^{-7}	7	0.9	1.0	≤ 5.8	≤ 5.8
09429−2148	3300**	−0.5	1.6	1.0×10^{-8}	12	2.2	2.2	5.3	5.3
10261−5055	3000	−0.5	0.2	1.0×10^{-9}	4	≤ -1.0	≤ 0.0	5.8	5.8
11081−4203	3000	−0.5	1.6	5.0×10^{-8}	8†	1.3	1.1	5.8	5.8
14266−4211	2900	−0.5	0.2	5.0×10^{-8}	9	≤ 0.0	0.2	≤ 5.3	≤ 5.3
14337−6215*	3300	−0.5	0.2	5.0×10^{-8}	20	2.4[1]	2.4[1]	...	...
15193+3132	2800	−0.5	1.6	1.0×10^{-9}	3	≤ 0.0	≤ 0.0	≤ 5.8	≤ 5.8
15211−4254	3300**	−0.5	1.6	1.0×10^{-9}	11	2.3	2.3	5.8	5.8
15255+1944	2900	−0.5	0.2	5.0×10^{-7}	7	1.0	0.9	6.0	6.0
15576−1212	3000	−0.5	0.2	1.0×10^{-8}	10	1.1	1.2	5.7	5.7
16030−5156*	3000	−0.5	0.2	1.0×10^{-8}	10†	1.5	1.5	...	...
16037+4218	2900	−0.5	1.2	1.0×10^{-8}	4	≤ -1.0	≤ 0.0	6.3	6.3
16260+3454	3300**	−0.5	0.2	1.0×10^{-9}	12	2.7	2.6	5.4	5.4
17034−1024	3300**	−0.5	0.8	1.0×10^{-8}	8†	≤ 0.0	≤ 0.0	6.2	6.2
18413+1354	3300**	−0.5	1.2	1.0×10^{-8}	15	1.8	1.7	≤ 5.3	≤ 5.3
18429−1721	3000	−0.5	0.2	1.0×10^{-8}	7	1.2	1.1	5.8	5.8
19129+2803	3300**	−0.5	0.2	1.0×10^{-8}	11†	3.1[1]	3.1[1]	5.5	5.5
19361−1658	3000	−0.5	0.2	1.0×10^{-9}	8	1.9	2.0	5.8	5.8
20052+0554*	3300	−0.5	0.2	1.0×10^{-7}	16	2.6	2.3	...	...
20343−3020	3000	−0.5	1.2	1.0×10^{-9}	8	≤ -1.0	≤ 0.0	6.0	6.0
RU Cyg	3000	−0.5	1.6	1.0×10^{-7}	12†	2.0	1.7	6.2	6.2
SV Cas	3000	−0.5	1.6	1.0×10^{-7}	12†	3.5	3.3	6.3	6.3
R Cen[2]	3000	−0.5	1.6	1.0×10^{-7}	5†	4.3	4.0	...	...

† These stars only display a single peak in the 1612 MHz OH maser. Thus, in the abundance analysis, we adopted the average OH expansion velocities of other stars with similar variability periods.

* The S/N at Ca I 6463 Å is very low to derive any Ca abundance estimate.

** The best fitting T_{eff} in the Ca I 6463 Å spectral region is cooler (3000 K) than the one around the Li I 6708 Å line.

[1] The line is resolved in two components (circumstellar and photospheric) and the abundance obtained corresponds to the photospheric one.

[2] R Cen was not observed in the Ca I line region.

The NLTE radiative transfer calculations for the 6708 Å Li I line were performed using the MULTI code (Carlsson 1986, 1992) with the same Li atom model as in Osorio et al. (2011). This Li atom model includes quantum mechanical calculations of electron and hydrogen collisional excitation as well as charge exchange with hydrogen (see more details in Osorio et al. 2011). The calculations were performed in the same grid of MARCS models used in Osorio & Barklem (2016) and the models are hydrostatic. For this study we focused on the subgrid of atmospheric models with the typical massive AGB stellar parameters (see García-Hernández et al. 2007a, for more details); i.e. log $g = -0.5$, [Fe/H] = 0.0 and five different effective temperatures, T_{eff} = 2500, 2600, 2700, 3300, and 3400 K. For the three coolest models, the NLTE abundance corrections $\Delta(\log\varepsilon(\mathrm{Li}))_{NLTE-LTE}$ are $\gtrapprox +0.2$ dex, reaching +0.3 dex at logε(Li)=0.0. The warmer model atmospheres display smaller NLTE abundance corrections of $\Delta(\log\varepsilon(\mathrm{Li}))_{NLTE-LTE} \sim 0.0$ dex at logε(Li) $\sim +2.0$ and $\Delta(\log\varepsilon(\mathrm{Li}))_{NLTE-LTE}$ $\sim +0.1$ dex around logε(Li) ≥ 3.0 and logε(Li) ≤ 0.5. Our updated NLTE Li calculations thus confirm the Li-rich character of our massive O-rich AGB sample stars and that the adoption of LTE in Li-rich AGB stars is likely to result in an underestimation of the Li abundances (e.g. Kiselman & Plez 1995; Abia et al. 1999).

For the NLTE calculations of the 6463 Å Ca I line, the MULTI code was used with the same Ca atom model as in Osorio et al. (2019). This Ca atom model also includes updated data for electron and hydrogen collisional excitation and charge exchange with hydrogen. The calculations were performed in two atmospheric hydrostatic models with T_{eff}/log$g$/[Fe/H] = 3000/−0.5/0.0 and 3300/−0.5/0.0 for which we found positive NLTE abundance corrections of $\sim +0.06$ and +0.02 dex, respectively. In short, our NLTE Ca calculations show that the use of LTE in massive O-rich AGB stars would translate into a slight underestimation of the real Ca abundances (see Sect. 3.6.2).

3.6 Discussion

3.6.1 Lithium

Our Li results in massive Galactic AGB stars, including a circumstellar component in the analysis, do not reflect a dramatic change in the derived abundances, contrary to our previous findings of the Rb abundances in these stars (see Chapter 2). The Rb abundances obtained with pseudo-dynamical models are much lower (sometimes even by 1-2 dex) than the hydrostatic ones, being strongly affected by the presence of a circumstellar envelope. We have made several tests by changing the wind parameters (mass loss rate $\dot{M}$, parameter β

and the terminal velocity v_{exp}(OH)) in the models; for example, not fixing $\dot{M}$ and β or by assuming the wind model parameters from the best fits of the Rb I 7800 Å line (see Table 2.4) but the Li abundances remain very similar (within 0.1 dex). As we have mentioned before, for consistency, we have fixed $\dot{M}$ and β to those values obtained in Cgapter 2 from the Rb spectral fits (when available) because the synthetic spectra around 7800 Å are more sensitive to variations in the model wind parameters than the Li I 6708 Å spectral region. Our finding of the circumstellar effects being not so important for the Li I 6708Å line could be perceived as surprising because the atomic parameters (e.g. excitation potential) of the Li I 6708 Å and Rb I 7800 Å resonance lines are quite similar. The lower Li abundance as compared with Rb, and therefore lower Li I column-density in the circumstellar envelope, however, likely explains the small abundance differences obtained between the pseudo-dynamical and hydrostatic models. In addition, other factors such as the molecular blends in each wavelength range and the line depth formation could influence the different sensitivity to the circumstellar effects between Rb and Li. In particular, the line depth formation is extremely important because the velocity field could change the τ-scale of the lines (see Nowotny et al. 2010).

We have compared our new Li abundances with up-to-date solar metallicity massive AGB nucleosynthesis models with very different prescriptions for mass loss and convection: (i) ATON models (Ventura et al. 2018) with the Bloecker (1995) recipe for mass loss and the full spectrum of turbulence convective mixing (FST; e.g. Mazzitelli et al. 1999); (ii) Monash models (Karakas & Lugaro 2016) with the Vassiliadis & Wood (1993) mass-loss prescription and the mixing length theory of convection (MLT; Böhm-Vitense 1958); (iii) FRUITY[3] models (Cristallo et al. 2015) with a pulsationally-driven mass-loss rate (see Straniero et al. 2006) and the MLT of convection but under the formulae from Straniero et al. (2006); and (iv) NUGrid/MESA models (Ritter et al. 2018) with the mass-loss formula from Bloecker (1995) and assuming convective boundary mixing (CBM; e.g. Ritter et al. 2018).

The evolution of Li in massive HBB-AGB stars is strongly affected by several stellar parameters such as the progenitor mass, metallicity, mass loss, and convection model (see e.g. Mazzitelli et al. 1999; van Raai et al. 2012). During the AGB phase, the mass loss and treatment of the convection are the most important factors determining the duration of HBB and the variation of the surface chemistry during the AGB phase. For example, i) the massive AGB nucleosynthesis ATON models show strong Li abundance oscillations (by or-

[3]FUll-Network Repository of Updated Isotopic Tables and Yields: http://fruity.oa-abruzzo.inaf.it/.

ders of magnitude) on timescales as short as $\sim 10^4$ years (see e.g. Mazzitelli et al. 1999) and there may be negligible Li in the envelope for a significant (at least 20%) period of time; and ii) the Li minima and the duration of the Li-rich phase in the Monash models are less deep and longer, respectively, than in the ATON models (see García-Hernández et al. 2013, for more details). This complex theoretical evolution of the Li abundance implies that the Li abundance distribution derived from the spectroscopic observations (e.g. the exact progenitor mass and evolutionary status are not known) can only be analysed in a statistical way (García-Hernández et al. 2007a).

Regarding the peak surface Li abundances during the AGB, the ATON models at Z = 0.014 predict that it goes from logε(Li) = 3.8 dex for M = 3.5 $M_\odot$ to 4.3 dex for M = 6.0 and 7.5 $M_\odot$, while in the Monash models it changes from logε(Li) = 3.8 dex for M = 4.25 $M_\odot$ to logε(Li) = 4.4 dex for M = 8 $M_\odot$ at Z = 0.014. In the NuGrid/MESA models, Li production at Z = 0.02 is only predicted for M = 6 and 7 $M_\odot$ with a peak surface Li abundance of 2.9 and 3.7 dex, respectively. However, the FRUITY models do not predict production of Li at all, which is at odds with the Li over-abundances observed in massive AGB stars in the Galaxy (e.g. García-Hernández et al. 2007a, 2013), the Magellanic Clouds (e.g. Plez et al. 1993; Smith et al. 1995; García-Hernández et al. 2009a) and the Li-detected O-rich AGB star in the dwarf galaxy IC 1613 (e.g. Menzies et al. 2015).

The pseudo-dynamic Li abundances obtained from our spectra are between $\sim$0.0 and 4.0 dex; with eight non Li-rich (logε(Li) $<$ 0.5 dex), twenty Li-rich (0.5 $\leq$ logε(Li) $\leq$ 3.2 dex) and two super Li-rich (logε(Li) $>$ 3.2 dex) stars. Their great similarity with the hydrostatic Li abundances (and the relatively small positive NLTE corrections, see Section 3.5) supports the conclusions reached by García-Hernández et al. (2007a, 2013) are unchanged. In short, the Li-rich and super Li-rich character of the massive AGB stars in our sample confirm that they experience strong HBB (García-Hernández et al. 2007a, 2013). This is in good agreement with the predictions from AGB nucleosynthesis models like the ATON, Monash and NuGrid/MESA, but in strong contrast with the FRUITY AGB models, which do not predict strong HBB and Li production in solar metallicity massive AGB stars.

3.6.2 Calcium

This is the first work in which the Ca abundances have been obtained for a sample of massive AGB stars. Figure 3.3 shows that the 6463 Å Ca I line is not sensitive to changes in the stellar (T_{eff}) and wind ($\dot{M}$, β and v_{exp}(OH)) parameters. Thus, we adopted the wind parameters from the Rb fits (when

possible) or the Li fits, which are more sensitive to variations of the wind parameters. The hydrostatic and pseudo-dynamic abundances of Ca obtained from our spectra are identical; so the Ca abundances are not affected at all by the presence of a circumstellar envelope. The Ca abundances obtained are in the range log $\varepsilon(Ca)$ = 5.3 - 6.3 dex. The theoretical AGB nucleosynthesis models predict an important production of some Ca isotopes like the radioactive ^{41}Ca but no significant change in the total Ca abundance (see Section 3.1). We note that here we consider log $\varepsilon(Ca)$ = 6.31 dex as the solar abundance in the photosphere (Grevesse et al. 2007). While ATON models (Ventura et al. 2018) do not include Ca, the Monash models predict Ca abundances in the range log $\varepsilon(Ca)$ = 6.31 - 6.35 dex for solar metallicity; in other words, an at-most 12% increase relative to the initial value used in these models of 6.29 dex. In the same way, the FRUITY models predict solar Ca abundances for Z = 0.014. In the NuGrid/MESA models, Ca at Z = 0.01 is predicted to vary from log $\varepsilon(Ca)$ = 6.11 to 6.18 dex in the range of M = 3 -7 solar masses, while for Z = 0.02 the Ca abundances are between 6.44 and 6.48 dex.

In Figure 3.6 we show the evolution of Li, Ca, and the radioactive isotope ^{41}Ca as a function of time for the 6 $M_{\odot}$ model of solar metallicity from Karakas & Lugaro (2016). This figure shows that the ^{41}Ca abundance increases as a consequence of nucleosynthesis and mixing during the TP-AGB phase although the first increase of the ^{41}Ca occurred during the second dredge-up, after core helium burning. We can also see that the total elemental Ca abundance is, however, unchanged. The 6 $M_{\odot}$ model has TDU and HBB as described in Karakas & Lugaro (2016), remains oxygen rich as a consequence of HBB, and as shown by Figure 3.6 the model becomes Li-rich, where the log ε(Li) exceeds three for $\sim$ 80,000 years.

We find that most (67%) sample stars display Ca abundance values $\sim$ 0.5 - 0.6 dex lower than the adopted Ca solar abundance of log $\varepsilon(Ca)$ = 6.31 dex. In spite of the fact that we cannot completely discard that some of our sample stars could be indeed slightly metal poor[4], their Ca abundances can be considered as nearly solar when taking into account our estimated Ca abundance errors ($\sim$ 0.5 dex) and the possible NLTE effects (see Section 3.5). This is consistent with the predictions from the available *s*-process nucleosynthesis models for solar metallicity massive AGB stars, as mentioned above.

However, a minority (five) of the sample stars seem to show a significant Ca depletion (-0.8 to -1.0 dex). We explored if the derived Ca abundances are correlated with the Li content, the wind parameters ($\dot{M}$, β and v_{exp}(OH))

[4]We note, however, that most sample stars are expected to be of solar metallicity (see a detailed discussion on this in García-Hernández et al. 2007a).

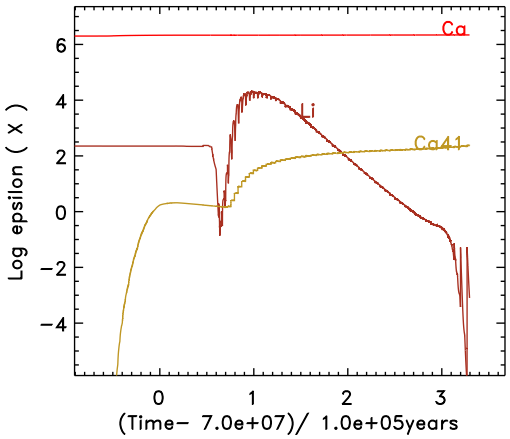

Figure 3.6: Evolution of Li, Ca, and ^{41}Ca versus time for the 6 $M_{\odot}$ model of solar metallicity from Karakas & Lugaro (2016).

or other observational information such as variability periods, near-IR colours and IR excess but our search proved to be negative with the possible exception of the near-IR colours and the IR excess (see below). We have identified three possibilities (i.e. missed opacities in the stellar atmosphere models, Ca depletion into dust and line weakening phenomena) in order to understand their apparent (and unexpected) Ca depletion:

Firstly, the low Ca abundances in our sample stars could be due to missed opacities in the stellar atmosphere models. Although the Ca spectral region (mainly dominated by the TiO molecule) is generally well modelled by us, García-Hernández et al. (2007a, 2009a) report the presence of strong and yet unidentified molecular bands in several spectral regions in the optical spectra of massive Galactic and extragalactic O-rich AGB stars, which suggest the presence of other opacity contributors not yet considered in the model atmospheres and in the construction of synthetic optical spectra for O-rich AGB stars.

Secondly, although the condensation of inorganic dust grains in the winds of evolved stars is still poorly understood, the observed Ca under-abundances may be also due to the fact that Ca in our sample of stars could be depleted into dust (see e.g. Lodders & Fegley 1999, for a review). Figure 3.7 plots the Ca pseudo-dynamical abundaces against the 2MASS J-K colours and the infrared excesses R = F(12μm)/F(2.2μm)[5] (with fluxes at 2.2 and 12 μm from 2MASS and IRAS, respectively) in our sample stars. Curiously, the five stars that have significant Ca depletion are the redder ones (they display, on average, higher J-K colours) and most of them display a significant infrared excess, suggesting that they could be among the more evolved and/or dusty stars in our sample. However, the number of stars is still low and Galactic massive AGB stars are known to display a large photometric variability in the near-IR and mid-IR ranges (see e.g. García-Hernández et al. 2007b). Dell'Agli et al. (2014) studied the alumina dust (the amorphous state of Al_2O_3) production in O-rich circumstellar shells, which is expected to be fairly abundant in the winds of the more massive and O-rich AGB stars. By coupling AGB stellar nucleosynthesis and dust formation, the predicted production of alumina dust implies an important decrease (see below) in the abundance of gaseous Al in the AGB wind. The high fraction of gaseous Al condensed in Al_2O_3 (especially in their more massive AGB models) implies that the gaseous Al is expected to be under-abundant in the more massive HBB-AGB stars; something that is in good agreement with the only estimate of the Al content in massive HBB-AGB stars to date[6]; in other words, the Al content measured in a confirmed massive

[5]The infrared excess R probes the presence of circumstellar material emitting at 12 μm with respect to the stellar continuum at 2.2 μm (see e.g. Jorissen et al. 1993).

[6]McSaveney et al. (2007) measured $\log \varepsilon$(Al) = 5.5 dex in the truly massive HBB-AGB

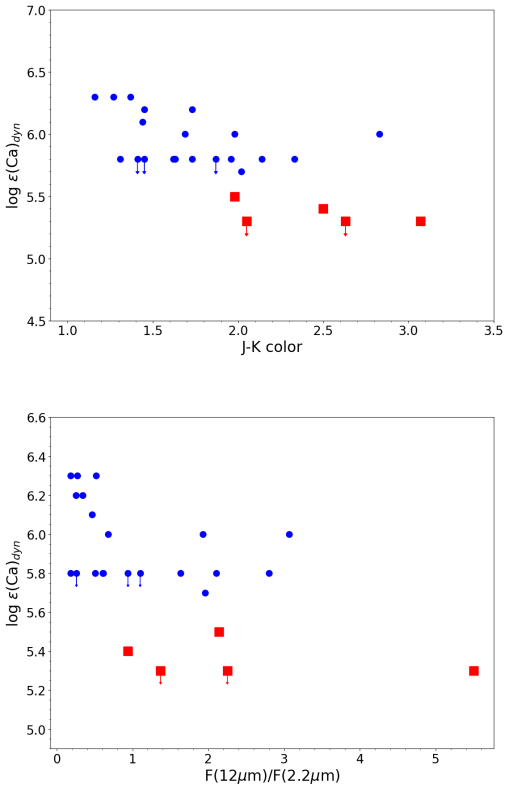

Figure 3.7: Ca abundances derived with pseudo-dynamical models against the J-K colours (top panel) and infrared excesses R = F(12μm)/F(2.2μm) (bottom panel). The five stars with the largest Ca depletion values are shown by red squares and upper limits are indicated by vertical arrows.

HBB-AGB in the Large Magellanic Cloud (see Dell'Agli et al. 2014, for more details). Thus, similarly to the Al case, the gaseous Ca in massive Galactic O-rich AGB stars could be depleted into dust. For example, Tielens (1990) proposed a dust condensation sequence in O-rich circumstellar regions, in which the formation of calcium-rich silicates such as augite ($Ca_2Al_2SiO_7$), diopside ($CaMgSi_2O_6$), and anothite ($CaAl_2Si_2O_6$) would be expected (see also Lodders & Fegley 1999, and references therein). However, Speck et al. (2000) suggest that the dust evolutionary path is different for the AGB and red supergiant (RSG) stars; although both condensation sequences eventually would lead to similar dust types. Basically, the main difference between the RSG and AGB dust condensation sequences is that the RSG stars experience an evolutionary phase in which aluminium- and calcium-rich silicates condensation takes place, while this evolutionary phase is apparently not seen in the AGB stars. Speck et al. (2000) classified the spectra of a sample of AGB and RSG stars into several groups according to the observed appearance of the amorphous silicates infrared (IR) features around 10 μm. They found that the RSG IR spectra are better reproduced when calcium-rich silicates are considered, while the AGB stars are well reproduced with amorphous silicates only. Unfortunately, we have only three stars (RU Cyg, IRAS 07304−2032, and IRAS 15193+3139) in common with Speck et al. (2000) and they are not among the most Ca-poor stars in our sample. Speck et al. (2000) classified their spectra as silicate A (RU Cyg) and silicate B (IRAS 07304−2032 and IRAS 15193+3139) AGB types; all of them with no clear signs of calcium-rich silicates. Additional N-band IR spectroscopic observations of confirmed Galactic AGB O-rich stars (especially for those stars with significant Ca depletion) would be desirable in order to clarify if their 10 μm amorphous silicates dust features could be better fitted by the inclusion of Ca-rich silicates. Ca-rich stardust grains from AGB stars have been recovered from meteorites, also belonging to the Group II population that probably originated from HBB-AGB stars (Lugaro et al. 2017). Both hibonite grains (e.g. Nittler et al. 2008), as well as Ca-rich silicates (e.g. Nguyen & Zinner 2004; Vollmer et al. 2009) have been reported.

Third and finally, line weakening phenomena could be another possibility to explain the lack of Ca in these sample stars. Humphreys (1974) studied some high-luminosity M-type supergiants that show veiling of the absorption metallic lines; the veiling effect was found to be most pronounced in the near-IR than in the blue spectral regions. Humphreys (1974) proposed that the

star HV 2576 in the LMC (Z = -0.3 dex), while the Al solar abundance is 6.4 dex (Grevesse et al. 2007). The amount of gaseous Al depleted into dust is 0.6 dex, in good agreement with the Dell'Agli et al. (2014) AGB models that include dust formation.

peculiar energy distributions of these stars and the veiling of the absorption lines may be explained by a combination of free-bound emission ($\lambda < 1.6$ μm) and free-free emission ($\lambda > 1.6$ μm) from electron-neutral H interactions arising in the extended atmosphere around the star plus the surrounding circumstellar shell of dust grains. Such line weakening phenomenon, as observed in these peculiar M-supergiants, could be also present in similar M-type long-period variables (more than 260 days) dusty stars such as our sample stars. We have looked for additional absorption metallic lines in our Li and Ca spectral regions (e.g. the 6469 Å Fe I and 6484 Å Ni I lines) in order to check if line weakening phenomena are affecting other metallic lines. Unfortunately, our optical spectra are severely dominated by the TiO molecule and no metallic lines are detected. We thus cannot confirm or reject the possibility that the lack of Ca in our minority stars is because of possible line weakening phenomena affecting the optical spectra of massive Galactic O-rich AGB stars.

4

CNO abundances and isotopic ratios in massive AGB stars

Based on

V. Pérez-Mesa et al. 2020, A&A (to be submitted)

ABSTRACT - We have determined, for the first time by using spectral synthesis, the CNO abundances and isotopic ratios in a small sample of massive Galactic AGB stars at the beginning of the TP phase. The abundances and isotopic ratios, as derived by using hydrostatic model atmospheres, are consistent with the nucleosynthesis theoretical predictions for very massive (∼7-8 $M_{\odot}$) AGB stars that experience HBB at solar metallicity. In addition, we have explored the circumstellar effects (considering pseudo-dynamical model atmospheres) in the elemental and isotopic CNO abundances of massive AGB stars, resulting that such effects are negligible. Moreover, we have compared our O isotopic ratios with the measurements in presolar grains, and they are compatible (clearly for two sample stars) with Group II grains. This result, however, is not conclusive and we cannot unambiguously confirm that massive AGB stars are the origin of the Group II grains. Finally, our results for two sample stars indicate ∼8 $M_{\odot}$ HBB progenitors that have not experienced any TP. Such stars could represent very good candidates for truly super-AGB stars, but more precise CNO isotopic ratios and further super-AGB nucleosynthesis calculations would be needed to confirm this possibility.

4.1 Introduction

The AGB (Herwig 2005; Karakas & Lattanzio 2014) is occupied by low- and intermediate-mass (between 0.8 and 8 $M_{\odot}$) stars in the last nuclear-burning phase. At the end of the AGB phase, these stars develop TPs and suffer extreme mass loss. The AGB stars are thus one of the main contributors to the enrichment of the ISM of light elements (e.g. Li, C, N, F) and heavy (slow neutron capture, *s*-process; e.g. Rb, Zr, Y, Sr) elements and this evolutionary stellar phase is thus crucial to understand the chemical evolution of galaxies, because the expelled material will lead to new generations of stars and planets. AGB stars are also the site of origin of the vast majority of meteoritic stardust grains (e.g. Hoppe & Ott 1997; Nittler et al. 1997; Lugaro et al. 2017).

As it was commented in Chapter 1, there are two possible reactions releasing neutrons for the *s*-process elements: $^{13}C(\alpha, n)^{16}O$ and $^{22}Ne(\alpha, n)^{25}Mg$. In the low-mass AGB stars ($M < 4$ $M_{\odot}$), the ^{13}C reaction is the dominant one, while in the more massive AGB stars ($M > 4$–5 $M_{\odot}$), neutrons are mainly released by the ^{22}Ne reaction, resulting in a higher neutron density (up to 10^{13} n/cm^3) and temperature environment than in lower-mass AGB stars (e.g. García-Hernández et al. 2006). Thus, the more massive AGB stars enrich the ISM with elements and radioisotopes very different to those from low-mass AGB stars as a consequence of the HBB activation and the *s*-process being driven by the ^{22}Ne neutron source. According to our current understanding, the HBB process in massive AGB stars overproduces ^{13}C, ^{7}Li, ^{14}N, ^{17}O and the short-lived radioisotopes ^{26}Al and ^{41}Ca, while the activation of the ^{22}Ne neutron source leads to overabundances of the radioisotopes ^{87}Rb and ^{60}Fe (e.g. Trigo-Rodríguez et al. 2009). In fact, it has been shown that the contamination produced by a nearby massive AGB or super-AGB star during the formation of the Early Solar System could explain the abundances of these radioisotopes (e.g. ^{26}Al, ^{41}Ca and ^{60}Fe) as measured in primitive meteorites (e.g. Trigo-Rodríguez et al. 2009; Doherty et al. 2012). In addition, the isotopic ratios $^{17}O/^{16}O$, $^{18}O/^{16}O$, $^{12}C/^{13}C$, etc. are usually used as indicators of the parent stars of the presolar grains found in meteorites (Nittler et al. 1997; Zinner et al. 2005). Most of the analyzed presolar grains show ^{17}O excesses and ^{18}O deficits (in comparison with the solar values) and were historically associated with Red Giant stars and low-mass AGB stars in the literature. Recently, Lugaro et al. (2017) showed that the increased proton-capture rate of ^{17}O (as reported by the Laboratory for Underground Nuclear Astrophysics, LUNA) leads to theoretically predicted $^{17}O/^{16}O$ isotopic ratios that match those observed in the Group II grains, and also to temperatures that could be achieved at the base of the convective envelope during the late evolution of intermediate-mass

stars in the 4-8 $M_{\odot}$ range. This result reveals these stars as the possible site of the origin of the Group II grains. However, all these previous works are based in theoretical predictions of AGB nucleosynthesis models that have not been confronted with observations of truly massive AGB stars in our Galaxy.

There are not many previous works about the elemental and isotopic CNO abundances in massive AGB stars. McSaveney et al. (2007) aimed to derive the CNO abundances in a small sample (7) of massive AGB stars in the Magellanic Clouds (MC), finding very large N enhancements (and C deficiencies) in two stars and providing the observational confirmation that HBB can produce significant amounts of primary N in low-metallicity massive AGB stars. However, McSaveney et al. (2007) could not derive the abundances for the remaining five stars in their sample because they were too cool and extreme to model their spectra. These stars were the most evolved and extreme dusty stars in their sample and showed complex spectra with no clear continuum remaining or showing strong shocks in their atmospheres. Justtanont et al. (2013) observed with the far-IR Herschel Space Observatory a small sample (5) of extreme Galactic OH/IR stars (massive AGB stars candidates with no optical counterpart) and estimated the $^{12}C/^{13}C$ and $^{18}O/^{16}O$ isotopic ratios from the CO and H_2O isotopologues. In all these heavily reddened AGB stars, the average $\langle ^{12}C/^{13}C\rangle = 15$ and $\langle ^{18}O/^{17}O\rangle \simeq 0.1$ were explained by the HBB process, which is activated in stars with stellar masses larger than 5 $M_{\odot}$ at solar metallicity, and that reduces the $^{12}C/^{13}C$ ratio and preferentially destroys ^{18}O relative to ^{16}O (see Justtanont et al. 2013, for more details). Hinkle et al. (2016) reported the C and O isotopic ratios from near-IR (R $\sim$ 57,000 at 2.5 μm and R $\sim$ 96,000 at 1.5 μm) Fourier Transform Spectrometer (FTS) spectra and following the curve of growth (CoG) analysis (see Section 4.4 for more details), in a sample of 46 Mira and SRa-type variable AGB stars. The stars in their sample showed $^{16}O/^{17}O$ ratios similar to those of Group I presolar grains and theoretical predictions of 1.2-2 $M_{\odot}$ stars, but with $^{16}O/^{18}O$ ratios lower than those of Group I grains. No stars in their sample showed evidence for HBB, but for one star, SV Cas, they estimated an O isotopic composition similar to that of Group II grains. More recently Abia et al. (2017a) presented preliminary results of CNO isotopic ratios in two highly evolved intermediate-mass ($M \geq 4$ $M_{\odot}$) Galactic AGB stars from high resolution near-IR spectra. They had problems modelling the spectra of such extreme stars and their derived preliminary C and O ratios were not consistent with the HBB theoretical predictions.

In this chapter, we report for the first time by using spectral synthesis, the CNO isotopic abundances in massive Galactic AGB stars at the beginning of the TP phase. We deliberately looked for Li-rich (but with no *s*-elements enhancements) massive AGB stars at the beginning of the TP phase because

they display simpler spectra (less affected by circumstellar dust and should be more easy to model), already showing the strong effects of the HBB (García-Hernández et al. 2013). In addition, we compare the elemental and isotopic CNO abundances with theoretical nucleosynthesis models, and also with the corresponding isotopic ratios measured in presolar grains.

4.2 Sample, near-IR spectroscopic observations and data reduction

4.2.1 Sample selection

We acquired between April and October 2007 optical spectra of a large sample (about 100 sources) of relatively blue Galactic AGB stars displaying different maser emission (from SiO, H_2O or OH) with the Cross-Dispersed Echelle Spectrometer (CS2) attached to the Coude f/32.5 focus of the 2.7m Harlan J. Smith telescope, at McDonald Observatory. Most of these optical spectra, obtained by García-Hernández and Lambert, have not been published before; only two stars, SV Cas and RU Cyg, were published in García-Hernández et al. (2013). In order to select our sample stars at the beginning of the TP phase, we looked for Li-rich and no *s*-elements enriched stars (García-Hernández et al. 2013) by using the 6708 Å Li I, 7800 Å Rb I and 6474 Å ZrO spectral regions. After a quick look of these ∼100 optical spectra, we selected IRAS 15152+3632, IRAS 18072+3100 and IRAS 18141+0340 because these stars display very weak Rb I lines and ZrO bandheads, but strong Li I resonance lines, which are indicative of them being good candidates for massive AGB stars at the beginning of the TP phase (see García-Hernández et al. 2013). Moreover, we added also two stars, SV Cas and RU Cyg, which were previously known to be not Rb-rich but super Li-rich massive AGB stars at the beginning of the TP phase (García-Hernández et al. 2013).

As we have mentioned before, we have selected this small sample of five massive Galactic AGB stars at the beginning of the TP phase in order to know the real effects of the HBB by measuring the CNO elemental abundances and isotopic ratios (e.g. $^{12}C/^{13}C$, $^{16}O/^{17}O$, $^{16}O/^{18}O$ and $^{14}N/^{15}N$) in the near-IR spectral range. We note also that we have selected about 25 additional AGB stars from García-Hernández et al. (2006, 2007a) covering different observational properties (IR color, level of obscuration, etc.) and chemical abundances of Li and *s*-process elements (Rb and Zr). However, those additional stars cover different progenitor masses and/or AGB evolutionary stages and will be studied elsewhere.

4.2.2 Near-IR TNG/GIANO observations and data reduction

We used the high resolution spectrogragh GIANO, mounted at the Nasmyth A focus of the 3.6m Telescopio Nazionale Galileo (TNG), at the Observatorio del Roque de Los Muchachos (ORM), La Palma. GIANO provides cross-dispersed echelle spectroscopy at a resolution of ∼50,000 over the 0.95-2.45 μm spectral range in a single exposure. It is fiber-fed with two fibers of 1 arcsec angular diameter at a fixed angular distance of 3 arcsec on sky. GIANO has only one observing mode and can acquire spectra either of astrophysical objects and sky simultaneously (on fiber A and B, AB cycles), or of calibration lamps (halogen for flat-field and U-Ne for wavelength calibration) and dark frames. The observations were carried out during three nights on July 2017 (10-12). The five massive AGB stars at the beginning of the TP phase were observed during July 10 (with an average seeing of ∼1"). Our stars are strongly variable in the near-IR (up to 1-2 magnitudes in the H and K bands) and our goal was to obtain a high signal-to-noise (S/N > 100) in the pseudo-continuum. For this reason, our strategy was to obtain a first short test exposure (AB cycle) in order to estimate, at real time, the individual exposure time to reach the maximum S/N of 50 for a single exposure (see the GIANO cookbook for proposers; version 2015A) but still permitting a good sky background subtraction as well as the number of AB cycles per target. For example, for a S/N of 50 from the individual test exposure ($S/N_{individual}$) a total of 4 exposures (N) are needed to reach the desired S/N of 100 ($S/N_{final} = S/N_{individual} \times \sqrt{N}$). In addition, we also obtained very high S/N spectra of nearby and hot (fast-rotating) stars for telluric correction purposes. The final S/N ratios achieved in the five massive AGB stars at the beginning of the TP phase varied between 130 and 200 per pixel (see Table 4.1).

The near-IR data have been reduced by using the data reduction pipeline of GIANO. In summary, the data reduction pipeline combines together the dark frames with the same integration time and subtracts the corresponding dark frame to the flat-field frames and single science or calibration frame. Then, the pipeline performs bad-pixel correction of all frames (flat-field, reference lamp, science and calibration) and average together the flat-field frames. Later, it finds the traces after the scattered light correction, fits them and constructs a normalised 2D flat-field frame from the average flat-field frame that is then used to divide all corrected reference lamp, science and calibration frames. Next, the data reduction pipeline subtracts the corrected frame B in every AB cycle set from the corresponding corrected frame A. If there are more AB cycles on the same target, the subtracted frames are averaged together. Afterwards, the pipeline sorts all the traces retrieved to reflect the correct spectral order

Table 4.1: Atmosphere parameters and Li abundances (as derived using hydrostatic models) and other selected observational information.

IRAS name	T_{eff} (K)	log$g$	Period[a] (days)	log$\varepsilon(Li)_{static}$	S/N at 1550 nm
15152+3632	2900	−0.5	276	1.2	156
18072+3100	3000	−0.5	165	1.5	202
18141+0340	3000	−0.5	150	1.4	191
SV Cas	3000	−0.5	262	3.5	130
RU Cyg	3000	−0.5	233	2.0	186

[a]Reference for the pulsation periods: General Catalogue of Variable Stars (GCVS), Samus' et al. (2017).

scheme, fixes the trace definition and the sky windows to be used for background subtraction. Finally, the data pipeline extracts and wavelength-calibrates the 1D spectra science frames.

We finally had to do by hand some additional steps in order to obtain our final reduced spectra. First, we combined with the IRAF[1] task *scombine* the spectra of the massive AGB and telluric stars (in those cases observed more than once) and cut them into the spectral sections in which we were interested by using *scopy*. Then, with the task *continuum*, we normalized the spectra to the pseudo-continuum envelope increasing the order of the fitting function. Finally, we compared the spectra of the massive AGB and telluric stars and shifted the spectra of the telluric ones until both match well and we used the task *telluric* in order to correct the telluric features in the spectra of the AGB stars (see Figure 4.1).

4.3 Synthetic spectra

In Chapters 2 and 3, we used the v12.2 version of the spectral synthesis code *Turbospectrum* (Alvarez & Plez 1998; Plez 2012) in order to study how the abundances of Rb, Zr, Li and Ca in massive AGB stars were affected by extended atmospheres. In the determination of the CNO elemental abundances and isotopic ratios, when using hydrostatic model atmospheres, we have used

[1]The Image Reduction and Analysis Faciclity sofware package (IRAF) is distributed by the National Optical Astronomy Observatories, which is operated by the Association of Universities for Research in Astronomy, Inc., under cooperative agreement with the National Science Foundation.

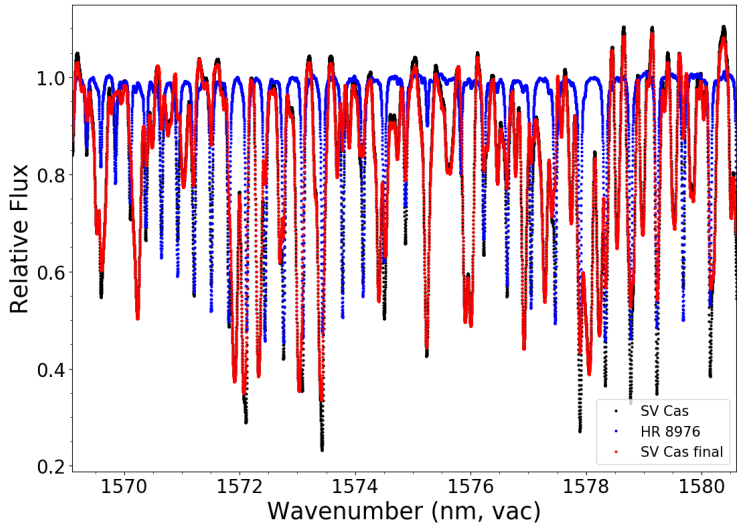

Figure 4.1: Illustrative example of the correction of telluric features at ∼1575 nm in the spectrum of the sample star SV Cas. The black dots indicate the observed spectrum of SV Cas, the blue dots mark the observed spectrum of the telluric star HR 8976 and the red dots indicate the final SV Cas spectrum, which is corrected of telluric features.

the more recent v15.1 version of *Turbospectrum*, while for the pseudo-dynamic case, in which we consider the presence of a circumstellar gas envelope with a radial wind, we have used again the v12.2 version of *Turbospectrum*. However, there are no differences between the v12.2 and v15.1 versions of *Turbospectrum*, only improvements in the calculation time. We have constructed the hydrostatic synthetic spectra assuming the solar abundances from Grevesse et al. (2007) and atmosphere parameters (e.g. T_{eff}, log g, [Fe/H], macroturbulence) from García-Hernández et al. (2013). For those stars not observed before (IRAS 15152+3632, IRAS 18072+3100 and IRAS 18141+0340), we have determined the T_{eff} and Li abundances from the spectral region around the 6708 Å Li I resonance line (see Table 4.1). By adopting the atmosphere parameters from García-Hernández et al. (2013), we generated synthetic spectra for each star in which we have fixed some parameters: stellar mass M = 2 $M_{\odot}$[2], gravity log g = -0.5, microturbulent velocity ξ = 3 km/s and metallicity [Fe/H] = 0.0 dex (see García-Hernández et al. 2007a, for more details).

We have constructed the synthetic spectra considering up-to-date atomic and molecular line lists of the most important contributors in the 1.5 - 2.4 μm spectral range: C_2 (Yurchenko et al. 2018), CN (Sneden et al. 2014), CO (Gordon et al. 2017), OH (Brooke et al. 2016), H_2O (Barber et al. 2006) and HF (Jönsson et al. 2014). In addition, we have synthesized individual spectra of the atoms, molecules and isomers (i.e. $^{12}C^{16}O$, $^{12}C^{17}O$, $^{12}C^{18}O$, $^{13}C^{16}O$, $^{12}C^{14}N$, $^{12}C^{15}N$, etc.) separately in order to select the best molecular lines to obtain the CNO elemental abundances and isotopic ratios. In particular, we were initially interested in various spectral regions around 1.554 μm (V-R OH lines), 1.650 μm ($^{12}C^{16}O$ and $^{13}C^{16}O$), 2.253 μm (CN Red System lines), 2.336 μm (2-0 $^{12}C^{17}O$) and 2.366 μm (2-0 $^{12}C^{18}O$) (see e.g. McSaveney et al. 2007; García-Hernández et al. 2009b; Hinkle et al. 2016; Souto et al. 2016; Abia et al. 2017a). Unfortunately, the 2.366 μm spectral region is in a gap in our observed echelle spectra.

The identification of spectral lines is a very difficult task in massive O-rich AGB stars because of the much higher density of CO, OH and CN molecular lines (see e.g. Figure 4.2) as compared to other hotter and/or simpler stars. For example, García-Hernández et al. (2009b) used the wavelength intervals 2.246-2.256, 2.326-2.346, 2.326-2.336 and 2.349-2.358 μm in order to obtain the $^{14}N/^{15}N$, $^{12}C/^{13}C$, $^{16}O/^{18}O$ and $^{16}O/^{17}O$ ratios, respectively, in hydrogen-deficient carbon (HdC) and R Coronae Borealis (RCB) stars. McSaveney et al.

[2]In all cases the stellar mass is 2 $M_{\odot}$ because between 1 and 10 $M_{\odot}$ model atmospheres the temperature and pressure structure are practically identical and the output synthetic spectra are not sensitive to the mass of the star (see Fig. 1 in Plez 1990).

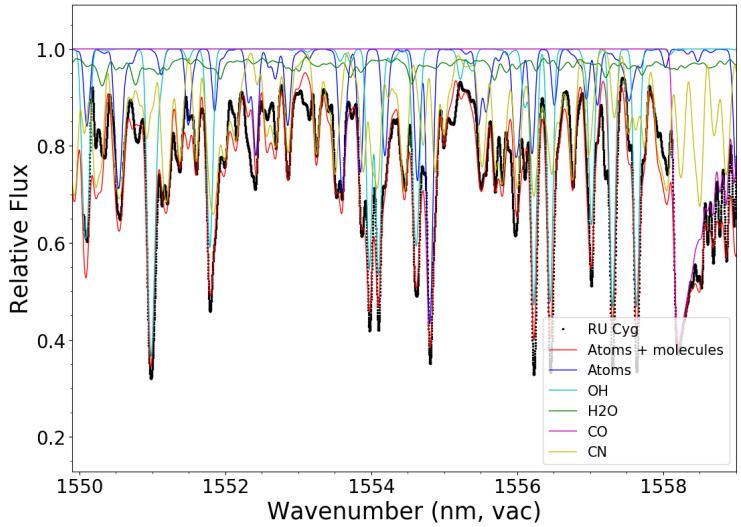

Figure 4.2: Observed spectrum of RU Cyg (black dots) centered at ∼1554 nm and the best hydrostatic fit (red line). The parameters of the best fit are indicated in Table 4.2. The contribution of the atoms (blue line), OH (cyan line), H_2O (green line), CO (magenta line) and CN (yellow line) to the total synthetic spectrum are also represented.

(2007), in intermediate-mass AGB stars in the MC, used a piece of the spectrum centred near 1.554 μm to determine the O and N elemental abundances and other region around 2.340 μm to measure the C abundance. Abia et al. (2017a), in intermediate-mass AGB stars in the Milky Way, refers to the McSaveney et al. (2007) regions around 1.554 and 2.340 μm for the determination of the CNO absolute abundances, but they did not report their estimated CNO values. Regarding the spectral regions used in Abia et al. (2017a) to derive the CNO isotopic ratios, the $^{16}O/^{17}O$ ratios were derived around 2.3 μm, while the N isotopic ratio was only measured in one carbon AGB star from an independent spectrum in the 8000 Å region. Unfortunately, Abia et al. (2017a) did not specify the spectral regions used to obtain the $^{12}C/^{13}C$ and $^{16}O/^{18}O$ isotopic ratios listed in their preliminary results. In C-rich AGB stars, Abia et al. (2017b) derived the C and O isotopic ratios from the intervals 2.329-2.340 and 2.349-2.369 μm, while the $^{14}N/^{15}N$ ratio was obtained at ∼8000 Å. Besides, Souto et al. (2016) measured the abundances of the dominant isotopes ^{12}C, ^{16}O and ^{14}N from sets of molecular lines of $^{12}C^{16}O$, ^{16}OH and $^{12}C^{14}N$, respectively, from NGC 2420 red giant H-band (1.5-1.7 μm) spectra. These spectral regions are the same used in Smith et al. (2013) for the analysis of red giant stellar spectra in the H-band. Finally, Hinkle et al. (2016) recently reported the C and O isotopic ratios, by CoG analysis, from the 2.462-2.498 μm and 1.753-1.794 μm CO regions in a sample of Mira and SRa-type variable AGB stars. However, most of these molecular lines are not clearly detected in our much cooler and O-rich massive AGB stars (e.g. due to the different T_{eff}, metallicity, evolutionary stage, etc.).

After a careful analysis of the spectral absorption lines (atoms, molecules and their isomers) across the entire wavelength range and their sensitivity to changes in the elemental abundaces of CNO and isotopic ratios, we have selected the following molecular features/lines: CO 1558.20 nm bandhead for C abundance, CN 1556.75 nm and 1558.50 nm for N abundance, and OH 1550.98 nm and 1563.14 nm for O abundance (see Figures 4.3 and 4.4). Then, we use the line at 1674.60 nm to obtain the $^{12}C/^{13}C$ ratio, which is the most sensitive line to changes in the isotopic ratio, and it is formed by $^{13}C^{16}O$ blended with $^{12}C^{14}N$ (see 4.5). Regarding the $^{16}O/^{17}O$ and $^{16}O/^{18}O$ ratios, the lines most sentive to changes in these isotopic ratios are $^{12}C^{17}O$ 2340.84 nm and $^{12}C^{18}O$ 2380.57 nm, respectively (see Figure 4.6). However, the fits to the observed spectra around 2380 nm are slightly worse than in the other spectral regions, so we have been conservative and the values that we have derived for the $^{16}O/^{18}O$ ratios are lower limits. The $^{14}N/^{15}N$ ratio is even more difficult to estimate because there are no clean lines with the only contribution of ^{15}N,

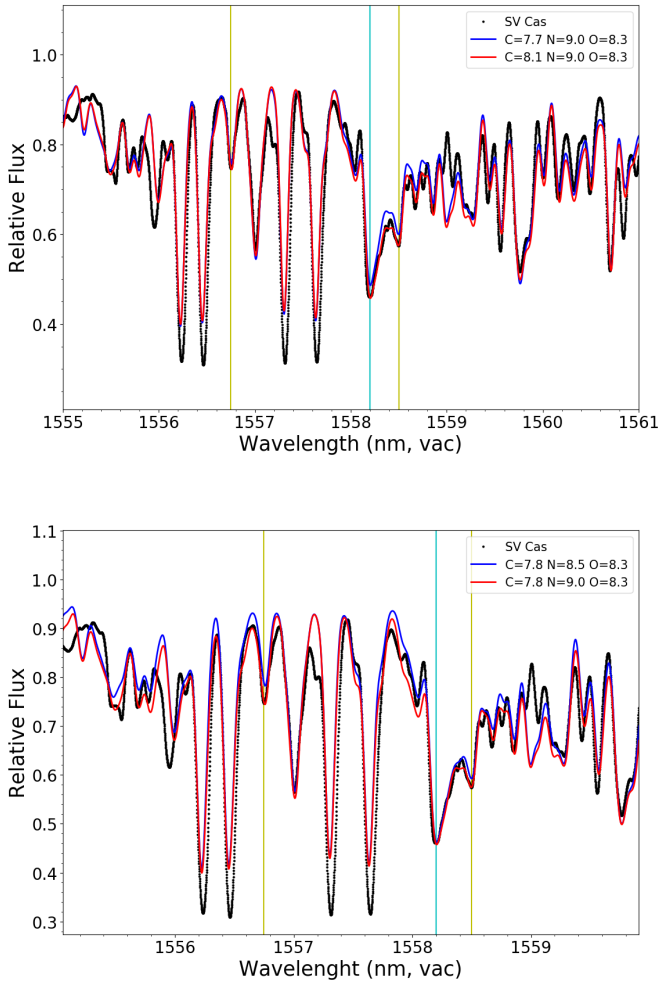

Figure 4.3: Sensitivity of the synthetic spectra (constructed for the star SV Cas, in black dots) around 1558 nm to changes in the abundances of C (*top panel*) and N (*bottom panel*). The cyan vertical lines indicate the position of the CO 1558.20 nm bandhead, while the yellow vertical lines mark the CN 1556.75 and 1558.50 nm lines.

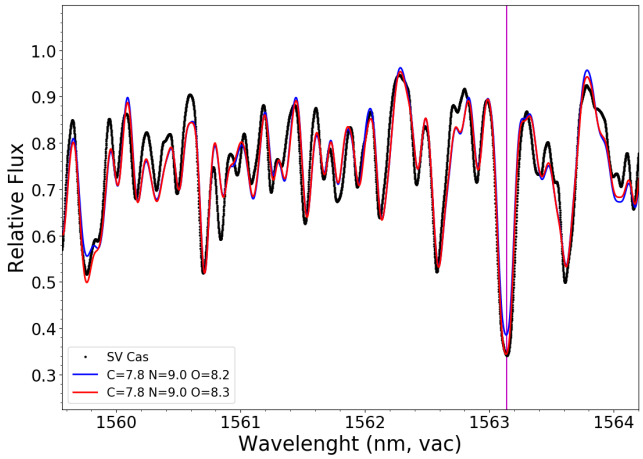

Figure 4.4: Sensitivity of the synthetic spectrum (constructed for the star SV Cas, in black dots) around 1562 nm to changes in the O abundances. The magenta vertical line indicates the position of the OH 1563.14 nm line.

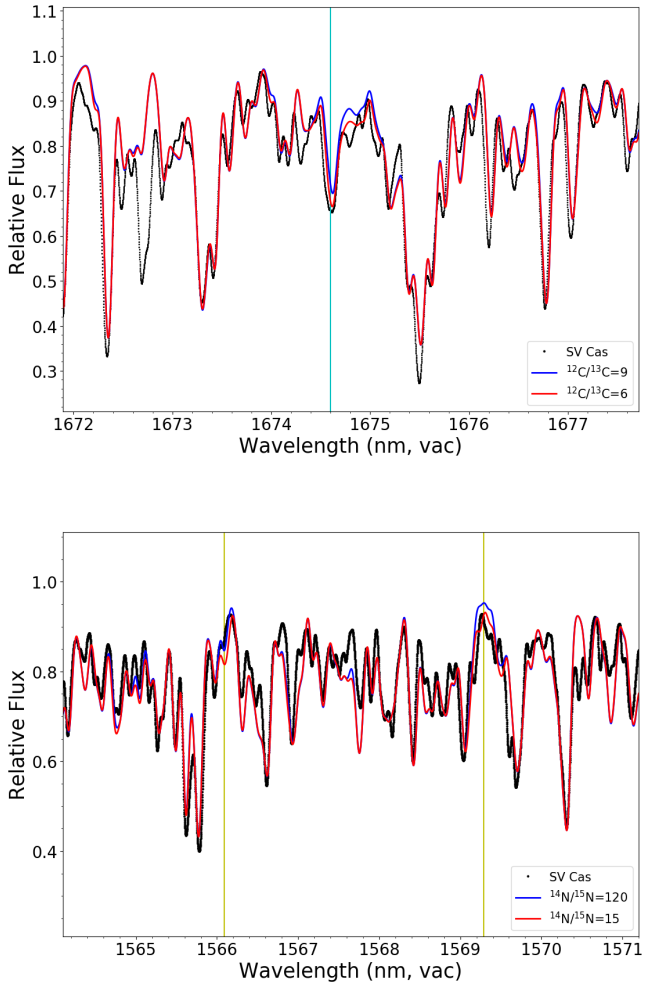

Figure 4.5: Sensitivity of the synthetic spectra (constructed for the star SV Cas, in black dots) around 1675 and 1568 nm to changes in the $^{12}C/^{13}C$ (*top panel*) and $^{14}N/^{15}N$ (*bottom panel*) ratios, respectively. The color vertical lines indicate the position of the lines used to obtain the $^{12}C/^{13}C$ (*cyan*; 1674.60 nm) and $^{14}N/^{15}N$ (*yellow*; 1566.09 and 1569.82 nm). See the text for more details.

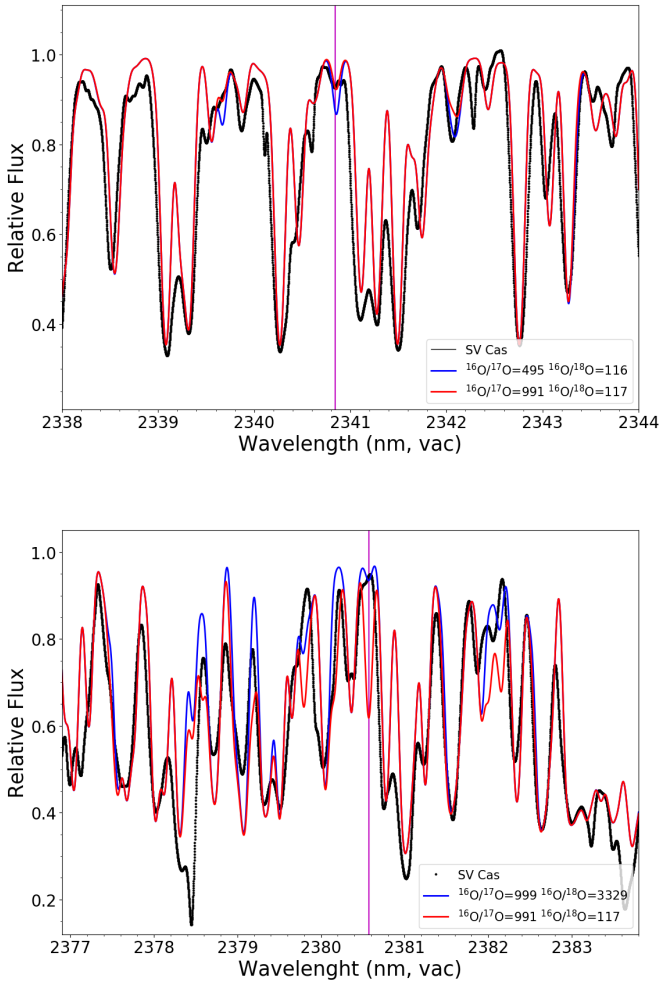

Figure 4.6: Sensitivity of the synthetic spectra (constructed for the star SV Cas, in black dots) around 2341 and 2380 nm to changes in the $^{16}O/^{17}O$ (*top panel*) and $^{16}O/^{18}O$ (*bottom panel*) ratios, respectively. The magenta vertical lines indicate the position of the lines used to obtain the $^{16}O/^{17}O$ and $^{16}O/^{18}O$ (2340.84 and 2380.57 nm, respectively) isotopic ratios. See the text for more details.

and the available blended lines are weak and not very sensitive to variations of the isotopic ratios. In any case, we have selected a small group of lines among the most sensitive lines to variations in the $^{14}N/^{15}N$ ratio in order to obtain a rough average ratio from those lines (see Figures 4.5). The final set of lines for the $^{14}N/^{15}N$ ratio ratio is: 1550.76, 1554.32, 1563.29, 1566.09 and 1569.29 nm, which may have some contribution from$^{12}C^{14}N$, $^{12}C^{15}N$, $^{13}C^{14}N$, H_2O and OH.

4.4 CNO abundances and isotopic ratios

There are two main techniques for measuring the CNO abundances and isotopic ratios from stellar spectra: CoG analysis and spectral synthesis. The CoG method (see e.g. Dominy & Wallerstein 1987; Hinkle et al. 2016) is a technique for deriving elemental abundances including many simplifications that can be dealt with more depth by spectrum synthesis, but, in principle, very powerful if only isotopic ratios are derived (Hinkle et al. 2016). Here, we have derived the CNO abundances and isotopic ratios by using spectral synthesis techniques, as used for example by García-Hernández et al. (2009b), Souto et al. (2016) and Abia et al. (2017a,b) among many others. In this work, we have followed the Souto et al. (2016) methodology, as described in Smith et al. (2013): we first derive the C abundances from CO, then derive O from OH and, finally, N from CN lines[3]. We tested also starting from OH (O abundance), then CO (C abundance) and finally CN (N abundance), finding that the obtained CNO abundances are the same, but the Souto et al. (2016) methodology provides a faster convergence towards the final abundance values. This is because our synthetic spectra are less sensitive to changes in the N abundance than to C and O, so a lower number of steps in the iterative process is needed to obtain the final CNO abundances.

4.4.1 Elemental abundances - C, N and O

In Table 4.2 we list the CNO abundances and isotopic ratios in our small sample of massive AGB stars at the beginning of the TP phase. The Figures 4.7-4.12 show examples of the synthetic fits to the observational spectra of the sample star SV Cas around several spectral regions. The hydrostatic synthetic spectra fit well the SV Cas ones, resulting in $\log\varepsilon(C)=7.8\pm0.2$ dex,

[3]We have to take in mind that these cool stars display a lot of molecular lines (millions even for a single molecule!) and all these molecules are not perfectly known; only the transitions measured at the laboratory are well known, while the rest of lines come from theoretical models and extrapolations.

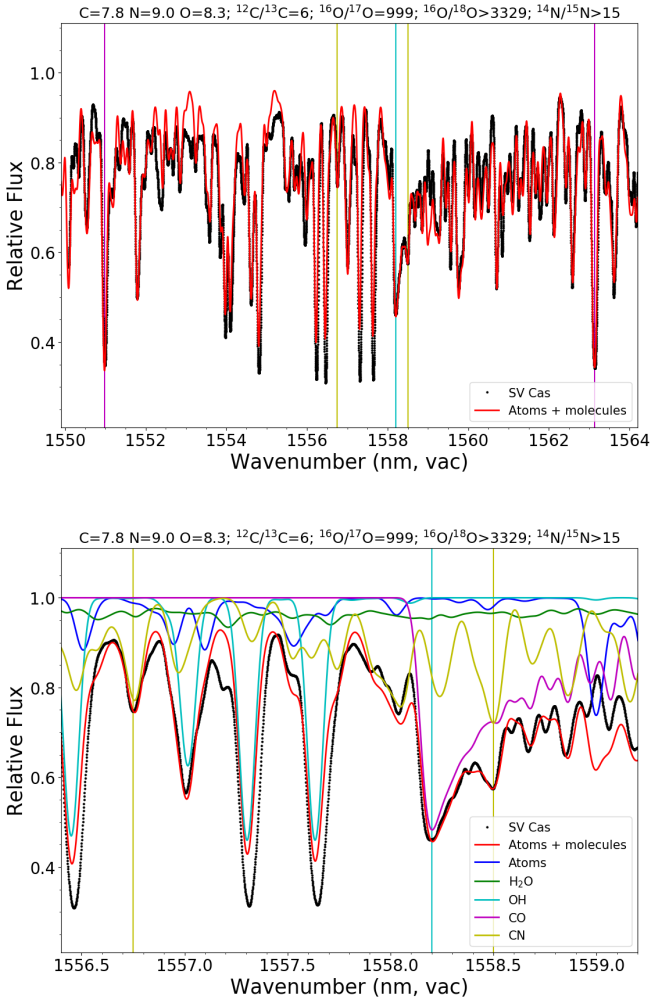

Figure 4.7: The SV Cas observed spectrum (*black* dots) and the best synthetic fit (*red* line) in the spectral region around 1557 nm, which is used to determine the CNO abundances. A zoom in the molecular contribution to the total synthetic spectrum is also showed (*bottom panel*). The color vertical lines indicate the spectral features/lines used to obtain the abundances of C (*cyan* line; CO 1558.20 nm), N (*yellow* lines; CN 1556.75 and 1558.50 nm) and O (*magenta* lines; OH 1550.98 and 1563.14 nm).

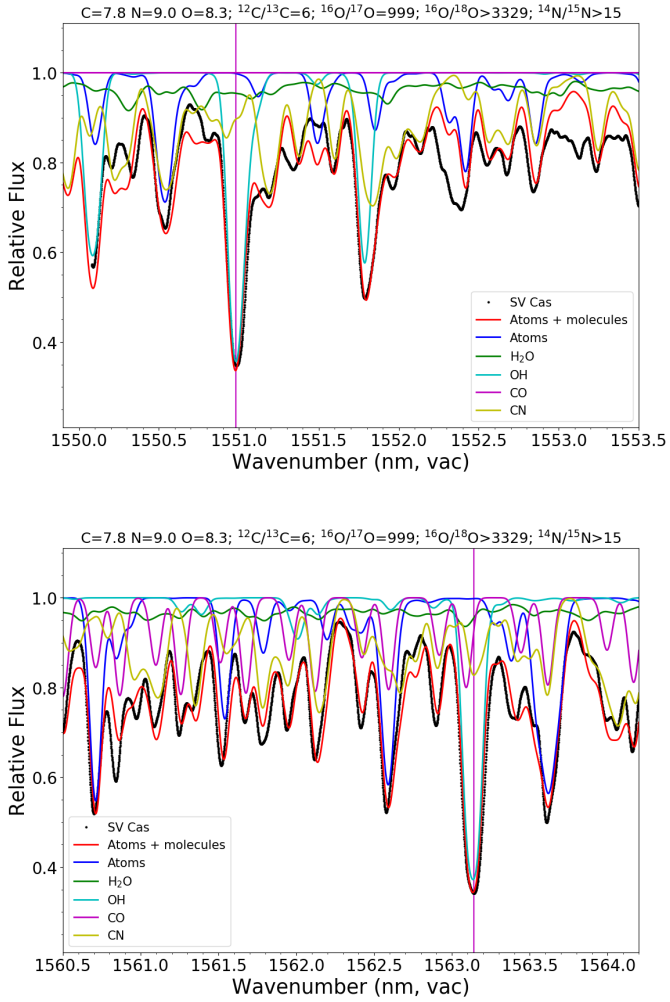

Figure 4.8: Zoom in the molecular contribution to the total synthetic spectrum in the spectral regions around 1551 nm (*top panel*) and 1563 nm (*bottom panel*. The SV Cas observed spectrum (*black* dots) and the best synthetic fit (*red* line) in those spectral regions are showed. The *magenta* vertical lines indicate the lines used to obtain the abundances of O (OH 1550.98 and 1563.14 nm).

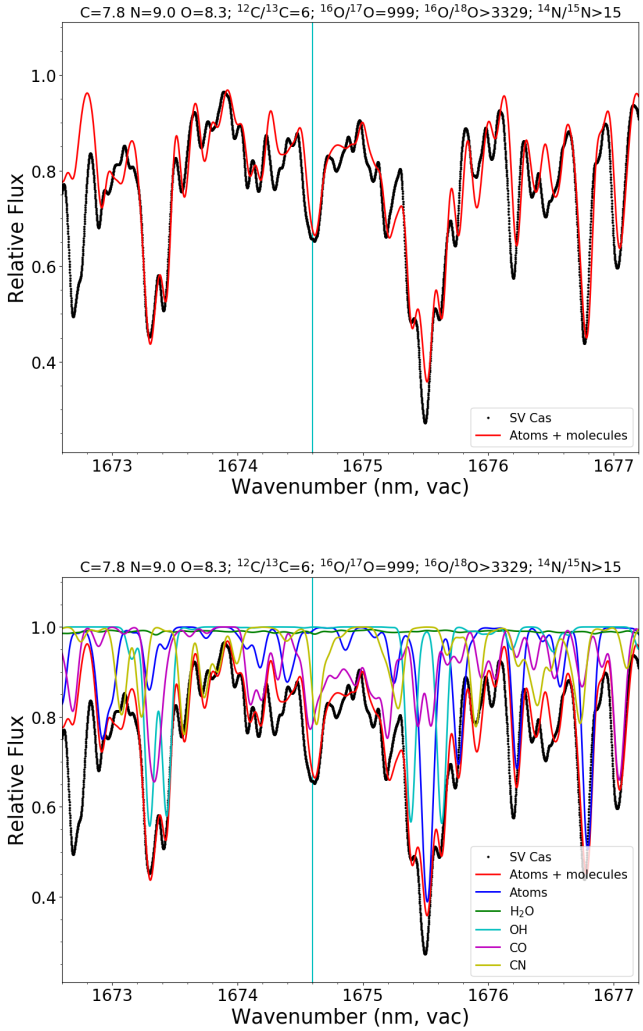

Figure 4.9: The SV Cas observed spectrum (*black* dots) and the best synthetic fit (*red* line) in the spectral region around 1674 nm, which is used to determine the ^{12}C/^{13}C ratio. The molecular contribution to the total synthetic spectrum is also showed (*bottom panel*). The cyan vertical line indicates the position of ^{13}CO 1674.60 nm, blended with ^{12}CN.

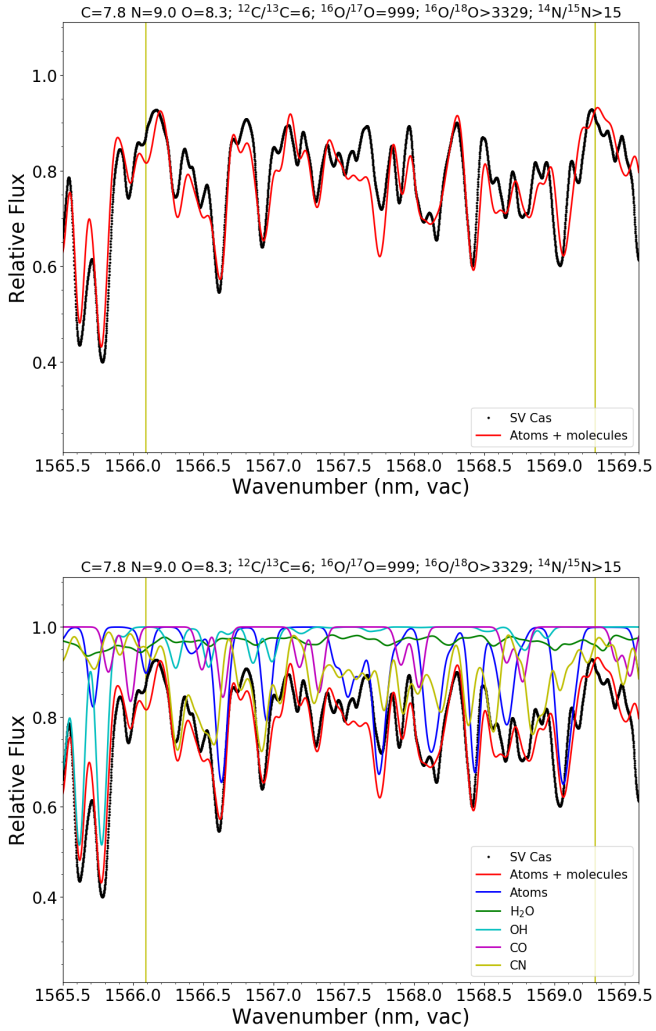

Figure 4.10: The SV Cas observed spectrum (*black* dots) and the best synthetic fit (*red* line) in the spectral region around 1567 nm, which is used to determine the $^{14}N/^{15}N$ ratio. The molecular contribution to the total synthetic spectrum is also showed (*bottom panel*). The yellow vertical lines indicate the position of $^{12}C^{15}N$ 1566.09 and 1569.82 nm.

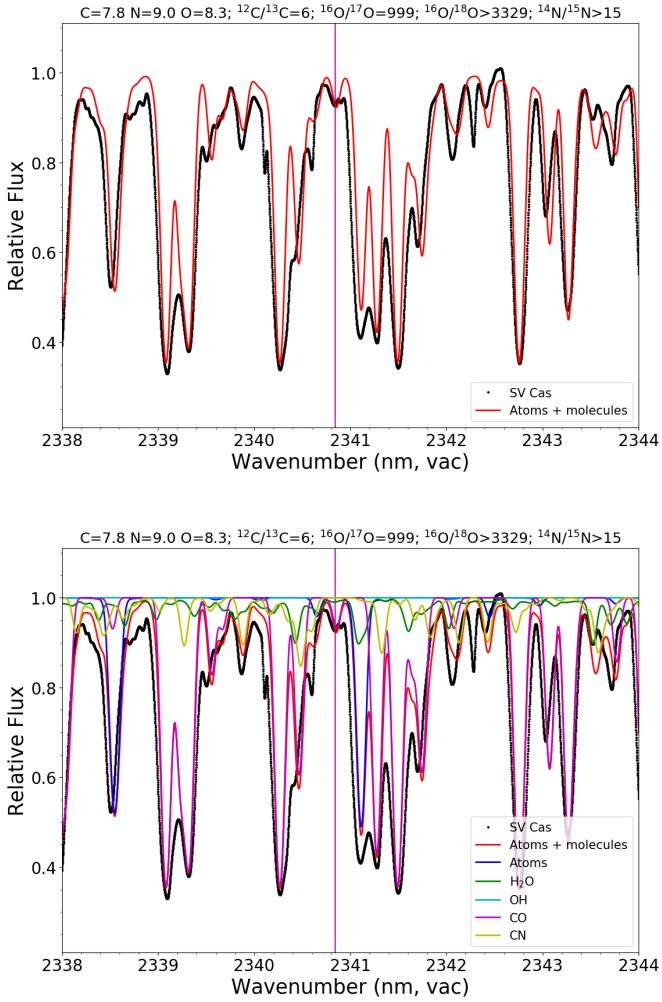

Figure 4.11: The SV Cas observed spectrum (*black* dots) and the best synthetic fit (*red* line) in the spectral region around 2340 nm, which is used to determine the $^{16}O/^{17}O$ ratio. The molecular contribution to the total synthetic spectrum is also showed (*bottom panel*). The magenta vertical line indicates the position of $^{12}C^{17}O$ 2340.84 nm.

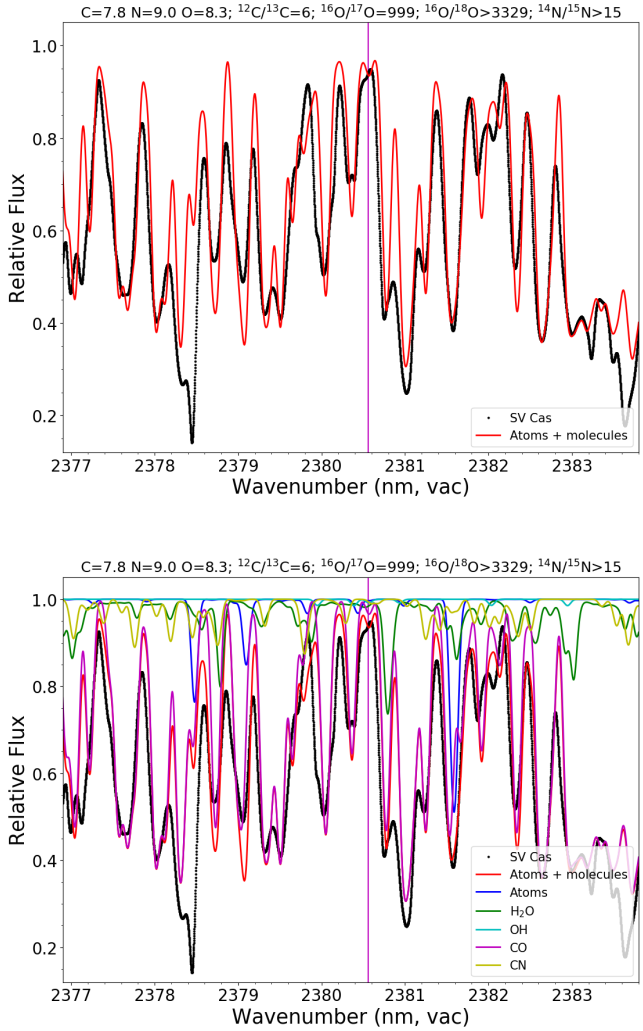

Figure 4.12: The SV Cas observed spectrum (*black* dots) and the best synthetic fit (*red* line) in the spectral region around 2380 nm, which is used to determine the $^{16}O/^{18}O$ ratio. The molecular contribution to the total synthetic spectrum is also showed (*bottom panel*). The magenta vertical line indicates the position of $^{12}C^{18}O$ 2380.57 nm.

Table 4.2: Derived CNO abundances and isotopic ratios for the sample stars.

IRAS name	C	N	O	$^{12}C/^{13}C$	$^{16}O/^{17}O$	$^{16}O/^{18}O$	$^{14}N/^{15}N$
15152+3632	8.1±0.2	9.5±1.1	8.5±0.4	9±6	1427±619	⩾3330	>4
18072+3100	7.3±0.2	>9.4	8.0±0.5	6±4	100±33	>50	>15
18141+0340	7.5±0.2	9.6±0.8	8.0±0.4	3±1	252±124	>76	>4
SV Cas	7.8±0.2	9.0±0.8	8.3±0.7	6±2	999±300	⩾3329	>15
RU Cyg	8.1±0.3	9.0±0.6	8.4±0.3	9±2	553±206	⩾498	>30

The CNO elemental abundances are listed as logε(X). The uncertainties represent the formal error due to the sensitivity of the derived CNO abundances and isotopic ratios to small changes in the model atmosphere parameters (ΔT_{eff} = ±100 K, Δlog g = ±0.5, ΔZ = ±0.2, $\Delta\xi$ = ±0.5 km s^{-1} and $\Delta FWHM$ = ±50 mÅ) for each star.

logε(N)=9.0±0.8 dex and logε(O)=8.3±0.7 dex elemental abundances (see Figures 4.7-4.8). The photosphere solar CNO abundances from Grevesse et al. (2007) are logε(C)=8.39, logε(N)=7.78 and logε(O)=8.66 dex, respectively. McSaveney et al. (2007) derived the CNO abundances in two relatively blue intermediate-mass AGB stars, HV 2576 and NGC 1866 in the LMC (Z = 0.01 or [Fe/H] = -0.3 dex), obtaining very large N enhancements, [^{14}N/Fe] = +1.17 and +0.97 dex, C deficiency, [^{12}C/Fe] = −1.13 and −0.63 dex, and regarding the O case, HV 2576 is sligthly O deficient, [^{16}O/Fe] = −0.13 dex, while NGC 1866 is O-rich, [^{16}O/Fe] = +0.54 dex. These values confirmed, for the first time, that the activation of the third dredge-up and HBB can produce significant primary N in low-metallicity intermediate-mass AGB stars.

This is the first time that the elemental CNO abundances are derived in truly massive AGB stars at solar metallicity. Our C abundances are in the range [C/Fe] = −1.09 - −0.29 dex, with ⟨[C/Fe]⟩ = −0.69 dex, while the N abundances show an average of ⟨[N/Fe]⟩ = +1.52 dex for values between [N/Fe] = +1.22 - +1.82 dex. In the O case, our stars display abundances in the range [O/Fe] = −0.66 - −0.16 dex, and an average ⟨[O/Fe]⟩ = −0.41 dex. Our smal sample of massive Galactic AGB stars thus display subsolar C and O abundances, but supersolar N, even higher than the N enrichment derived by McSaveney et al. (2007) in two intermediate-mass AGB stars in the LMC. This N enhancement confirm the HBB activation in our small sample of massive Galactic AGB stars at solar metallicty. This observation is independent of their high Li abundances (see Table 4.1), which also indicate the activation of the HBB in massive solar metallicity AGB stars (see Chapter 3, García-Hernández et al. 2007a, 2013).

4.4.2 Isotopic ratios for C, N and O

We have obtained for the first time, by spectral synthesis, the CNO isotopic ratios in truly massive Galactic AGB stars at the beginning of the TP phase. In Table 4.2 we list the values of $^{12}C/^{13}C$ and $^{16}O/^{17}O$ obtained, as well as our estimated lower limits for $^{16}O/^{18}O$ and $^{14}N/^{15}N$. In Figures 4.5-4.6 we display the synthetic fits to the sample star SV Cas made to estimate the $^{12}C/^{13}C$, $^{14}N/^{15}N$, $^{16}O/^{17}O$ and $^{16}O/^{18}O$ isotopic ratios. Our estimated C isotopic ratios in the sample stars are in the range $^{12}C/^{13}C$ = 3-9. Regarding the O isotopic ratios, we estimated $100 \leq {}^{16}O/^{17}O \leq 1427$ and $^{16}O/^{18}O > 50$[4]. Finally, the $^{14}N/^{15}N$ isotopic ratios are always estimated to be higher than 4 (see Table 4.2).

In the literature there are only a couple of works reporting the C and O isotopic ratios in massive AGB stars, while we could not find any work reporting the N isotopic ratios in such stars:

i) In a few (5) extreme OH/IR stars (i.e. highly evolved massive AGB stars with no optical counterpart), observed in the far-IR by the Herschel Space Observatory[5], Justtanont et al. (2013) obtained a range for the $^{12}C/^{13}C$ ratio between 2 and 30, with three stars displaying $^{12}C/^{13}C \leq 10$ consistent with HBB expectations and two stars showing $^{12}C/^{13}C \sim 30$ but with large uncertainties. They could observe the H_2O isotopologues in three of these stars. They obtained $^{18}O/^{17}O < 0.1$ in two stars, while for the OH/IR star WX PSc they reported a higher value of $^{18}O/^{17}O$=1.5. In a subsequent and more detailed work, Justtanont et al. (2015) increased the sample of extreme OH/IR stars with Herschel H_2O isotopologues observations to 9[6] objects and they obtained an upper limit of $^{18}O/^{17}O < 1$. Justtanont et al. (2013, 2015) concluded that their O isotopic data support the idea that extreme OH/IR stars experience HBB and are quite evolved AGB stars more massive than $\sim$5 $M_\odot$. We note that the Li, Rb and Zr abundances are not known in the Justtanont et al. (2013, 2015) sample of extreme OH/IR stars because these stars, at the end

[4] In the cases of IRAS 18072+3100 and IRAS 18141+0340, our fits are worse at 2.3 μm (more complex spectra), so the $^{16}O/^{18}O$ lower limits listed in Table 4.2 are more conservative than in the other stars due to the larger uncertainties.

[5] We note that the Herschel H_2O isotopologues observations in a small sample (4) of M-type AGB stars (not classified as long-period extreme OH/IR stars) have been studied by Danilovich et al. (2017) but their estimated O isotopic ratios (in the ranges $^{16}O/^{17}O$= 558-1620, $^{16}O/^{18}O$ = 214-833 and $^{17}O/^{18}O$ = 0.15-0.69) were consistent with low-mass (< 1.5 $M_\odot$) progenitors not suffering HBB.

[6] We note that Justtanont et al. (2015) removed WX PSc from the extreme OH/IR extended sample with Herschel H_2O data, but De Nutte et al. (2017) got, from radio CO isotopologue observations, an even higher $^{18}O/^{17}O$ isotopic ratio of 3.5. The OH/IR star WX PSc is, in terms of the $^{18}O/^{17}O$ ratio, an outlier among the extreme OH/IR stars.

of the AGB phase, are completely obscured in the optical range (see García-Hernández et al. 2007a). Our estimated $^{18}O/^{17}O$ upper limits are in the range 0.3-0.9 for the three sample stars (IRAS 18071+3100, IRAS 18181+0340 and RU Cyg), with the stars IRAS 15152+3632 and SV Cas displaying $^{18}O/^{17}O >$ 2 and 3, respectively.

ii) Hinkle et al. (2016) applied the CoG method to high-resolution FTS near-IR spectra to estimate the CNO isotopic composition in a sample of 46 nearby Mira and SRa-type variable AGB stars with different spectral types, (35 M-, 4 S-, 1 SC- and 6 C-type stars). For the 35 M-type AGB stars, they reported $^{12}C/^{13}C$ ratios in the range 8-45 with only 5 stars with $^{12}C/^{13}C \leq$ 10, concluding that their sample of stars is dominated by low-mass AGB stars. Their relatively high $^{12}C/^{13}C$ ratios in M-type AGBs together with their reported values of $^{16}O/^{17}O$ and $^{16}O/^{18}O$ in the ranges of 100-4467 and 71-5623, respectively, led them to conclude that no star in their sample shows evidence for the activation of HBB. Remarkably, two of our sample stars, SV Cas and RU Cyg, were also studied in Hinkle et al. (2016). They reported $^{12}C/^{13}C$ = 10±2 and 32±10 for SV Cas and RU Cyg, respectively, while we estimate $^{12}C/^{13}C$ = 6±2 (SV Cas) and 9±2 (RU Cyg). Our $^{12}C/^{13}C$ values are consistent with the HBB expectations in massive AGB stars (see Section 4.5). In addition, the activation of HBB in these stars is confirmed independently by their strong N enhancements (see Subsection 4.4.1 above) and Li overabundances (see Chapter 3 and García-Hernández et al. 2013). Thus, we believe that our $^{12}C/^{13}C$ ratios, by spectral synthesis on high-resolution near-IR spectra, are more precise than those obtained by the CoG method. Finally, the range of our O isotopic ratio estimates agree well (within the errors) with those reported by Hinkle et al. (2016). For the two stars in common with us, they obtained $^{16}O/^{17}O$ = 708±300 and 887±200 for SV Cas and RU Cyg, respectively, while our estimates are $^{16}O/^{17}O$ = 999±300 (SV Cas) and 553±206 (RU Cyg). Our estimated $^{16}O/^{18}O$ lower limits are, respectively, ≥3329 and ≥498, while Hinkle et al. (2016) obtained the values of 5623±2500 (SV Cas) and 447±200 (RU Cyg).

iii) In a recent conference proceeding, Abia et al. (2017a) reported preliminary results on the CNO isotopic ratios in two massive Galactic O-rich (C/O < 0.5) AGB stars (V1415 Aql and V697 Her). They used the same method as used in this thesis; i.e. spectral synthesis on high-resolution GIANO/TNG near-IR spectra. However, their sample stars are presumably more evolved than ours. This is because both stars already display the strong blue-shifted Rb I 7800 Å lines that are characteristic of evolved massive AGB stars (García-Hernández et al. 2006). According to García-Hernández et al. (2007a), the star V697 Her is Li-rich, while V1415 Aql is Li-poor. Both stars, however, display OH masers

Table 4.3: Derived CNO abundances and isotopic ratios with pesudo-dynamical models in two sample stars.

Star name	C	N	O	$^{12}C/^{13}C$	$^{16}O/^{17}O$	$^{16}O/^{18}O$	$^{14}N/^{15}N$
SV Cas	7.8±0.3	9.0±0.8	8.3±0.4	6±4	999±414	≥3329	>15
RU Cyg	8.1±0.4	9.0±0.6	8.4±0.3	9±4	553±271	≥498	>30

The uncertainties represent the formal error due to the sensitivity of the derived CNO abundances and isotopic ratios to small changes in the model atmosphere (ΔT_{eff} = ±100 K, Δlog g = ±0.5, ΔZ = ±0.2, Δt = ±0.5 km s^{-1} and $\Delta FWHM$ = ±50 mÅ) and wind ($\Delta\beta$ = ±0.2, $\Delta log(\dot{M}/M_{\odot}yr^{-1})$ = ±0.5 and Δv_{exp}(OH) = ±5 km s^{-1}) parameters for each star.

with high expansion velocities (> 12 kms^{-1}) and long Mira-like periods (≥ 440 days), which are typical of massive AGB stars of OH/IR type that experience HBB (García-Hernández et al. 2006, 2007a); the only difference is that both stars are still detectable in the optical range. Indeed, Abia et al. (2017a) had difficulties in modeling the complex spectra of these two evolved massive AGBs - our synthetic fits to the simpler near-IR spectra of massive AGB stars at the beginning of the TP phase are superior to them. In any case, in V1415 Aql they reported $^{12}C/^{13}C$ = 20, $^{16}O/^{17}O$ > 600, and $^{16}O/^{18}O$ > 1000, while in V697 Her they estimated $^{12}C/^{13}C$ = 30 and $^{16}O/^{18}O$ > 1000. Their preliminary $^{12}C/^{13}C$ ratios are higher than ours and than those expected from HBB. Their O isotopic ratios (lower limits) are in good agreement with those derived for our sample stars IRAS 15152+3632 and SV Cas, which display the highest O isotopic ratios in our sample.

In short, our low (∼ 3-9) $^{12}C/^{13}C$ ratios in massive O-rich AGB stars at the beginning of the TP phase are consistent with the HBB expectations. The operation of HBB in these stars is confirmed independently by their strong N enhancements and Li overabundances (see Chapter 3).

4.4.3 CNO abundances and isotopic ratios by using pseudo-dynamical models

We have determined the CNO abundances and isotopic ratios in our small sample of massive AGB stars at the beginning of the TP phase by using classical hydrostatic model atmospheres. In the previous chapters, we explored the circumstellar effects on the Rb, Zr, Li and Ca in massive Galactic O-rich AGB stars, resulting in that the Rb abundances are strongly affected by the presence of a circumstellar envelope, while in the Li, Ca and Zr cases the effect of the extended atmosphere is almost negligible. We have explored such circumstellar

effects with a modified version of the spectral synthesis code *Turbospectrum* (Alvarez & Plez 1998; Plez 2012). Here we extended such exploration to the near-IR in order to study their possible influence on the CNO abundances and isotopic ratios. For this, we have studied two stars of our sample, SV Cas and RU Cyg, with pseudo-dynamical models. This is because we previously obtained their wind parameters ($\dot{M}$, β and v_{exp}(OH)) from visible spectra (see Chapter 3). Figure 4.13 shows that the pseudo-dynamical synthetic spectra are practically identical to the hydrostatic ones, and that the CNO abundances and the isotopic ratios obtained by using extended atmospheres, as listed in Table 4.3, are practically the same than those obtained from the hydrostatic models (see Table 4.2). Therefore, this suggests that the determination of the CNO abudances and isotopic ratios in massive O-rich AGB stars at the beginning of the TP phase is not affected by the presence of a circumstellar envelope. Thus, the abscense of important circumstellar effects in the H-band, is not surprising if we consider that the near-IR (e.g. H-band) spectral lines are formed deeper in the atmosphere where the circumstellar effects (and other effects like NLTE) are less severe than in the optical domain.

4.5 Comparison with AGB nucleosynthesis models

In contrast to the previous chapters, where we compared with different nucleosynthesis models, here we have mainly compared our CNO elemental abundances and isotopic ratios with solar metallicity massive (3-8 $M_{\odot}$) AGB stars predictions from the Karakas & Lugaro (2016) nucleosynthesis models (Monash models; see also below). The most important input physics to the stellar nucleosynthesis is that the Karakas & Lugaro (2016) models use the Vassiliadis & Wood (1993) mass-loss prescription, the mixing lenght theory of convection (MLT; Böhm-Vitense 1958) and assume instantaneous mixing in the convective regions. Moreover, the convective overshoot is not included in the calculations, but an algorithm is implemented to try to search for a neutrally stable point from the formal Schwarzschild boundary, as described by Lattanzio (1986), between the radiative and convective regions. In intermediate-mass stellar models, this method has been shown to increase the efficiency of TDU (Frost & Lattanzio 1996). We refer the reader to Karakas (2014) and Karakas & Lugaro (2016) for more details about the input physics and the numerical methods.

It is to be noted here that we have not compared with the FRUITY[7] models (Cristallo et al. 2015) because the HBB activation is not predicted in these

[7]FUll-Network Repository of Updated Isotopic Tables and Yields: http://fruity.oa-abruzzo.inaf.it/.

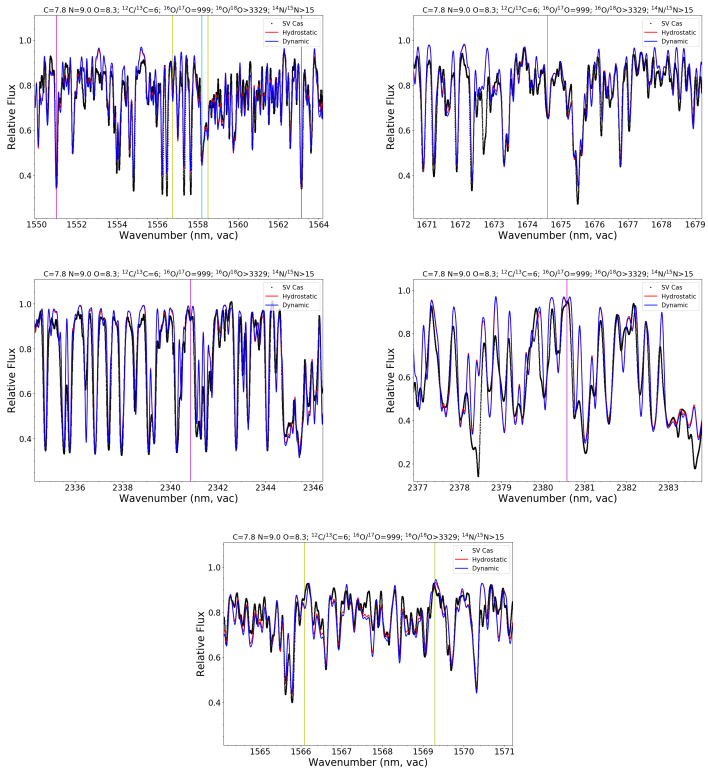

Figure 4.13: A zoom in the spectral regions selected to obtain the CNO abundances and isotopic ratios in SV Cas (black dots) and the best hydrostatic (red lines) and pseudo-dynamical (blue lines) models. The color vertical lines in the *top left panel* indicate the position of the molecular lines used to obtain the abundances of C (*cyan*; CO 1558.20 nm), N (*yellow*; CN 1556.75 and 1558.50 nm) and O (*magenta*; OH 1550.98 and 1563.14 nm). In the other panels we indicate the position of the features/lines used to derive the ^{12}C/^{13}C (*cyan*; *top right panel*), ^{16}O/^{17}O and ^{16}O/^{18}O (*magenta*; both *middle panels*) and ^{14}N/^{15}N (*yellow*; *bottom panel*) isotopic ratios.

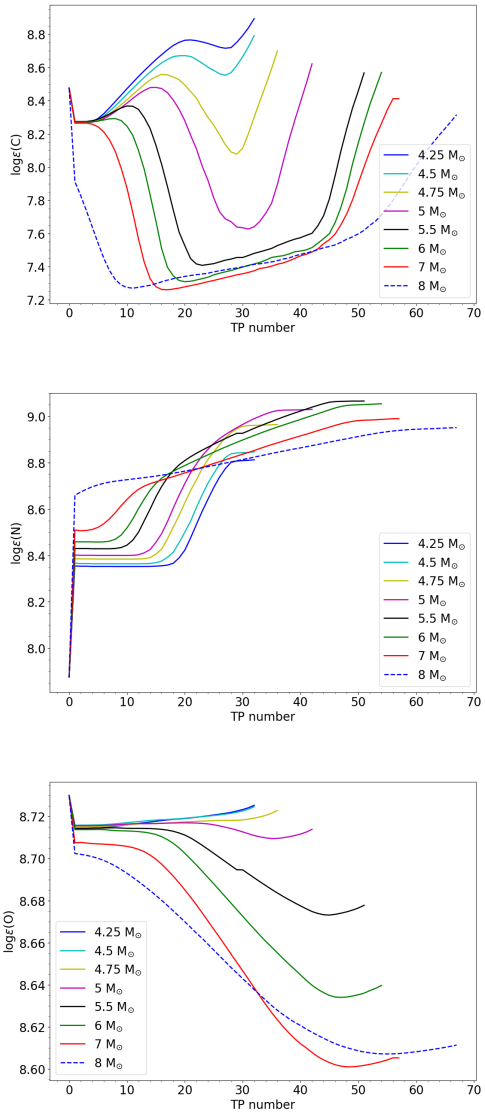

Figure 4.14: Theoretical Monash predictions for the C (*top panel*), N (*middle panel*) and O (*bottom panel*) elemental abundances against TP number for the progenitor masses that experience HBB at solar metallicity. We note that only for the 4.25 $M_\odot$ model, Karakas & Lugaro (2016) assume $M_{mix} = 10^{-4}$ $M_\odot$.

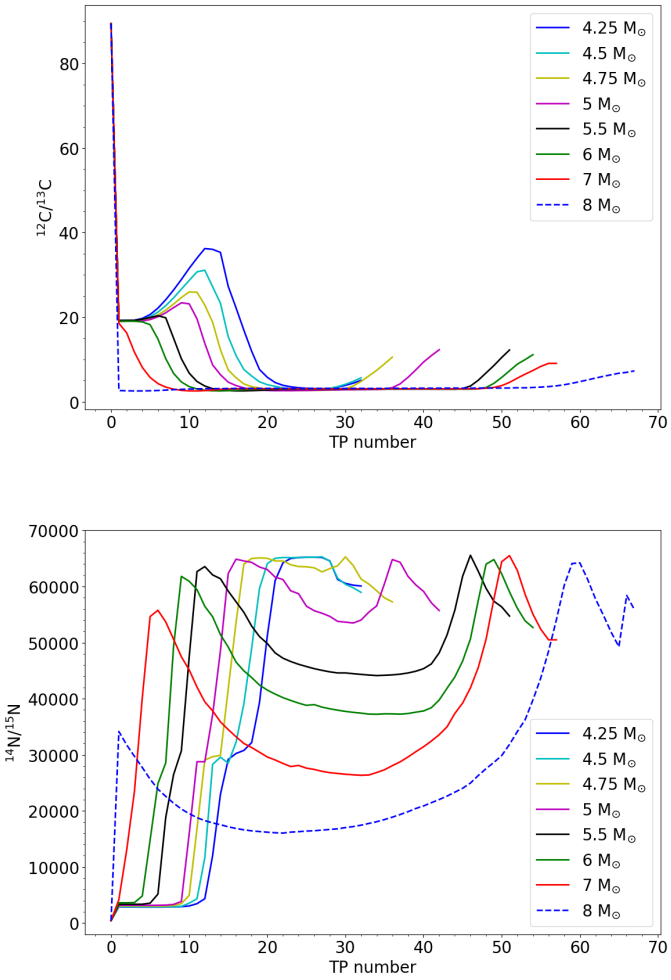

Figure 4.15: Theoretical Monash predictions for the $^{12}C/^{13}C$ (*top panel*) and $^{14}N/^{15}N$ (*bottom panel*) isotopic ratios against TP number for the progenitor masses that experience HBB at solar metallicity. We note that only for the 4.25 $M_{\odot}$ model, Karakas & Lugaro (2016) assume $M_{mix} = 10^{-4}$ $M_{\odot}$.

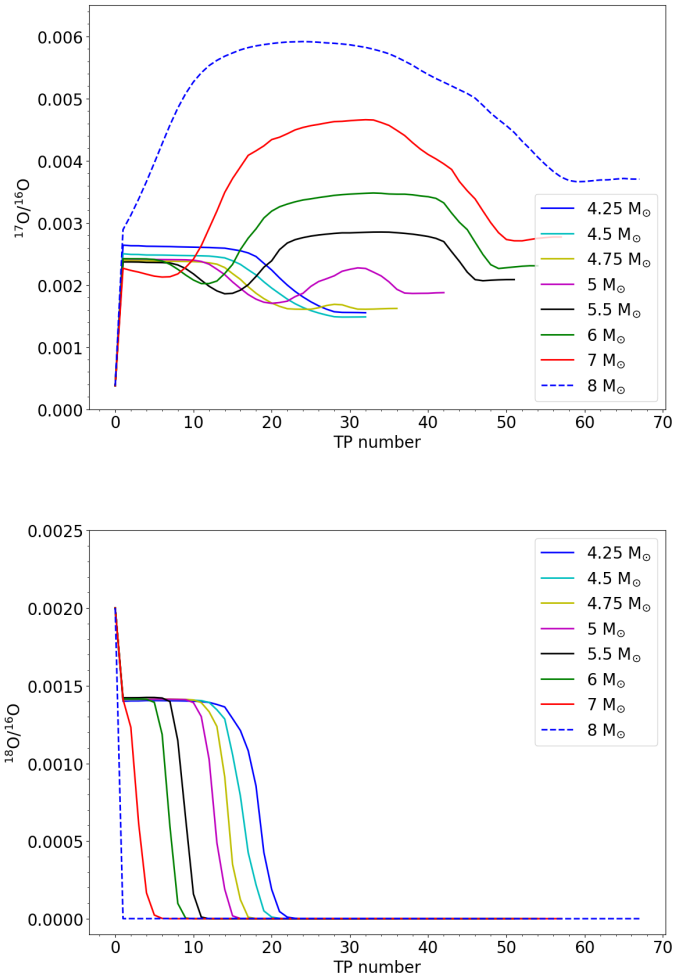

Figure 4.16: Theoretical Monash predictions for the $^{17}O/^{16}O$ (*top panel*) and $^{18}O/^{16}O$ (*bottom panel*) isotopic ratios against TP number for the progenitor masses that experience HBB at solar metallicity. We note that only for the 4.25 $M_\odot$ model, Karakas & Lugaro (2016) assume $M_{mix} = 10^{-4}$ $M_\odot$.

models, in strong contrast with our CNO values and other theoretical nucleosynthesis models and observations of massive AGB stars at solar metallicity (see e.g. García-Hernández et al. 2013; Pérez-Mesa et al. 2019, for more details). For example, the $^{12}C/^{13}C$ isotopic ratios from the FRUITY models, for masses in the range M = 1.3-6.0 $M_{\odot}$, never reach the low values observed in our sample of massive AGB stars. Moreover, we have not included a detailed comparison with the NuGrid/MESA theoretical predictions because Ritter et al. (2018) states that the final yields of CNO isotopes based on their nested-network method are similar to the Monash models. Regarding the ATON models, unfortunately they have not published (i.e. publicly available) the CNO elemental abundances and isotopic ratios for each TP (i.e. temporal evolution) in massive AGB stars at solar metallicity. However, Figure 11 in Di Criscienzo et al. (2016) shows the ATON surface $^{12}C/^{13}C$ and $^{18}O/^{17}O$ ratios versus the actual stellar mass (decreasing during the evolution) for solar metallicity ∼3.5-8 $M_{\odot}$ AGB stars, experiencing HBB. Qualitavely, there is a significant reduction of the surface $^{12}C/^{13}C$ and $^{18}O/^{17}O$ ratios as soon as HBB begins; e.g. $^{12}C/^{13}C$∼4 and $^{18}O/^{17}O$∼0.001 are quickly reached (when only a tiny amount of mass is lost) for progenitor masses higher than 4 $M_{\odot}$. In short, the ATON models predict a very fast (qualitatively consistent with the beginning of the TP phase) and dramatical reduction of the initial $^{12}C/^{13}C$ and $^{18}O/^{17}O$ ratios in massive HBB AGB stars, which is consistent with our interpretation of our sample stars being truly massive AGB stars at the beginning of the TP phase.

In this section, we assume the meteoritic community convention for the oxygen isotopic ratios, the inverse of the astronomical convention, to allow straightforward comparisons with the literature data (see Table 4.4). In Figures 4.14-4.16 we display the nucleosynthesis theoretical predictions from the Monash models for stellar masses between 4.25 and 8 $M_{\odot}$, in which Karakas & Lugaro (2016) find the activation of the HBB at solar metallicity. We note that in the 4.25 $M_{\odot}$ case, Karakas & Lugaro (2016) assume that a partial mixing of $M_{mix} = 10^{-4}$ $M_{\odot}$ occurs between the convective H-rich envelope and the intershell at the deepest extent of each TDU, so that the protons injected in the He intershell are captured by ^{12}C to produce a region rich in ^{13}C, the so-called ^{13}C pocket (see Karakas & Lattanzio 2014; Karakas & Lugaro 2016, for more details). We have plotted the predicted CNO elemental abundances and isotopic ratios against the number of TPs experienced by the stars as an indicator of the lifetime of the stars. We have compared the Monash theoretical predictions with our CNO elemental/isotopic abundances in order to know if our sample stars are truly massive AGB stars at the beginning of the TP phase and to estimate their progenitor masses.

Thus, in the following we compare the CNO elemental abundances and iso-

topic ratios obtained in each sample star with the Monash predictions for solar metallicitiy massive AGB stars mentioned above (Figures 4.14-4.16). In Appendix C we present the plots where we show the comparison between our derived CNO elemental/isotopic abundances and theoretical predictions for each sample star. We note that the isotopic ratios obtained (especially the $^{12}C/^{13}C$ and $^{17}O/^{16}O$ ratios) are more robust than the CNO elemental abundances because they are less affected by variations of the stellar parameters used in the spectral modelling, and they will thus have more weight in the comparison. Finally, in the comparison, we also use qualitatively the detection of Li and no *s*-process elements (Rb and Zr) in all sample stars. This is because the Monash models predict that the Li abundance is high near the beginning of the AGB, before any *s*-process nucleosynthesis has reached the stellar surface. The Monash models also show that the Li abundance goes down more gradually during the AGB than in models with more efficient HBB and convection (Di Criscienzo et al. 2016).

IRAS 15152+3632

The CNO abundances of IRAS 15152+3632, listed in Table 4.2, can be reproduced by the massive AGB Monash models for all progenitor stellar masses in the first TPs (around 10-15 TPs) taking into account the uncertainties, alike the $^{14}N/^{15}N$ lower limit, because we considere that our sample stars are massive AGB stars at the beginning of the TP phase. The $^{17}O/^{16}O = 7.018\times10^{-4}$ isotopic ratio is only reached before the first TP but for all progenitor masses. Regarding the $^{18}O/^{16}O$ upper limit, $^{18}O/^{16}O < 3.003\times10^{-4}$, this value is reproduced by the Monash models with masses larger than 5.5 $M_{\odot}$ before the 10th TP and before the first TP only for the 8 $M_{\odot}$ model. About the $^{12}C/^{13}C = 9\pm6$ ratio, it can be achieved by masses larger than 5.5 $M_{\odot}$ at the beginning of the TP phase (again around the 10th TP) but the Monash models predict $^{12}C/^{13}C < 15$ before the first TP for 8 $M_{\odot}$ only. Thus, the CNO isotopic composition of IRAS 15152+3632 is consistent with a 8 $M_{\odot}$ progenitor already experiencing strong HBB before the first TP, in good agreement with the Monash predictions. The Li enhancement (together with no Rb and Zr) is also consistent with this interpretation.

IRAS 18072+3100

In the case of IRAS 18072+3100, the star is O-poor, but super N-rich in comparison with the Monash models. The $\log \epsilon(O) = 8.0\pm0.5$ dex and $\log \epsilon(N) > 9.4$ dex abundances are not expected by the theoretical predictions. Neverthe-

less, the more massive models (∼7-8 $M_\odot$) could reach the low C enhancement, log ϵ(C) = 7.3±0.2 dex, in the 12th TP for the 7 $M_\odot$ model or in the 5th TP for the 8 $M_\odot$ progenitor stellar mass, taking into account the uncertainties. Regarding the CNO isotopic ratios, the $^{14}N/^{15}N$ and $^{18}O/^{16}O$ lower and upper limits, respectively, do not give us additional information about the possible progenitor stellar mass, while the $^{17}O/^{16}O = 1.000\times10^{-2}$ ratio, taking into account the uncertainties, is higher than the predictions of the Monash models for all progenitor masses. On the other hand, the $^{12}C/^{13}C = 6\pm4$ ratio, is reached in the 4th TP, $^{12}C/^{13}C = 8.1$, for 7 $M_\odot$ and in the first TP, $^{12}C/^{13}C = 2.6$, for 8 $M_\odot$, respectively. However, the C abundance does not reach our range of values until the 12th and 5th TP in the 7 and 8 the $M_\odot$ models, respectively. Thus, the $^{12}C/^{13}C = 6\pm4$ ratio agrees well with the Monash models: $^{12}C/^{13}C = 2.6$ in the 12th TP for 7 $M_\odot$ and $^{12}C/^{13}C = 2.58$ in the 5th for 8 $M_\odot$ progenitor stellar mass. In summary, the low C abundance and $^{12}C/^{13}C$ in IRAS 18072+3100 suggest a progenitor star around M = 7-8 $M_\odot$ experiencing HBB during the first TPs, which is consistent with the presence of Li without Rb and Zr but the high N, O and $^{17}O/^{16}O$ are not expected by the theoretical predictions.

IRAS 18141+0340

In IRAS 18141+0340, the obtained CNO abundances indicate that this star is O-poor in comparison with the Monash models. Regarding the C abundance, logε(C) = 7.5±0.2 dex, this value could be reached for the larger stellar mass models, logε(C) = 7.73 dex in the 11th TP for 7 $M_\odot$ and logε(C) = 7.74 dex in the 4th TP for 8 $M_\odot$ in the Monash models. In the case of our derived N abundance, logε(N) = 9.6±0.8 dex, agrees taking into account the large uncertainties with 7 $M_\odot$ in the 25th TP, logε(N) = 8.80 dex, and 8 $M_\odot$ in the 27th TP, logε(N) = 8.80 dex, respectively. Thus, the strong N enhancement observed is not predicted in the early TPs, and IRAS 18141+0340 is N-rich in comparison with the predictions in the first TPs. About the CNO isotopic ratios, the $^{14}N/^{15}N$ lower and $^{18}O/^{16}O$ upper limits do not help to limit the stellar mass of IRAS 18141+0340, while the $^{17}O/^{16}O = 3.968\times10^{-3}$ isotopic ratio is in good agreement with the more massive Monash models (M = 7-8 $M_\odot$) because they can reproduce the derived ratio in the 12th TP for 7 $M_\odot$, $^{17}O/^{16}O = 2.911\times10^{-3}$, and in the 4th TP for 8 $M_\odot$, $^{17}O/^{16}O = 3.666\times10^{-3}$, taking into account our uncertainties. Finally, in this star we obtain $^{12}C/^{13}C = 3\pm1$, the lowest C isotopic ratio in our sample stars, and only compatible with the M = 7-8 $M_\odot$ models at the beginning of the TP phase; $^{12}C/^{13}C = 2.6$ in the 12th TP for 7 $M_\odot$ and $^{12}C/^{13}C = 2.5$ in the 4th TP for the 8 $M_\odot$ progenitor

stellar mass. In short, the low C, $^{12}C/^{13}C$ and $^{17}O/^{16}O$ in IRAS 18141+0340 suggest again a progenitor star of M = 7-8 $M_{\odot}$ experiencing HBB during the first TPs, which is consistent with the Li, Rb and Zr information but the high N and low O are not theoretically predicted by the Monash models.

SV Cas

In the star SV Cas, the log ϵ(C) = 7.8±0.2 dex abundance suggests a 7-8 $M_{\odot}$ progenitor stellar mass in good agreement with the values predicted by the Monash models at the beginning of the TP phase, log ϵ(C) = 8.09 dex in the 8th TP for 7 $M_{\odot}$ and log ϵ(C) = 7.91 dex even in the first TP for 8 $M_{\odot}$. The N and O abundances, log ϵ(N) = 9.0±0.8 dex and log ϵ(O) = 8.3±0.7 dex respectively, do not give us additional information about the progenitor stellar mass because all the models reproduce those ranges of abundances even before the first TP. Also, the $^{14}N/^{15}N$ lower and $^{18}O/^{16}O$ upper limits do not give us additional information about the progenitor stellar mass because are compatible with the predictions for all stellar mass models. Regarding the $^{17}O/^{16}O = 1.001\times10^{-3}$ ratio, it agrees well with the M = 7 $M_{\odot}$ nucleosynthesis models in the 8th TP, $^{17}O/^{16}O = 2.178\times10^{-3}$, and 8 $M_{\odot}$ before the first TP, $^{17}O/^{16}O = 2.891\times10^{-3}$, taking into account the uncertainties. The obtained $^{12}C/^{13}C = 6\pm2$ ratio confirms that the progenitor mass of SV Cas is $\sim$ 7-8 $M_{\odot}$ because the Monash models predict $^{12}C/^{13}C = 2.9$ in the 8th TP for 7 $M_{\odot}$ and $^{12}C/^{13}C = 2.6$ for the first TP, values even slightly lower than those obtained by us. The derived CNO elemental/isotopic abundances are thus consistent with a $\sim$7-8 $M_{\odot}$ progenitor star suffering HBB during the very first TPs; being also consistent with the super Li-rich character of SV Cas (log ϵ(Li) = 3.5 dex) and the lack of s-process overabundances.

RU Cyg

Finally, the log ϵ(C) = 8.1 ± 0.3 dex abundance obtained in RU Cyg is in good agreement with all the stellar models, while the derived N abundance, log ϵ(N) = 9.0 ± 0.6 dex, is compatible with the M $\geqslant$ 5 $M_{\odot}$ models in the early TPs (around the 10th TP). However, our O enhancement, log ϵ(O) = 8.4 ± 0.3 dex, only can be reached by the most massive model, M = 8 $M_{\odot}$, in the 10th TP. On the other hand, regarding the isotopic ratios, the range of the $^{17}O/^{16}O$ ratio taking into account the uncertainties, $1.318\times10^{-3} \leqslant {}^{17}O/^{16}O \leqslant 2.882\times10^{-3}$, is only compatible with the 8 $M_{\odot}$ model before the first TP ($^{17}O/^{16}O = 2.891\times10^{-3}$). The CNO abundances, alike the $^{12}C/^{13}C$, $^{14}N/^{15}N$ and $^{18}O/^{16}O$ isotopic ratios are compatible with the Monash predictions for M

Table 4.4: Derived O isotopic ratios for the sample stars in the meteoritic abundance community convention.

IRAS name	$^{17}O/^{16}O$	$^{18}O/^{16}O$
15152+3632	$7.008\times10^{-4} \pm ^{4.230\times10^{-4}}_{2.120\times10^{-4}}$	$<3.003\times10^{-4}$
18072+3100	$1.000\times10^{-2} \pm ^{4.930\times10^{-3}}_{2.481\times10^{-3}}$	$<2.000\times10^{-2}$
18141+0340	$3.968\times10^{-3} \pm ^{3.845\times10^{-3}}_{1.308\times10^{-3}}$	$<1.316\times10^{-2}$
SV Cas	$1.001\times10^{-3} \pm ^{4.300\times10^{-3}}_{2.312\times10^{-4}}$	$<3.004\times10^{-4}$
RU Cyg	$1.808\times10^{-3} \pm ^{1.074\times10^{-3}}_{4.900\times10^{-4}}$	$<2.008\times10^{-3}$

The solar values for $^{16}O/^{17}O$ and $^{16}O/^{18}O$ are 2700 and 498, respectively (Lodders et al. 2009). In the meteoritic abundance convention, the solar values for $^{17}O/^{16}O$ and $^{18}O/^{16}O$ are 3.704×10^{-4} and 2.008×10^{-3}, respectively.

= 8 $M_\odot$ before the first TP. Thus, a progenitor mass of 8 $M_\odot$ before the fiest TP is in good agreement with the Li enrichment together with the lack of Rb and Zr in this star.

In summary, the CNO isotopic ratios in our sample stars are consistent with very massive ($\sim$7-8 $M_\odot$) AGB stars at the beginning of the TP phase. Remarkably, two sample stars (IRAS 15152+3632 and RU Cyg) seem to be the descendants of $\sim$8 $M_\odot$ HBB progenitors that have not experienced any TP, being very good candidates for truly super-AGB stars. Our findings should thus encourage the extension of actual super-AGB nucleosynthesis models (e.g. Doherty et al. 2015, 2017) to the CNO isotopic abundances in such stars.

4.6 Comparison with presolar grains

Finally, we have compared our derived oxygen isotopic ratios with the presolar grain data discussed in Lugaro et al. (2017). In this section, we also adopt the meteoritic abundance community convention in the oxygen isotopic ratios to allow straightforward comparisons with the literature data (see Table 4.4). The presolar grains give us signatures of the nucleosynthesis and mixing processes that occured in the parent stars (Zinner 1998). The O-rich grains (C < O), oxides and silicates, are mainly originated in the winds of AGB stars (Nittler 2009). While the Group I grains are originated in stars of initial masses M

∼1-3 $M_\odot$ and show excesses in ^{17}O, characteristic of the FDU in red giant stars, hypotheses on the site of formation for Group II grains are still tentative (Lugaro et al. 2017).

In Figure 4.17 we plot the isotopic ratios observed for Group I and II stardust grains, together with the oxygen isotopic ratios in our sample stars and the stellar surface evolution of the $^{17}O/^{16}O$ and $^{18}O/^{16}O$ ratios from four AGB nucleosynthesis Monash models (of initial masses between 4.5 and 8 $M_\odot$ at solar metallicity). The predicted evolution of the oxygen isotopic ratios at the stellar surface of the Lugaro et al. (2017) AGB Monash models uses a new $^{17}O(p, \alpha)^{14}N$ rate, which has been determined from the experiments at the Laboratory for Underground Nuclear Astrophysics (LUNA). At temperatures typical of cool bottom processing (CBP; Nollett et al. 2003; Palmerini et al. 2011), 40-55 MK, the new reaction rate reproduces only the lowest $^{17}O/^{16}O$ values observed in Group II grains. In addition, the new LUNA reaction rate, at the typical temperatures for HBB (∼ 60-80 MK), reproduces most of the observed $^{17}O/^{16}O$ range, revealing the signature of HBB in stardust grains (Lugaro et al. 2017). Any massive AGB model experiencing HBB with temperatures in the range 60-80 MK will produce $^{17}O/^{16}O$ ratios in agreement with those observed in most Group II grains (see Figure 2 in Lugaro et al. 2017).

The $^{17}O/^{16}O$ and $^{18}O/^{16}O$ isotopic ratios obtained in IRAS 15152+3632 and SV Cas are clearly compatible with Group II grains (see Figure 4.17); also the values derived for SV Cas from Hinkle et al. (2016). On the other hand, the O isotopic ratios for V1415 Aql from Abia et al. (2017a), RU Cyg from Hinkle et al. (2016) and the values for RU Cyg determined by us are in good agreement with the Group I grains. All these values are compatible with the isotopic evolution of the Lugaro et al. (2017) models for massive AGB stars (M = 4.25-8 $M_\odot$). Regarding IRAS 18072+3100 and IRAS 18141+0340, the high $^{17}O/^{16}O$ and low $^{18}O/^{16}O$ isotopic ratios do not clearly agree with Group I or II grains, although the large $^{17}O/^{16}O$ uncertainties in those stars could be consistent with Group I grains (or even Group II grains). In addition, the lower limits of the $^{18}O/^{16}O$ ratio in those stars are more conservative because the synthetic fits around the 2.3 μm spectral region are worse than in the rest of the sample stars.

These results reinforce the idea that the more massive AGB stars could be the site of formation of the Group II grains; at least this result is clear for the stars IRAS 15152+3632 and SV Cas. Regarding the other sample stars, although the $^{17}O/^{16}O$ ratios from our stars are consistent with Group II grains, the large uncertainties in the $^{17}O/^{16}O$ ratios and our conservative $^{18}O/^{16}O$ lower limits avoid a more solid confirmation of massive AGB stars at the beginning of the TP phase as generally being at the origin of the Group II

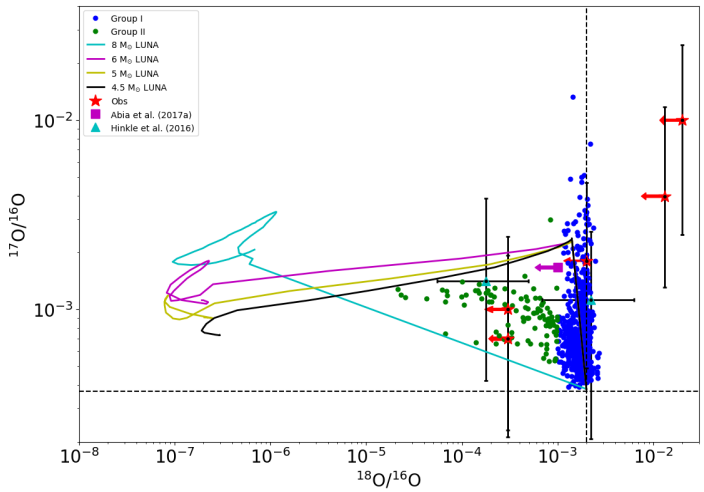

Figure 4.17: Isotopic ratios observed in our sample stars (red stars), Group I (blue dots) and II (green dots) presolar grains, and the evolution of the O isotopic ratios at the stellar surface of AGB Monash models of different masses (solid lines). Moreover, we have plotted the isotopic ratios of SV Cas and RU Cyg (blue triangles), and V1415 Aql (magenta square) derived in Hinkle et al. (2016) and Abia et al. (2017a), respectively. The black dashed lines indicate the values of the solar O isotopic ratios, $^{17}O/^{16}O = 3.704\times10^{-4}$ and $^{18}O/^{16}O = 2.008\times10^{-3}$.

grains.

It is to be noted here that with the new ^{17}O(p, α)^{14}N reaction rate from LUNA, most predictions for ^{17}O/^{16}O from the Karakas & Lugaro (2016) Monash models are expected to be a factor of roughly 2 lower (Lugaro et al. 2017). Although this does not affect our main conclusions, a full detailed exploration of the AGB (and even super-AGB) model predictions using the new ^{17}O(p, α)^{14}N LUNA reaction rate would be desirable; e.g. in order to explore if the ^{17}O/^{16}O ratios stays lower for a longer time and if this may affect the production and destruction of other elements such as Li.

5

Conclusions

We summarize here the main findings of the thesis.

5.1 Rb and Zr circumstellar abundances in massive AGB Galactic AGB stars

We have reported new Rb and Zr abundances from the 7800 Å Rb I line and the 6474 Å ZrO bandhead, respectively, in a sample of massive Galactic AGB stars, previously studied with hydrostatic models, using more realistic extended atmosphere models and a modified version of the spectral synthesis code Turbospectrum, which considers the presence of a circumstellar envelope with a radial wind. The Rb abundances are much lower (in some cases even 1-2 dex) with the pseudo-dynamical models, while the Zr abundances are close to the hydrostatic ones because the 6474 Å ZrO bandhead is formed deeper in the atmosphere and is less affected than the 7800 Å Rb I resonant line by the circumstellar effects.

We have studied the sensitivity of the determined abundances to variations in the stellar (T_{eff}) and wind ($\dot{M}$, β and v_{exp}) parameters. The Rb abundances are very sensitive to the $\dot{M}$ but much less to the β parameter and v_{exp}(OH). The Zr abundances, instead, are not affected by variations of the stellar and wind parameters. The Rb abundances from extended models are lower than those obtained from the hydrostatic ones, and the difference is larger in the stars with the highest Rb abundances in the hydrostatic case. We have represented the hydrostatic and pseudo-dynamical Rb abundances against the v_{exp}(OH), which can be used as a mass indicator independent of the distance, and we

have observed a flatter correlation. The difference between the hydrostatic and pseudo-dynamical Rb abundances increases with increasing the v_{exp}(OH), due to the fact that the presence of a circumstellar envelope affects more strongly the more massive stars. Furthermore, the dispersion of the correlation between the Rb abundance and v_{exp}(OH) is larger in the pseudo-dynamical case. When we fix the wind parameters $\dot{M}$ (i.e. equivalent to assuming that our AGB sample stars have a similar evolutionary stage in terms of mass loss), and/or β (the same velocity profile), the dispersion is lower.

The Monash predictions reproduce the range of new Rb and Zr abundances although [Rb/Fe] values above 1.0 can only be matched if the superwind is delayed to after the period reaches 700-800 days. Moreover, the rate of the ^{22}Ne$(\alpha, n)^{25}$Mg reaction is crucial, but still hampered by large systematic uncertainties. The FRUITY massive AGB models predict Rb abundances much lower than observed and negative [Rb/Zr] ratios, at odds with the observations. The NuGrid/MESA models of 4 and 5 $M_{\odot}$ predict [Rb/Fe] as high as 0.9 dex, however, the 4 $M_{\odot}$ model does not experience HBB and becomes C-rich, while our sample stars are clearly O-rich. The maximum observed [Rb/Zr] ratios are still more than a factor of two larger than predicted by the nucleosynthesis models. A possible explanation for this difference between the observations and the predictions is that Zr could be depleted into dust. Observations of other *s*-process elements belonging to the same first peak as Rb and Zr, and with condensation temperature lower than the Zr one, will help to clarify this mismatch.

In summary, the [Rb/Fe] abundances and [Rb/Zr] ratios previously derived with hydrostatic models are certainly not predicted by the most recent theoretical models of AGB nucleosynthesis. The new [Rb/Fe] abundances and [Rb/Zr] ratios as obtained from our pseudo-dynamical model atmospheres are much lower in much better agreement with the theoretical predictions, significantly resolving the mismatch between the observations and the nucleosynthesis models in the more massive AGB stars. This confirms the earlier Zamora et al. preliminary results on a smaller sample of massive O-rich AGB stars but here we find that the Rb abundances are strongly dependent on the wind mass-loss $\dot{M}$, which is basically unknown in our AGB star sample. Follow-up radio observations (e.g. the rotational lines of the several CO isotopologues) of these massive Galactic AGB stars are encouraged in order to obtain precise mass-loss rate estimates needed to break the actual models degeneracy and obtain more reliable (non-model-dependent) Rb abundances in massive AGB stars.

5.2 Circumstellar effects on the Li and Ca abundances in massive Galactic AGB stars

We have reported new hydrostatic and pseudo-dynamical abundances of Li and Ca from the 6708 Å Li I and 6463 Å Ca I lines, respectively, in a sample of massive Galactic O-rich AGB stars by using a modified version of the spectral synthesis code *Turbospectrum*, which considers the presence of a circumstellar envelope with a radial wind. The new Li abundances from extended atmosphere models are very similar to those obtained from the hydrostatic models (the average difference is 0.18 dex), while they are identical for Ca. This indicates that the determination of the Li and Ca abundances in massive O-rich AGB stars is not strongly affected by the presence of a circumstellar envelope. Indeed, we found that the Li I and Ca I line profiles are not very sensitive to variations of the wind ($\dot{M}$, β and v_{exp}(OH)) parameters.

The new pseudo-dynamic abundances of Li confirm the Li-rich (and super Li-rich in some stars) character of our sample stars and the strong activation of the HBB process in massive Galactic AGB stars. This is in good agreement with the theoretical predictions from the most recent AGB nucleosynthesis models such as ATON, Monash and NuGrid/MESA, but at odds with the FRUITY database, which predicts no Li production by HBB in massive AGB stars at solar metallicity.

For the first time we have obtained Ca abundances in a sample of massive Galactic AGB stars. Most of them (67%) display nearly solar Ca abundances; within the estimated errors and/or considering possible NLTE effects. Their abundances are thus consistent with the predictions from the *s*-process nucleosynthesis models for massive AGB stars at solar metallicity. For example, such models predict some production of the radioactive ^{41}Ca isotope but no change in the total Ca abundance. A minority of stars (five) show a significant Ca depletion (by $\sim$ -0.8 $-$ -1.0 dex). Possible explanations to explain their apparent and unexpected Ca depletion could be missed opacities in the stellar atmosphere models and/or Ca depletion into dust as well as line weakening phenomena.

5.3 CNO abundances and isotopic ratios in massive AGB stars

We have obtained for the first time, by spectral synthesis, the CNO elemental abundances and isotopic ratios in a small sample (5) of massive Galactic O-rich AGB stars at the beginning of the TP phase. In addition, we have explored the effects of the presence of a circumstellar envelope and radial wind in the CNO abundances and isotopic ratios. We have found that the abundances derived

with hydrostatic models are identical to those obtained with extended model atmospheres. The very large N enhancements in our sample stars confirm, independently of the Li overabundances, the activation of the HBB process in massive AGB stars at solar metallicity.

The derived CNO abundances and isotopic ratios, $^{12}C/^{13}C$, $^{16}O/^{17}O$, $^{16}O/^{18}O$ and $^{14}N/^{15}N$, are in general good agreement with the nucleosynthesis theoretical predictions for very massive AGB stars (in the range 7-8 $M_{\odot}$), at solar metallicity, that experience HBB in the early TPs. In particular, the obtained $^{12}C/^{13}C$ ratios also confirm the HBB activation in massive AGB stars in a more precise way that from the N and Li abundances because this isotopic ratio is more independent of variations in the stellar parameters (T_{eff}, log g, etc.) used in the modelling of the observed spectra. However, we note that for the $^{16}O/^{18}O$ and $^{14}N/^{15}N$ isotopic ratios, we only could estimate rough lower limits because: i) the synthetic spectra are less sensitive to changes of these isotopic ratios; ii) the high density of molecular lines in the observed spectra; and iii) the difficulty to find clean (not blended) molecular lines in massive AGB stellar spectra.

Moreover, two sample AGB stars (IRAS 15152+3632 and RU Cyg) seem to be the descendants of $\sim$8 $M_{\odot}$ HBB progenitors that have experienced any TP. They thus represent very good candidates for truly super-AGB stars. This finding should encourage more super-AGB nucleosynthesis calculations.

Finally, we have compared our O isotopic ratios with the measurements made on presolar grains. Our results for the AGB stars IRAS 15152+3632 and SV Cas reinforce the idea that the more massive AGB stars could be the formation site of the Group II grains. However, the large uncertainties in the $^{17}O/^{16}O$ ratios and our conservative $^{18}O/^{16}O$ lower limits for the rest of AGB stars in our sample do not permit us to reach a definitive answer about the the origin of the Group II stardust grains. Our findings should encourage the nucleosynthesis modelers to carry out a full detailed exploration of the massive AGB (and even super-AGB) model predictions using the new $^{17}O(p, \alpha)^{14}N$ reaction rate from the LUNA experiment.

6

Future work

As a natural continuation of the work presented in this thesis, new research directions have emerged. Some of them are enumerated below.

- Regarding the study of the circumstellar effects, it will be very useful to use the pseudo-dynamic models in other types of stars with thick circumstellar envelopes (e.g. C-rich AGB and red supergiant stars) in order to explore the circumstellar effects as a function of other stellar parameters such as the chemical composition as well as to investigate the circumstellar effects on other atoms and molecules from the optical to the IR range.
- We plan to keep improving the abundance determination in massive AGB stars and understand better the real effects of the HBB in these stars. Particularly, the extension to more evolved and extreme massive AGB stars, whose present modelling show some challenging problems. Indeed, the development of more realistic model atmospheres and synthetic spectra for the more evolved and extreme massive AGB stars would be highly desirable. The first step would be the inclusion of dust (which should be more important in the IR) in the models, while a long-term goal would be the natural extension to fully 3D hydrodynamical models.
- Concerning the CNO elemental/isotopic abundances, we would like to compare our results with new massive AGB (even super-AGB) model predictions, when available, that consider the new $^{17}O(p, \alpha)^{14}N$ reaction rate from the LUNA experiment in order to confirm/discard if the massive

AGB stars are the main site of the origin of the Group II grains. About the two stars (IRAS 15152+3632 and RU Cyg) that are good candidates for being super-AGB stars, more detailed (e.g. including the CNO isotopes) super-AGB models could elucidate if they are truly super-AGB stars; something that would represent the first detection of a super-AGB star.

- Observationally, we could study the CNO chemical composition by using several high-resolution spectroscopic facilities in the near-IR. For example, using data on well known massive AGB stars already available in our IAC group (i.e. VLT/ISAAC, VLT/CRIRES and TNG/GIANO). Also, the analysis of large AGB samples will be possible with the Sloan-III/APOGEE data, while the Sloan-IV/APOGEE-2 ones would provide us access to other metallicities like the Galactic Bulge and the Magellanic Clouds. Undoubtedly, this would provide strong observational constraints to the nucleosynthesis models and an unique database for the meteoritic community.

Bibliography

Abia, C., Busso, M., Gallino, R., et al. 2001, ApJ, 559, 1117

Abia, C., Hedrosa, R. P., Domínguez, I., & Straniero, O. 2017b, A&A, 599, A39

Abia, C., Pavlenko, Y., & de Laverny, P. 1999, A&A, 351, 273

Abia, C., Straniero, O., & Ventura, P. 2017a, Mem. Soc. Astron. Italiana, 88, 360

Alavi, S. F., & Shayesteh, A. 2018, MNRAS, 474, 2

Alvarez, R., & Plez, B. 1998, A&A, 330, 1109

Angulo, C., Arnould, M., Rayet, M., et al. 1999, Nucl. Phys. A, 656, 3

Asplund, M., Grevesse, N., Sauval, A. J., & Scott, P. 2009, ARA&A, 47, 481

Barber, R. J., Tennyson, J., Harris, G. J., & Tolchenov, R. N. 2006, MNRAS, 368, 1087

Becker, S. A., & Iben, I., J. 1979, ApJ, 232, 831

—. 1980, ApJ, 237, 111

Beer, H., & Macklin, R. L. 1989, ApJ, 339, 962

Bertelli, G., Bressan, A., Chiosi, C., & Angerer, K. 1986, A&AS, 66, 191

Bloecker, T. 1995, A&A, 297, 727

Böhm-Vitense, E. 1958, Zeitschrift fur Astrophysik, 46, 108

Brooke, J. S. A., Bernath, P. F., Western, C. M., et al. 2016, J. Quant. Spec. Radiat. Transf., 168, 142

Busso, M., Gallino, R., Lambert, D. L., Travaglio, C., & Smith, V. V. 2001, ApJ, 557, 802

Busso, M., Gallino, R., & Wasserburg, G. J. 1999, ARA&A, 37, 239

Cameron, A. G. W. 1960, AJ, 65, 485

Cameron, A. G. W., & Fowler, W. A. 1971, ApJ, 164, 111

Carlsson, M. 1986, Uppsala Astronomical Observatory Reports, 33

Carlsson, M. 1992, in Astronomical Society of the Pacific Conference Series, Vol. 26, Cool Stars, Stellar Systems, and the Sun, ed. M. S. Giampapa & J. A. Bookbinder, 499

Chengalur, J. N., Lewis, B. M., Eder, J., & Terzian, Y. 1993, ApJS, 89, 189

Cristallo, S., Straniero, O., Piersanti, L., & Gobrecht, D. 2015, ApJS, 219, 40

Danilovich, T., Lombaert, R., Decin, L., et al. 2017, A&A, 602, A14

Danilovich, T., Teyssier, D., Justtanont, K., et al. 2015, A&A, 581, A60

De Beck, E., Decin, L., de Koter, A., et al. 2010, A&A, 523, A18

De Nutte, R., Decin, L., Olofsson, H., et al. 2017, A&A, 600, A71

Dearborn, D. S. P. 1992, Phys. Rep., 210, 367

Decin, L., Justtanont, K., De Beck, E., et al. 2010, A&A, 521, L4

Dell'Agli, F., García-Hernández, D. A., Rossi, C., et al. 2014, MNRAS, 441, 1115

Di Criscienzo, M., Ventura, P., García-Hernández, D. A., et al. 2016, MNRAS, 462, 395

Dillmann, I., Domingo-Pardo, C., Heil, M., et al. 2009, Phys. Rev. C, 79, 065805

Doherty, C. L., Gil-Pons, P., Siess, L., & Lattanzio, J. C. 2017, PASA, 34, e056

Doherty, C. L., Gil-Pons, P., Siess, L., Lattanzio, J. C., & Lau, H. H. B. 2015, MNRAS, 446, 2599

Doherty, C. L., Lugaro, M., Lau, H., et al. 2012, Meteoritics and Planetary Science Supplement, 75, 5159

Dominy, J. F., & Wallerstein, G. 1987, ApJ, 317, 810

Eriksson, K., Nowotny, W., Höfner, S., Aringer, B., & Wachter, A. 2014, A&A, 566, A95

Fishlock, C. K., Karakas, A. I., Lugaro, M., & Yong, D. 2014, ApJ, 797, 44

Frost, C. A., & Lattanzio, J. C. 1996, ApJ, 473, 383

Gail, H. P., Zhukovska, S. V., Hoppe, P., & Trieloff, M. 2009, ApJ, 698, 1136

Gallino, R., Arlandini, C., Busso, M., et al. 1998, ApJ, 497, 388

García-Hernández, D. A., García-Lario, P., Plez, B., et al. 2006, Science, 314, 1751

—. 2007a, A&A, 462, 711

García-Hernández, D. A., Hinkle, K. H., Lambert, D. L., & Eriksson, K. 2009b, ApJ, 696, 1733

García-Hernández, D. A., Perea-Calderón, J. V., Bobrowsky, M., & García-Lario, P. 2007b, ApJ, 666, L33

García-Hernández, D. A., Zamora, O., Yagüe, A., et al. 2013, A&A, 555, L3

García-Hernández, D. A., Manchado, A., Lambert, D. L., et al. 2009a, ApJ, 705, L31

García-Rojas, J., Peña, M., Flores-Durán, S., & Hernández-Martínez, L. 2016, A&A, 586, A59

Gehrz, R. D. 1998, in Astronomical Society of the Pacific Conference Series, Vol. 137, Wild Stars in the Old West, ed. S. Howell, E. Kuulkers, & C. Woodward, 146

Gordon, I. E., Rothman, L. S., Tan, Y., Kochanov, R. V., & Hill, C. 2017, in 72nd International Symposium on Molecular Spectroscopy, TJ08

Goriely, S., & Siess, L. 2004, A&A, 421, L25

Grevesse, N., Asplund, M., & Sauval, A. J. 2007, Space Sci. Rev., 130, 105

Grevesse, N., & Sauval, A. J. 1998, Space Sci. Rev., 85, 161

Groenewegen, M. A. T., & de Jong, T. 1998, A&A, 337, 797

Gustafsson, B., Edvardsson, B., Eriksson, K., et al. 2008, A&A, 486, 951

Herwig, F. 2000, A&A, 360, 952

—. 2005, ARA&A, 43, 435

Hinkle, K. H., Lebzelter, T., & Straniero, O. 2016, ApJ, 825, 38

Höfner, S., Bladh, S., Aringer, B., & Ahuja, R. 2016, A&A, 594, A108

Höfner, S., & Olofsson, H. 2018, A&A Rev., 26, 1

Hoppe, P., & Ott, U. 1997, in American Institute of Physics Conference Series, ed. T. J. Bernatowicz & E. Zinner, Vol. 402, 27–58

Humphreys, R. M. 1974, ApJ, 188, 75

Iben, I., J., & Renzini, A. 1982a, ApJ, 263, L23

—. 1982b, ApJ, 259, L79

—. 1983, ARA&A, 21, 271

Iliadis, C., Longland, R., Champagne, A. E., & Coc, A. 2010, Nucl. Phys. A, 841, 323

Jiménez-Esteban, F. M., García-Lario, P., Engels, D., & Manchado, A. 2006, A&A, 458, 533

Jones, T. J., Bryja, C. O., Gehrz, R. D., et al. 1990, ApJS, 74, 785

Jönsson, H., Ryde, N., Harper, G. M., et al. 2014, A&A, 564, A122

Jorissen, A., Frayer, D. T., Johnson, H. R., Mayor, M., & Smith, V. V. 1993, A&A, 271, 463

Jura, M., & Kleinmann, S. G. 1989, ApJ, 341, 359

—. 1992, ApJS, 79, 105

Justtanont, K., Teyssier, D., Barlow, M. J., et al. 2013, A&A, 556, A101

Justtanont, K., Barlow, M. J., Blommaert, J., et al. 2015, A&A, 578, A115

Karakas, A., & Lattanzio, J. C. 2007, PASA, 24, 103

Karakas, A. I. 2014, MNRAS, 445, 347

Karakas, A. I., García-Hernández, D. A., & Lugaro, M. 2012, ApJ, 751, 8

Karakas, A. I., & Lattanzio, J. C. 2014, PASA, 31, e030

Karakas, A. I., & Lugaro, M. 2016, ApJ, 825, 26

Karakas, A. I., Lugaro, M., & Gallino, R. 2007, ApJ, 656, L73

Karakas, A. I., Lugaro, M. A., Wiescher, M., Görres, J., & Ugalde, C. 2006, ApJ, 643, 471

Karakas, A. I., van Raai, M. A., Lugaro, M., Sterling, N. C., & Dinerstein, H. L. 2009, ApJ, 690, 1130

Kholopov, P. N., Samus, N. N., Frolov, M. S., et al. 1998, Combined General Catalogue of Variable Stars, 0

Kiselman, D., & Plez, B. 1995, Mem. Soc. Astron. Italiana, 66, 429

Korobkin, O., Rosswog, S., Arcones, A., & Winteler, C. 2012, MNRAS, 426, 1940

Lambert, D. L. 1981, in Astrophysics and Space Science Library, Vol. 88, Physical Processes in Red Giants, ed. J. Iben, I. & A. Renzini, 115–134

Lambert, D. L., Smith, V. V., Busso, M., Gallino, R., & Straniero, O. 1995, ApJ, 450, 302

Lattanzio, J. C. 1986, ApJ, 311, 708

Leisy, P., & Dennefeld, M. 1996, A&AS, 116, 95

Lewis, B. M. 1994, ApJS, 93, 549

Lockwood, G. W. 1985, ApJS, 58, 167

Lodders, K., & Fegley, B., J. 1999, in IAU Symposium, Vol. 191, Asymptotic Giant Branch Stars, ed. T. Le Bertre, A. Lebre, & C. Waelkens, 279

Lodders, K., Palme, H., & Gail, H. P. 2009, Landolt Börnstein, 4B, 712

Lugaro, M., & Chieffi, A. 2011, Radioactivites in Low- and Intermediate-Mass Stars, ed. R. Diehl, D. H. Hartmann, & N. Prantzos, Vol. 812, 83–152

Lugaro, M., Karakas, A. I., Stancliffe, R. J., & Rijs, C. 2012, ApJ, 747, 2

Lugaro, M., Ott, U., & Kereszturi, Á. 2018, Progress in Particle and Nuclear Physics, 102, 1

Lugaro, M., Tagliente, G., Karakas, A. I., et al. 2014, ApJ, 780, 95

Lugaro, M., Karakas, A. I., Bruno, C. G., et al. 2017, Nature Astronomy, 1, 0027

Mazzitelli, I., D'Antona, F., & Ventura, P. 1999, A&A, 348, 846

McKemmish, L. K., Masseron, T., Hoeijmakers, H. J., et al. 2019, MNRAS, 488, 2836

McSaveney, J. A., Wood, P. R., Scholz, M., Lattanzio, J. C., & Hinkle, K. H. 2007, MNRAS, 378, 1089

Menzies, J. W., Whitelock, P. A., & Feast, M. W. 2015, MNRAS, 452, 910

Messenger, S., Keller, L. P., & Lauretta, D. S. 2005, Science, 309, 737

Miller Bertolami, M. M. 2016, A&A, 588, A25

Mowlavi, N. 1999, A&A, 344, 617

Mowlavi, N. 2002, in IAU Symposium, Vol. 187, Cosmic Chemical Evolution, ed. K. Nomoto & J. W. Truran, 57–69

Nguyen, A. N., & Zinner, E. 2004, Science, 303, 1496

Nittler, L. R. 2009, PASA, 26, 271

Nittler, L. R., Alexander, C. M. O., Gallino, R., et al. 2008, ApJ, 682, 1450

Nittler, L. R., Alexander, O., Gao, X., Walker, R. M., & Zinner, E. 1997, ApJ, 483, 475

Nittler, L. R., & Cowsik, R. 1997, Phys. Rev. Lett., 78, 175

Nollett, K. M., Busso, M., & Wasserburg, G. J. 2003, ApJ, 582, 1036

Nordlund, A. 1984, Iterative solution of radiative transfer problems with spherical symmetry using a single-ray approximation., 211–233

Nowotny, W., Höfner, S., & Aringer, B. 2010, A&A, 514, A35

Osorio, Y., & Barklem, P. S. 2016, A&A, 586, A120

Osorio, Y., Barklem, P. S., Lind, K., & Asplund, M. 2011, A&A, 529, A31

Osorio, Y., Lind, K., Barklem, P. S., Allende Prieto, C., & Zatsarinny, O. 2019, A&A, 623, A103

Palmerini, S., La Cognata, M., Cristallo, S., & Busso, M. 2011, ApJ, 729, 3

Pérez-Mesa, V., Zamora, O., García-Hernández, D. A., et al. 2019, A&A, 623, A151

Pignatari, M., Herwig, F., Hirschi, R., et al. 2016, ApJS, 225, 24

Plez, B. 1990, Mem. Soc. Astron. Italiana, 61, 765

—. 2012, Turbospectrum: Code for spectral synthesis, ascl:1205.004

Plez, B., Smith, V. V., & Lambert, D. L. 1993, ApJ, 418, 812

Richards, J. W., Starr, D. L., Miller, A. A., et al. 2012, ApJS, 203, 32

Ritter, C., Herwig, F., Jones, S., et al. 2018, MNRAS, 480, 538

Sackmann, I. J., & Boothroyd, A. I. 1992, ApJ, 392, L71

Samus', N. N., Kazarovets, E. V., Durlevich, O. V., Kireeva, N. N., & Pastukhova, E. N. 2017, Astronomy Reports, 61, 80

Schwarzschild, M., & Härm, R. 1965, ApJ, 142, 855

Sevenster, M. N., Chapman, J. M., Habing, H. J., Killeen, N. E. B., & Lindqvist, M. 1997, A&AS, 122, 79

Shayesteh, A., Ram, R. S., & Bernath, P. F. 2013, Journal of Molecular Spectroscopy, 288, 46

Sivagnanam, P., Le Squeren, A. M., Foy, F., & Tran Minh, F. 1989, A&A, 211, 341

Slootmaker, A., Habing, H. J., & Herman, J. 1985, A&AS, 59, 465

Smith, V. V., Plez, B., Lambert, D. L., & Lubowich, D. A. 1995, ApJ, 441, 735

Smith, V. V., Cunha, K., Shetrone, M. D., et al. 2013, ApJ, 765, 16

Sneden, C., Lucatello, S., Ram, R. S., Brooke, J. S. A., & Bernath, P. 2014, ApJS, 214, 26

Souto, D., Cunha, K., Smith, V., et al. 2016, ApJ, 830, 35

Speck, A. K., Barlow, M. J., Sylvester, R. J., & Hofmeister, A. M. 2000, A&AS, 146, 437

Stanghellini, L., Guerrero, M. A., Cunha, K., Manchado, A., & Villaver, E. 2006, ApJ, 651, 898

Straniero, O., Gallino, R., Busso, M., et al. 1995, ApJ, 440, L85

Straniero, O., Gallino, R., & Cristallo, S. 2006, Nucl. Phys. A, 777, 311

Surman, R., McLaughlin, G. C., Ruffert, M., Janka, H. T., & Hix, W. R. 2008, ApJ, 679, L117

te Lintel Hekkert, P., Caswell, J. L., Habing, H. J., et al. 1991, A&AS, 90, 327

te Lintel Hekkert, P., Versteege-Hensel, H. A., Habing, H. J., & Wiertz, M. 1989, A&AS, 78, 399

Tielens, A. G. G. M. 1990, in From Miras to Planetary Nebulae: Which Path for Stellar Evolution?, ed. M. O. Mennessier & A. Omont, 186

Trigo-Rodríguez, J. M., García-Hernández, D. A., Lugaro, M., et al. 2009, Meteoritics and Planetary Science, 44, 627

van Raai, M. A., Lugaro, M., Karakas, A. I., García-Hernández, D. A., & Yong, D. 2012, A&A, 540, A44

Vassiliadis, E., & Wood, P. R. 1993, ApJ, 413, 641

Ventura, P., & D'Antona, F. 2009, A&A, 499, 835

Ventura, P., Karakas, A., Dell'Agli, F., García-Hernández, D. A., & Guzman-Ramirez, L. 2018, MNRAS, 475, 2282

Vollmer, C., Hoppe, P., & Brenker, F. E. 2008, ApJ, 684, 611

Vollmer, C., Hoppe, P., Stadermann, F. J., Floss, C., & Brenker, F. E. 2009, Geochim. Cosmochim. Acta, 73, 7127

Wallerstein, G., & Knapp, G. R. 1998, ARA&A, 36, 369

Wasserburg, G. J., Trippella, O., & Busso, M. 2015, ApJ, 805, 7

Watson, C. L., Henden, A. A., & Price, A. 2006, Society for Astronomical Sciences Annual Symposium, 25, 47

Whitelock, P., Menzies, J., Feast, M., et al. 1994, MNRAS, 267, 711

Winteler, C., Käppeli, R., Perego, A., et al. 2012, ApJ, 750, L22

Woźniak, P. R., Williams, S. J., Vestrand, W. T., & Gupta, V. 2004, AJ, 128, 2965

Yurchenko, S. N., Blissett, A., Asari, U., et al. 2016, MNRAS, 456, 4524

Yurchenko, S. N., Szabó, I., Pyatenko, E., & Tennyson, J. 2018, MNRAS, 480, 3397

Zamora, O., García-Hernández, D. A., Plez, B., & Manchado, A. 2014, A&A, 564, L4

Zhukovska, S., Petrov, M., & Henning, T. 2015, ApJ, 810, 128

Zinner, E. 1998, Annual Review of Earth and Planetary Sciences, 26, 147

Zinner, E., Nittler, L. R., Hoppe, P., et al. 2005, Geochim. Cosmochim. Acta, 69, 4149

A

Rubidium and zirconium fits

We present here the oberved spectra (black dots), best hydrostatic (blue lines) and pseudo-dynamical (red lines) fits of our sample of massive AGB stars in the regions 7800 Å Rb I line and 6474 Å ZrO bandhead. The parameters of the best fit model atmospheres are indicated in Table 2.4. The flux units are arbitrary. The plots are displayed in increasing R.A. order.

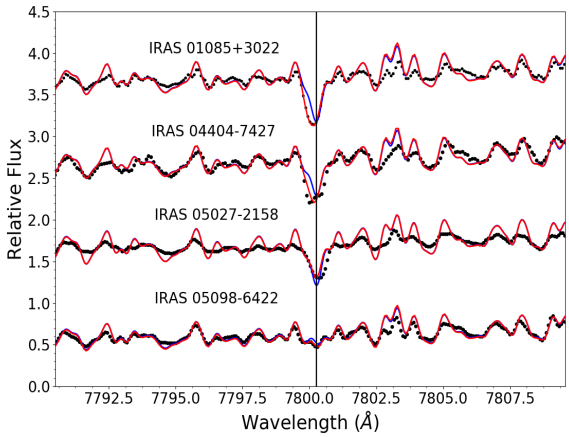

Figure A.1

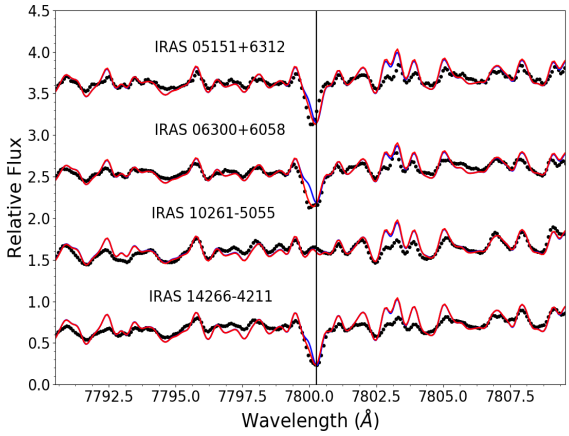

Figure A.2

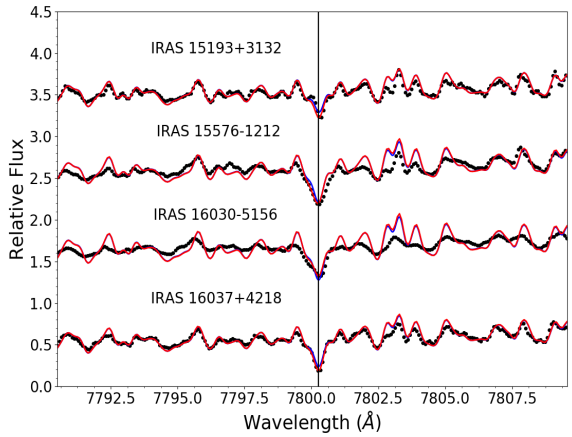

Figure A.3

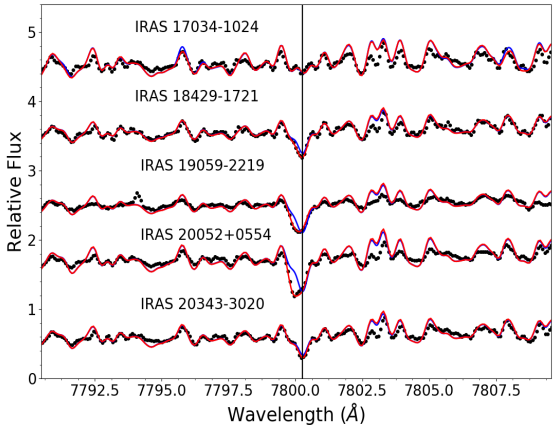

Figure A.4

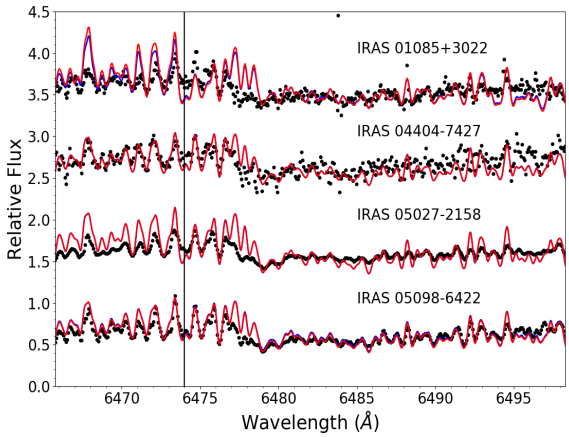

Figure A.5

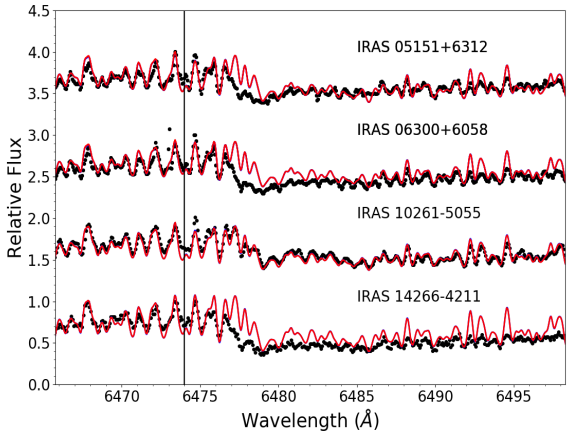

Figure A.6

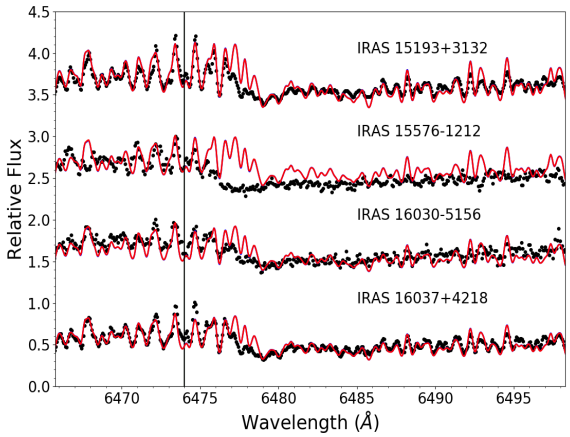

Figure A.7

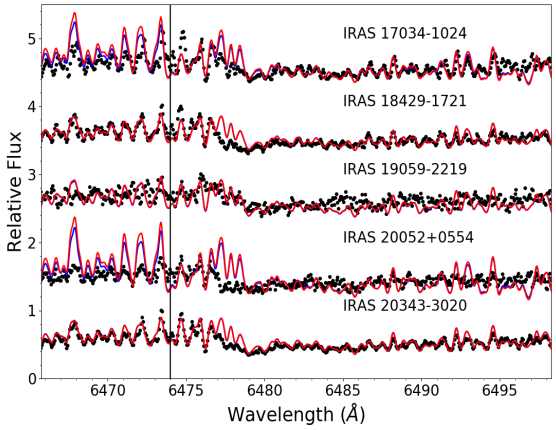

Figure A.8

B

Lithium and calcium fits

We present here the best fits of the 6708 Å Li I and 6463 Å Ca I spectral regions of our sample of massive AGB stars (black dots). The pseudo-dynamical (red lines) models are similar to the hydrostatic (blue lines) ones, and properly repodruce the Li and Ca regions, which means that the Li and Ca line profiles are not strongly affected by the presence of a circumstellar envelope and a radial wind. The parameters of the best fit model atmospheres are indicated in Table 3.3. The flux units are arbitrary. The plots are displayed in increasing R.A. order.

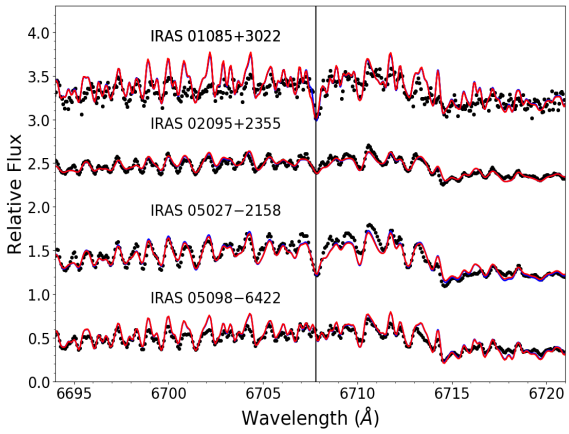

Figure B.1

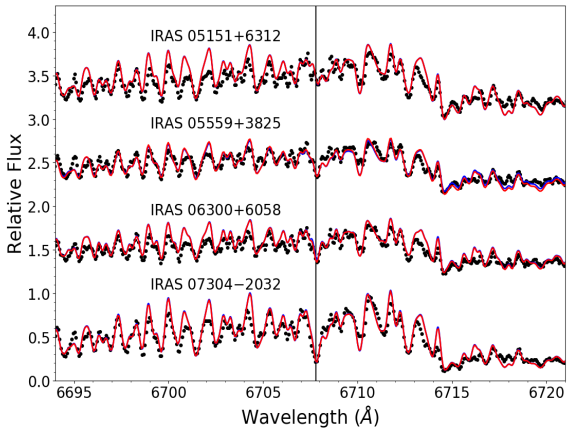

Figure B.2

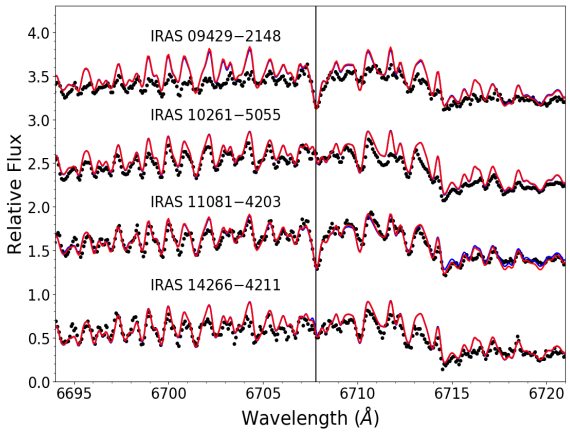

Figure B.3

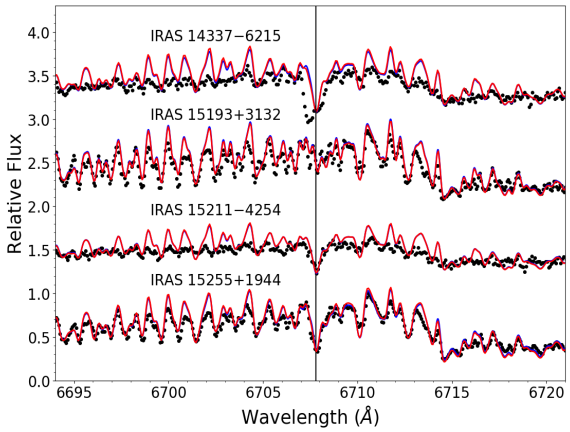

Figure B.4

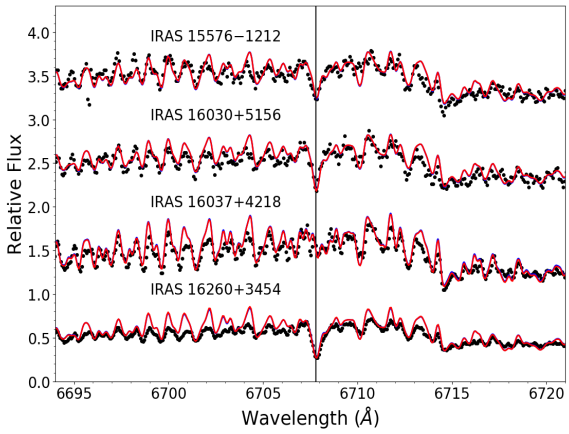

Figure B.5

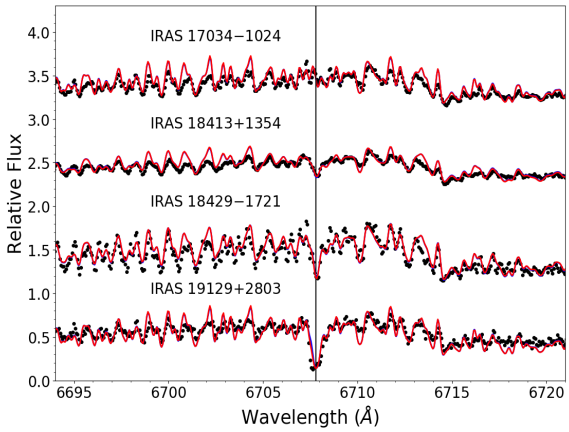

Figure B.6

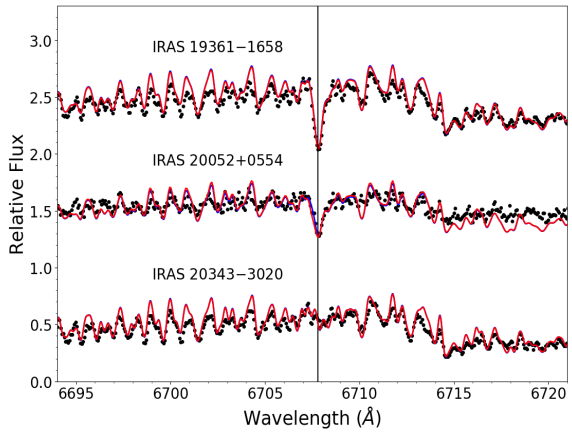

Figure B.7

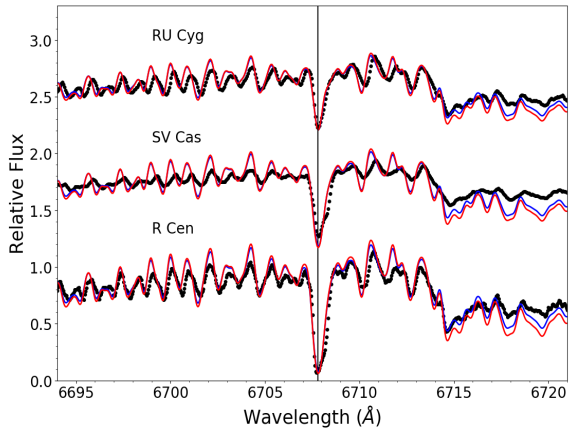

Figure B.8

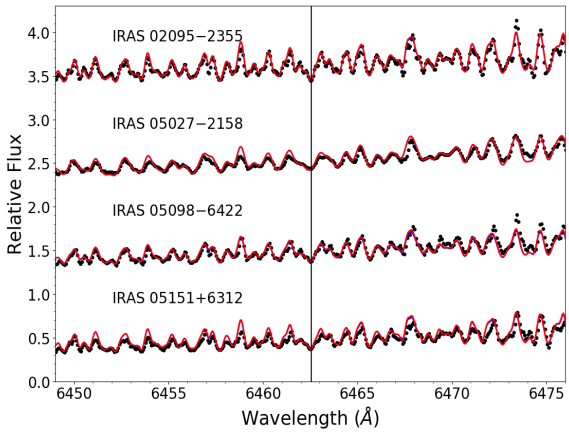

Figure B.9

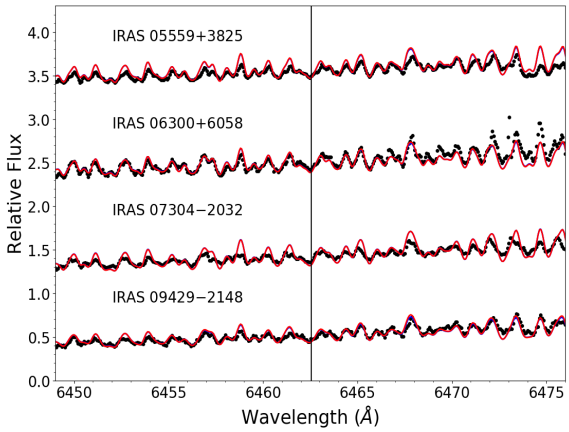

Figure B.10

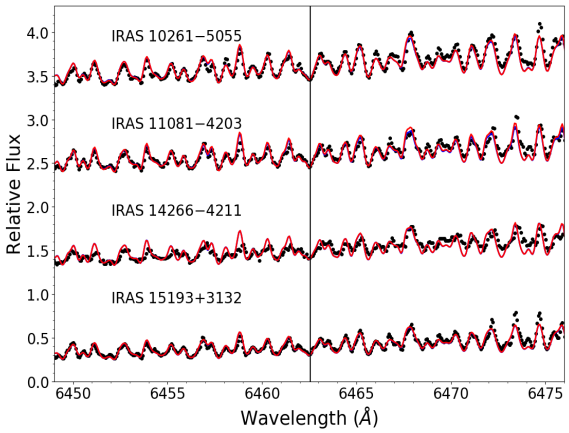

Figure B.11

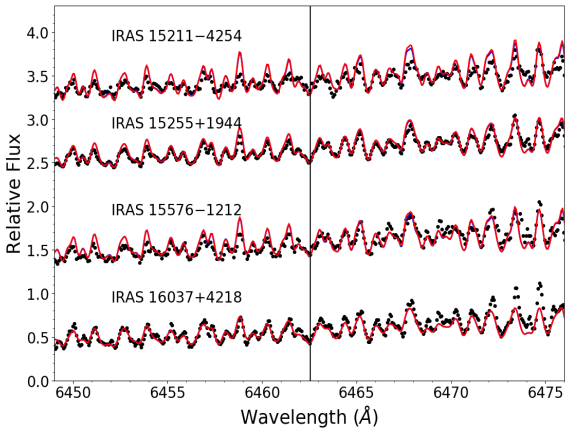

Figure B.12

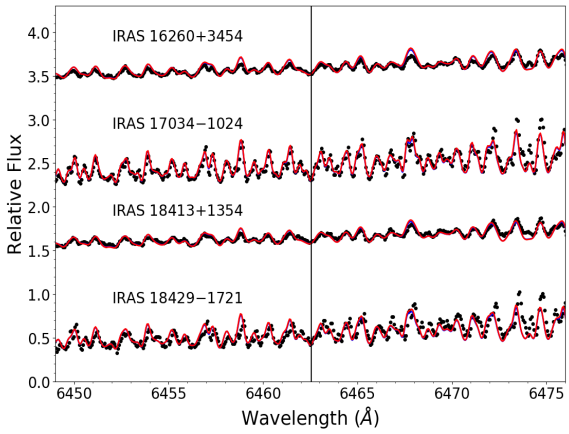

Figure B.13

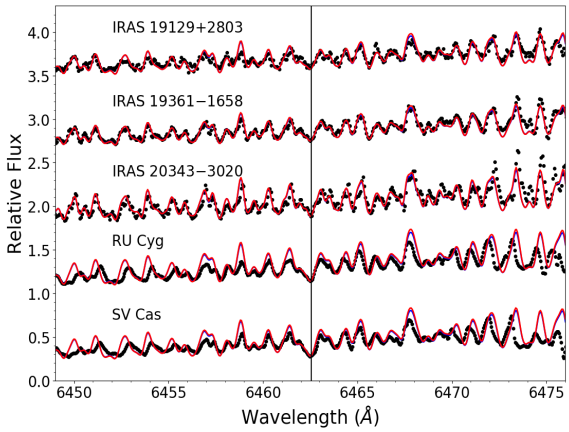

Figure B.14

C

Compasison between theoretical and derived CNO elemental/isotopic abundances

We present here the range of CNO elemental abundances and isotopic ratios, taking into account the uncertainties, of our small sample of massive AGB stars at the beginning of the TP phase in comparison with the Monash theoretical predictions in the TP-AGB phase for massive AGB stars at solar metallicity (Z = 0.014). We note that in the M = 4.25 $_{\odot}$ case, the Karakas & Lugaro (2016) models assume $M_{mix} = 10^{-4}$ $M_{\odot}$. The values of the derived CNO elemental/isotopic abundances are listed in Tables 4.2 and 4.4.

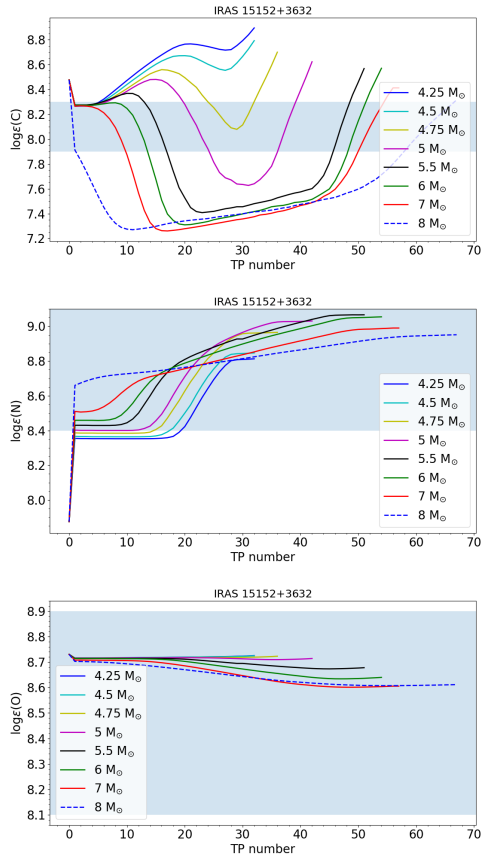

Figure C.1: Theoretical Monash predictions for the C (*top panel*), N (*middle panel*) and O (*bottom panel*) elemental abundances against TP number for the progenitor masses that experience HBB at solar metallicity. The shaded regions indicate the range of CNO abundances of IRAS 15152+3632 taking into account the uncertainties.

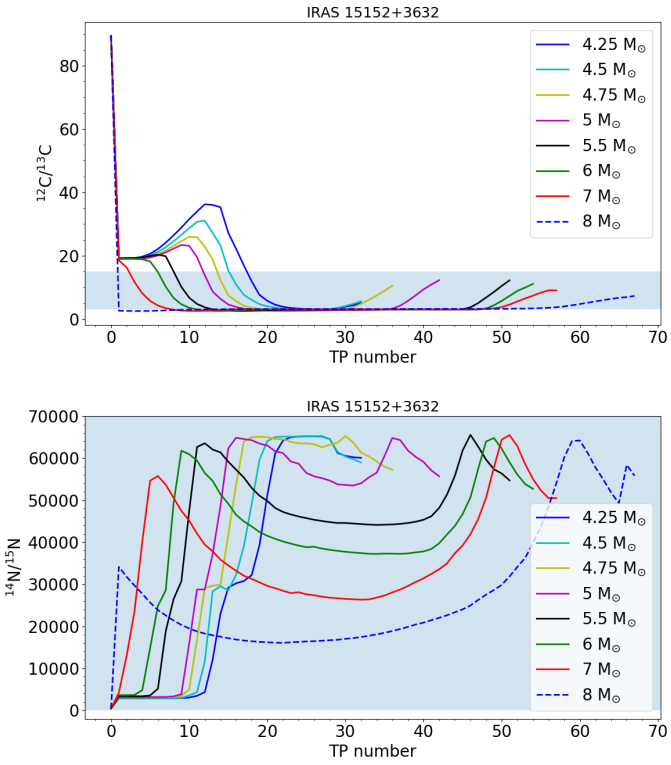

Figure C.2: Theoretical Monash predictions for the $^{12}C/^{13}C$ (*top panel*) and $^{14}N/^{15}N$ (*bottom panel*) isotopic ratios against TP number for the progenitor masses that experience HBB at solar metallicity. The shaded regions indicate the range of C and N isotopic ratios of IRAS 15152+3632 taking into account the uncertainties.

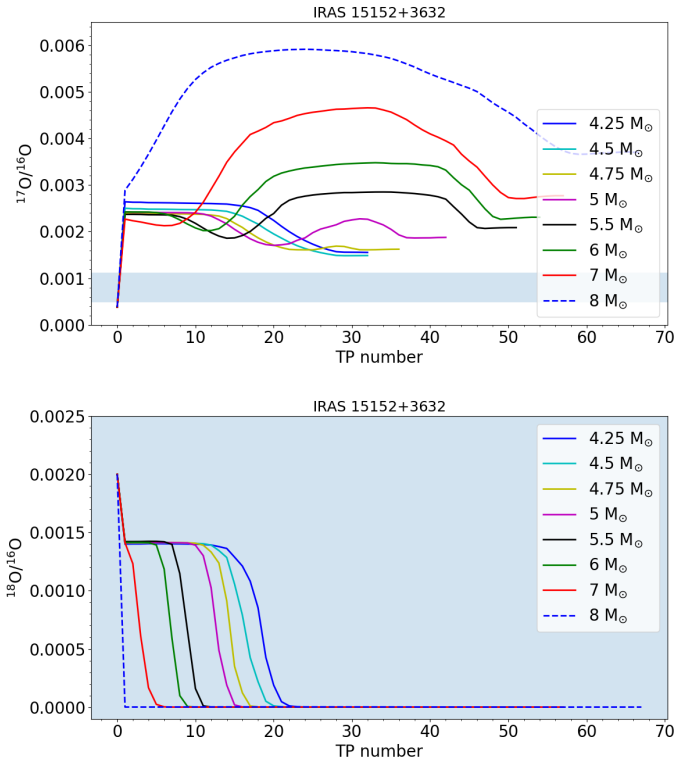

Figure C.3: Theoretical Monash predictions for the $^{17}O/^{16}O$ (*top panel*) and $^{18}O/^{16}O$ (*bottom panel*) isotopic ratios against TP number for the progenitor masses that experience HBB at solar metallicity. The shaded regions indicate the range of O isotopic ratios of IRAS 15152+3632 taking into account the uncertainties.

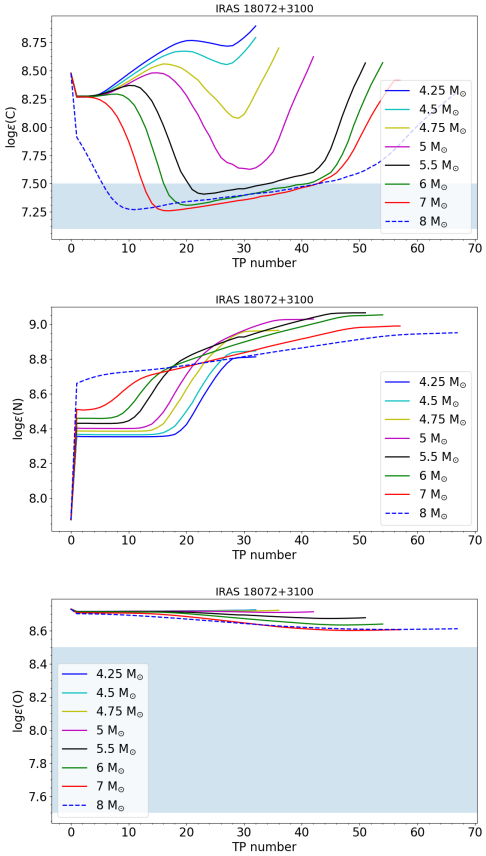

Figure C.4: Theoretical Monash predictions for the C (*top panel*), N (*middle panel*) and O (*bottom panel*) elemental abundances against TP number for the progenitor masses that experience HBB at solar metallicity. The shaded regions indicate the range of CNO abundances of IRAS 18072+3100 taking into account the uncertainties.

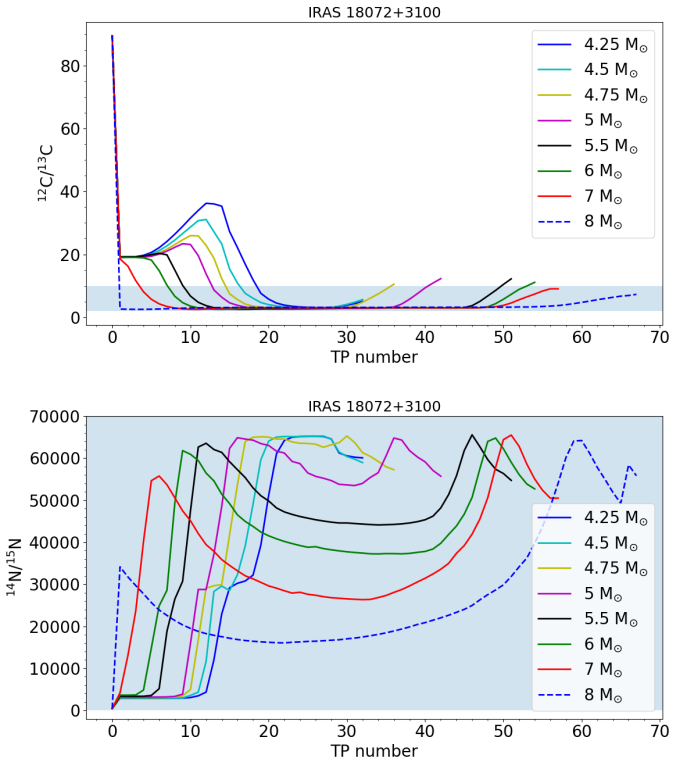

Figure C.5: Theoretical Monash predictions for the $^{12}C/^{13}C$ (*top panel*) and $^{14}N/^{15}N$ (*bottom panel*) isotopic ratios against TP number for the progenitor masses that experience HBB at solar metallicity. The shaded regions indicate the range of C and N isotopic ratios of IRAS 18072+3100 taking into account the uncertainties.

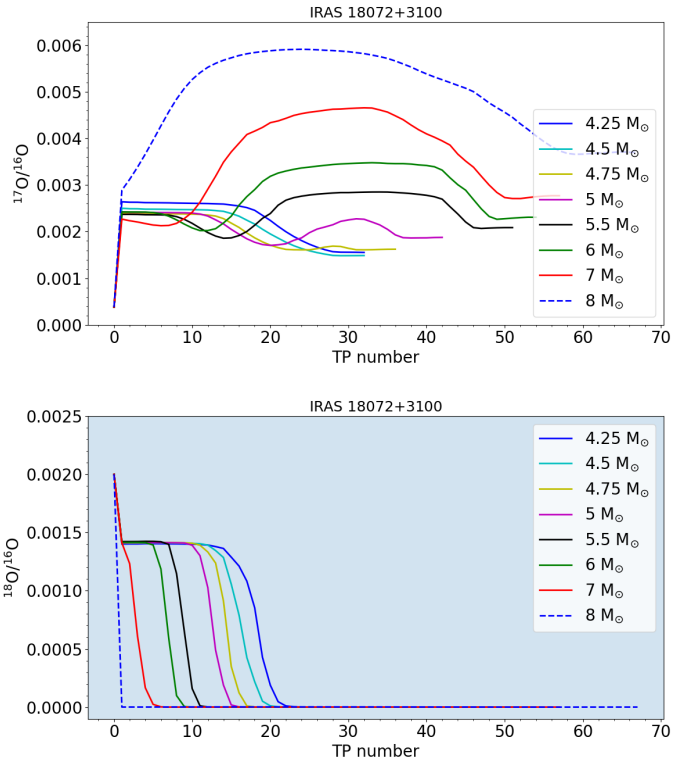

Figure C.6: Theoretical Monash predictions for the $^{17}O/^{16}O$ (*top panel*) and $^{18}O/^{16}O$ (*bottom panel*) isotopic ratios against TP number for the progenitor masses that experience HBB at solar metallicity. The shaded regions indicate the range of O isotopic ratios of IRAS 18072+3100 taking into account the uncertainties.

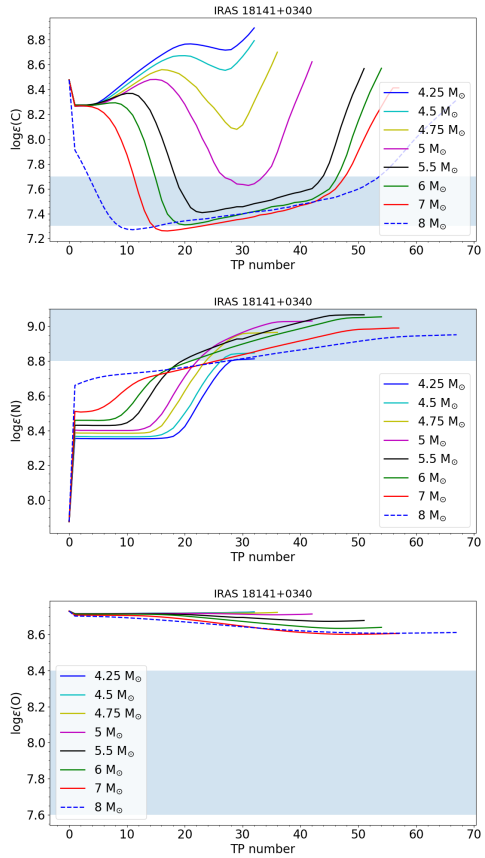

Figure C.7: Theoretical Monash predictions for the C (*top panel*), N (*middle panel*) and O (*bottom panel*) elemental abundances against TP number for the progenitor masses that experience HBB at solar metallicity. The shaded regions indicate the range of CNO abundances of IRAS 18141+0340 taking into account the uncertainties.

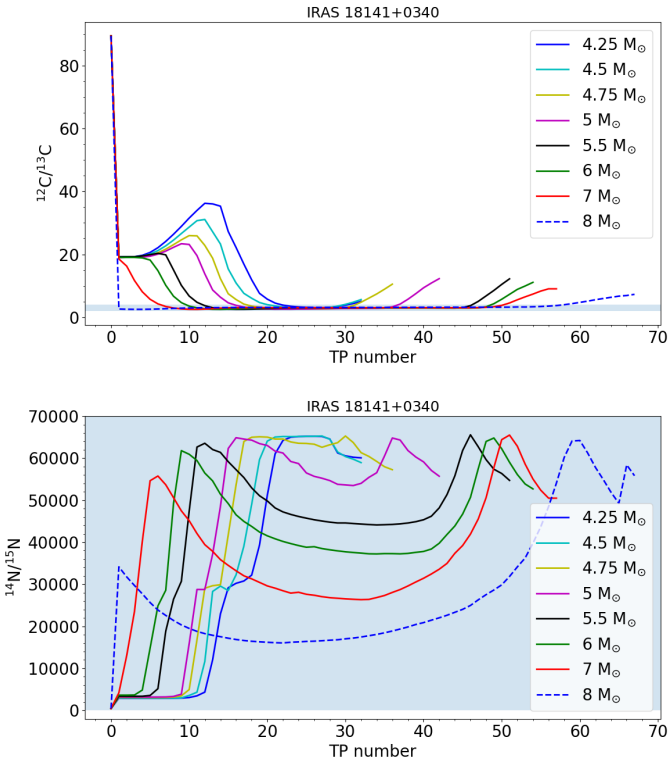

Figure C.8: Theoretical Monash predictions for the $^{12}C/^{13}C$ (*top panel*) and $^{14}N/^{15}N$ (*bottom panel*) isotopic ratios against TP number for the progenitor masses that experience HBB at solar metallicity. The shaded regions indicate the range of C and N isotopic ratios of IRAS 18141+0340 taking into account the uncertainties.

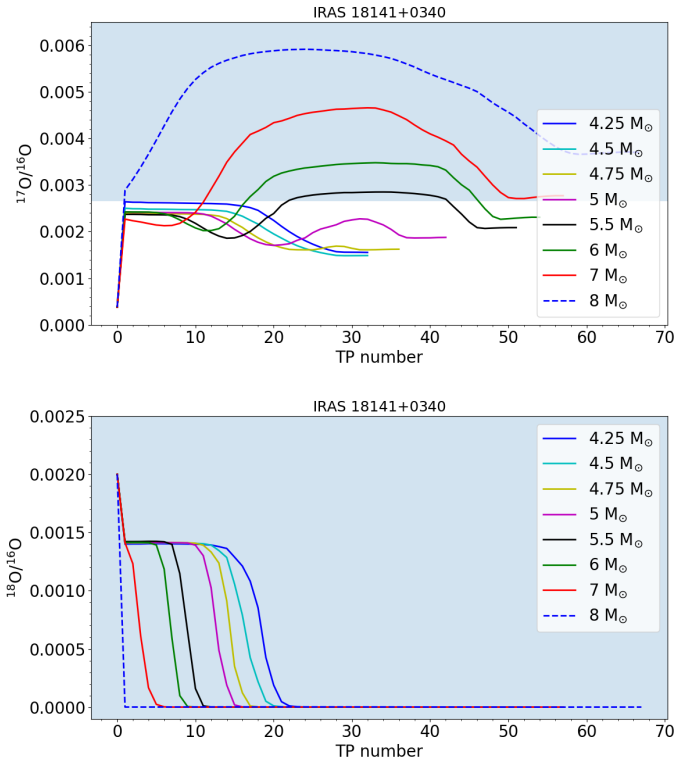

Figure C.9: Theoretical Monash predictions for the $^{17}O/^{16}O$ (*top panel*) and $^{18}O/^{16}O$ (*bottom panel*) isotopic ratios against TP number for the progenitor masses that experience HBB at solar metallicity. The shaded regions indicate the range of O isotopic ratios of IRAS 18141+0340 taking into account the uncertainties.

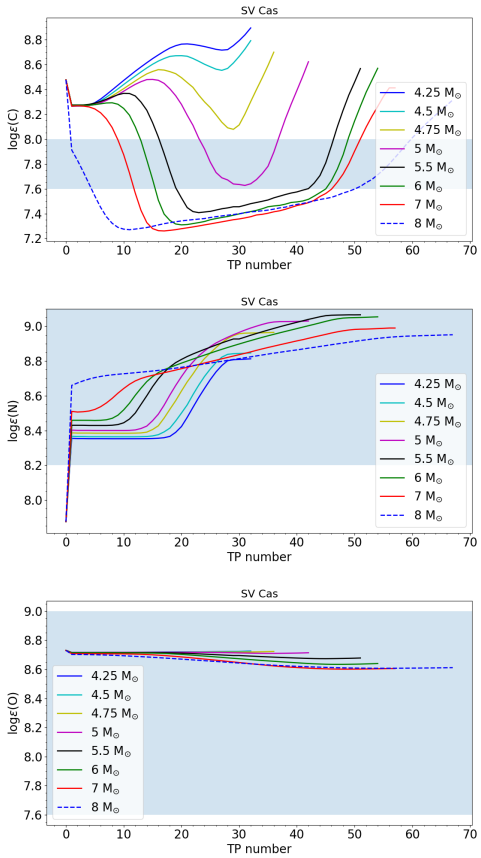

Figure C.10: Theoretical Monash predictions for the C (*top panel*), N (*middle panel*) and O (*bottom panel*) elemental abundances against TP number for the progenitor masses that experience HBB at solar metallicity. The shaded regions indicate the range of CNO abundances of SV Cas taking into account the uncertainties.

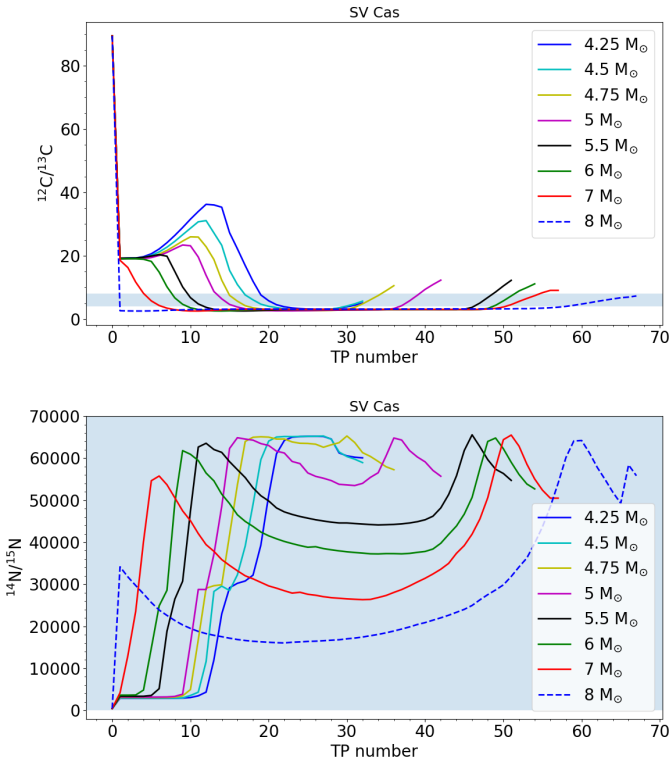

Figure C.11: Theoretical Monash predictions for the $^{12}C/^{13}C$ (*top panel*) and $^{14}N/^{15}N$ (*bottom panel*) isotopic ratios against TP number for the progenitor masses that experience HBB at solar metallicity. The shaded regions indicate the range of C and N isotopic ratios of SV Cas taking into account the uncertainties.

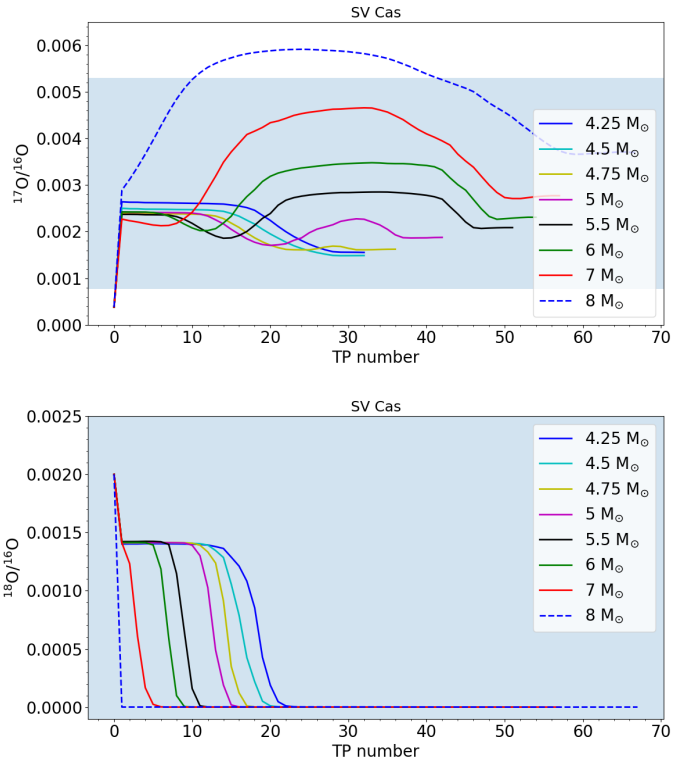

Figure C.12: Theoretical Monash predictions for the $^{17}O/^{16}O$ (*top panel*) and $^{18}O/^{16}O$ (*bottom panel*) isotopic ratios against TP number for the progenitor masses that experience HBB at solar metallicity. The shaded regions indicate the range of O isotopic ratios of SV Cas taking into account the uncertainties.

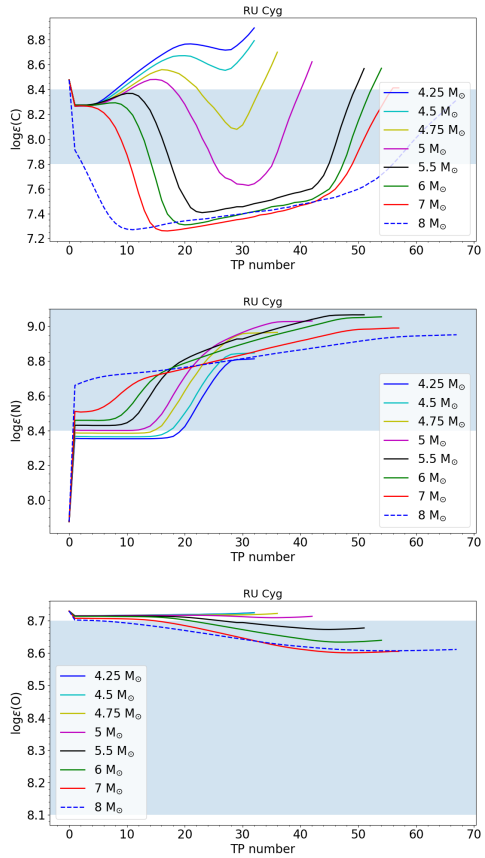

Figure C.13: Theoretical Monash predictions for the C (*top panel*), N (*middle panel*) and O (*bottom panel*) elemental abundances against TP number for the progenitor masses that experience HBB at solar metallicity. The shaded regions indicate the range of CNO abundances of RU Cyg taking into account the uncertainties.

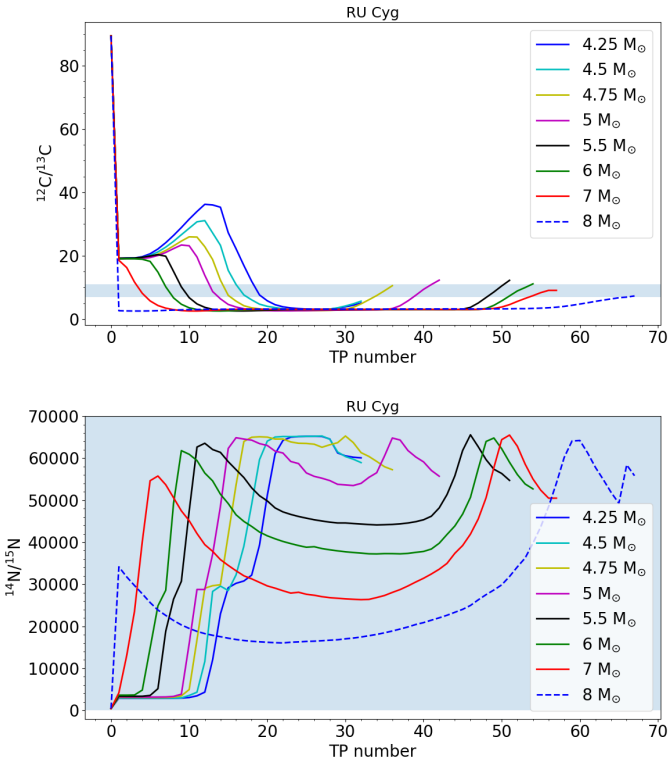

Figure C.14: Theoretical Monash predictions for the $^{12}C/^{13}C$ (*top panel*) and $^{14}N/^{15}N$ (*bottom panel*) isotopic ratios against TP number for the progenitor masses that experience HBB at solar metallicity. The shaded regions indicate the range of C and N isotopic ratios of RU Cyg taking into account the uncertainties.

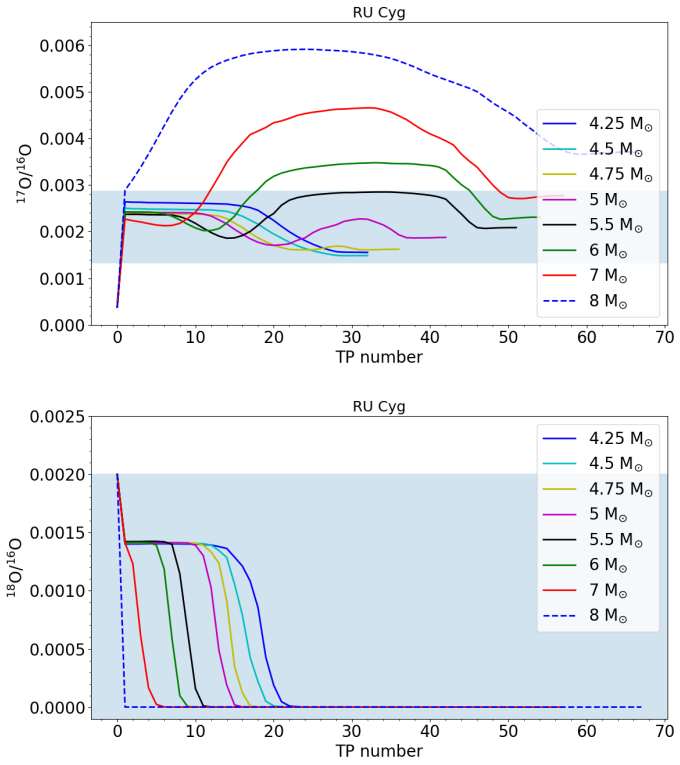

Figure C.15: Theoretical Monash predictions for the $^{17}O/^{16}O$ (*top panel*) and $^{18}O/^{16}O$ (*bottom panel*) isotopic ratios against TP number for the progenitor masses that experience HBB at solar metallicity. The shaded regions indicate the range of O isotopic ratios of RU Cyg taking into account the uncertainties.